NUMERICAL MODELING OF HOLLOW OPTICAL FIBER DRAWING PROCESS

BY JING YANG

A dissertation submitted to the

Graduate School—New Brunswick

Rutgers, The State University of New Jersey

in partial fulfillment of the requirements

for the degree of

Doctor of Philosophy

Graduate Program in Mechanical and Aerospace Engineering

Written under the direction of

Professor Yogesh Jaluria

and approved by

_____

_____

_____

_____

New Brunswick, New Jersey

January, 2008

ABSTRACT OF THE DISSERTATION

Numerical Modeling of Hollow Optical Fiber Drawing Process

by Jing Yang

Dissertation Director: Professor Yogesh Jaluria

The hollow optical fiber drawing process has been numerically investigated. Axisymmetric, laminar and conjugated flows of gas in the central cavity, glass and aiding purge gas, were simulated in the model. A numerical scheme was proposed to correct the inner and outer surfaces of the hollow fiber. The optically thick approximation, as well as the zonal model, was applied to calculate the radiative transport within glass. The validation of the model was carried out. It is shown that the results from the model are consistent with the physical trends and agree well with the results in the literature. The effects of variable properties of air and buoyancy were investigated and results indicated that these effects are neglectable for simulating the draw process. The effects of physical parameters, such as the temperature distribution on the furnace wall, the drawing speed, the preform feeding speed, geometry of the preform and material properties, on the thermal transport, the neck-down profiles, the final collapse ratio and draw tension have been studied. Then, an appropriate objective function, comprised of the maximum velocity lag, E' and NBOHCs defect concentrations and draw tension, has been proposed to describe the quality of the hollow fiber. The feasible domain for hollow optical fiber drawing process was identified for optimal design. A multi-variable and non-constrained optimal design problem in hollow optical fiber drawing process

has been solved by the univariate search and curve fitting method. Finally, collapse of Microstructured Polymer Optical Fibers (MPOFs) during the drawing process was investigated by a porous media model. Results provided the effects of parameters on the final porosity of MPOFs. This model has been validated by comparing with the results for solid-core and hollow fibers drawing processes.

Acknowledgements

I would like to express my deepest gratitude and appreciation to my academic advisor, Professor Yogesh Jaluria, for his invaluable guidance, encouragement, support and understanding throughout the whole course of my Ph.D. program. I wish to thank the members of the committee for my dissertation for their comments and suggestions based on their careful evaluation of my work.

I would like to thank Dr. S. H. -K. Lee, Dr. S. Roy Choudhury, Dr. Z. Yin, Dr. X. Cheng and Dr. C. Chen for their pioneering work on optical fiber drawing simulation. It would have been impossible for me to pursue my research without their previous work.

I am very thankful to my friends, Dr. Hong Zhao, Dr. Fusheng Xu, Dr.Haiyong Quan and Dr. Gaozhu Peng for their suggestions and help during the course of my research and daily life. I also wish to thank the departmental secretaries, Ms. Virginia Dare, Ms. Aiesha Jenkins and Ms. Helene Press for all of their help during my graduate studies.

The Financial support from the National Science Foundation and from the Department of Mechanical and Aerospace Engineering, Rutgers, The State University of New Jersey, are gratefully acknowledged.

Dedication

This dissertation is dedicated to my husband, Chen Lin, and my parents for their understanding, support and love.

Table of Contents

List of Tables

List of Figures

List of Abbreviations

A	Area
a	Absorption coefficient
C	Collapse ratio; Specific heat at constant pressure
E_c	Activatiion energy for NBOHCs defect
E_d	Activatiion energy for E' defect
E_p	Activatiion energy for precursor
F	View factor
F_g	Force due to gravity
F_I	Force due to inertia
F_T	Draw tension
F_μ	Force due to glass viscous stress
F_ξ	Force due to surface tension
f	Black body radiation fraction
G	Irradiation
$\overline{GG}$	Volume-volume direct exchange area
$\overline{GS}$	Volume-surface direct exchange area
Gr	Grashof number
g	Magnitude of gravitational acceleration
H	Mean curvature of the surface
J	Radiosity

K	Overall thermal conductivity
K_c	Thermal conductivity
K_r	Radiative conductivity
k	Boltzmann constant
L	Furnace length
N	Number of zones; Number of air holes
n	Normal direction; Refractive index of silica glass
$n_{E'}$	Concentration of E' defect
n_{NBOHCs}	Normalized concentration of NBOHCs
n_p	Concentration of precursor
p	Local pressure
q_{flux}	Radiative heat flux
R	Neck-down profile of MPOF
R_F	Furnace radius
R_1	Inner neck-down profile
R_{10}	Inner radius of the preform
R_2	Outer neck-down profile
R_{20}	Outer radius of the preform
R'	Radius of circular air holes in MPOF
r	Radial coordinate
S	Distance
S_r	Radiation source term
S_μ	Source term due to the variable viscosity
$\overline{SS}$	Surface-surface direct exchange area

T	Temperature
T_{melt}	Softening temperature
T_w	Temperature at the wall of furnace
T_0	Temperature of the preform and ambient gas
t	Time
U	Non-dimensional radial velocity; Objective function
u	Radial velocity
V	Non-dimensional axial velocity
V_a	Inlet velocity of purge gas
V_f	Drawing velocity
V_z	One dimensional lumped axial velocity
V_0	Feeding velocity
v	Axial velocity
z	Axial coordinate

Greek Symbols

β	Thermal expansion coefficient; Non-dimensional axial coordinate
ϵ	Relative error; Hemispherical emissivity
ξ	Surface tension coefficient
η	Non-dimensional radial coordinate
θ	Polar angle; Non-dimensional temperature
λ	Wavelength
μ	Dynamic viscosity
ρ	Density; Reflectivity

σ	Shear stress; Stephan-Boltzman constant
τ	Transmissivity
Φ	Viscous dissipation term
ϕ	Azimuthal angle; Porosity
Ψ	Non-dimensional streamfunction
ψ	Streamfunction
Ω	Non-dimensional vorticity
ω	Vorticity

Superscripts

1	Interface between glass layer and central cavity
2	Interface between glass layer and outer purge gas
c	Central cavity enclosure
g	Glass layer enclosure
o	Outer purge gas enclosure
$'$	First derivative with respect to z
$''$	Second derivative with respect to z
$-$	Reference point

Subscripts

1	Inner surface of hollow optical fiber
2	Outer surface of hollow optical fiber
a	External gas region
c	Central cavity region
g	Volume zones

i	Surface or volume element
j	Surface or volume element
k	Volume element
l	l^{th} absorbing band
ref	Reference value
s	Surface zones

Chapter 1

Introduction

1.1 History and background

An optical fiber is a glass or plastic fiber which is designed to propagate light along its length by confining as much light as possible within the wave guide. In the 1840s, the light-guiding principle was proposed. In the 1950s, optical fibers were largely developed for medical applications. In 1966, Kao and Hockham [33] of the British company Standard Telephones and Cables first speculated that the optical fiber could be a practical medium for tele-communication if the attenuation could be reduced to below 20 dB/km. In 1970, a fiber with a low-loss (below 20 dB/km) attenuation was first manufactured from a preform produced by Outside Vapor Phase Oxidation (OVPO) by researchers Kapron et al in Corning Glass Works, now Corning Inc [47]. Then the advent of modern age of optical fibers began. Currently, fibers with loss less than 0.5 dB/km for certain wavelengths have been widely manufactured. Today, optical fibers have a widely range of applications in medicine, military and industry. The applications of optical fibers are telecommunications, sensors, high power delivery, thermal imaging and so on.

A variety of materials are used to develop optical fibers. Based on the material, optical fibers can be divided into three categories: glass, crystalline, and plastic. Optical fibers were first made from silica glass. Then around 1975, some other glasses, such as fluorozirconate, fluoroaluminate, and chalcogenide glasses, were used to fabricate optical fibers. The optical fibers made from these glasses were designed to transmit radiation with wavelengths greater than 2 μm [24]. So they are called glass infrared optical fibers. The melting or softening temperature of these glasses is much lower than that of silica (about 1900 K). For example, the melting temperature of heavy metal fluoride glass is only 538 K [49]. And most of glass infrared optical fibers have higher

loss compared to silica glass optical fibers except fluoride glass fibers. Fluoride glass fibers have losses as low as a few dB/km. Crystalline material is also used to fabricate infrared optical fibers. There are two types of crystalline fibers: single-crystal (SC) and polycrystalline (PC) fiber [2, 46, 58]. Most non-oxide crystalline materials can transmit longer wavelength radiation than IR glasses. Therefore, these fibers are mainly used in military surveillance satellite application. Plastics can also be used to fabricate optical fibers. This kind of optical fiber is called Plastic Optical Fiber (POF). Conventional POFs are made from polymethyl methacrylate (PMMA) [27]. POFs typically have much higher attenuation than glass fibers, but they are relatively inexpensive. So they can be used for short-distance data transmission.

The most common structure of optical fibers is the clad-core structure. In this structure, the light-guiding central portion (called "core") is surrounded by a dielectric layer (called "cladding") which has a slightly lower refractive index than that of the core. Figure 1.1(a) schematically shows the clad-core structure. Clad-core optical fibers can be classified into two general categories, i.e. single-mode and multimode. The difference between single-mode and multi-mode fibers is that the single-mode fiber allows only one mode of light to propagate while the multi-mode fiber allows hundreds of modes of light to propagate simultaneously. Multi-mode fibers have larger core diameters (usually greater than 10 μm). In multimode fiber, components of light transmitted by different modes exhibit different group velocities. This results in multimode dispersion. Clad-core optical fibers are also classified into step-index fibers and graded-index fibers based on the refractive index in the core. The profile of the refractive index in the core is uniform in step-index fibers and gradual in graded-index fibers. Besides the clad-core structure, there is another structure called hollow waveguide. Hollow waveguides have many advantages over conventional solid-core fibers. These include high laser power thresholds, low insertion loss, no end reflection, ruggedness, and small beam divergence. Due to the presence of air core, hollow waveguides can be used to provide infrared laser beam and high-power delivery. Applications of hollow waveguides are medical applications, sensor technology, diagnostics and CO_2 and Er: YAG laser delivery, besides traditional telecommunications.

A new class of optical fibers, called photonic crystal fibers (PCF) or microstructured optical fibers (MOF), has been of considerable interest in recent years [14, 43]. MOFs can be divided into solid-core MOFs and hollow-core MOFs. Figure 1.1(b) schematically shows the structure of the solid-core MOFs. The effect of the periodic structure around the core in solid-core MOFs is the same as that of the cladding in the clad-core optical fibers. In solid-core MOFS, light is confined within the core by diffraction from a periodic structure. Compared to conventional optical fibers, MOFs have many advantages. For example, solid-core MOFs can be designed to get a much higher refractive index difference between core and cladding. Hollow-core MOFs can be used to carry gas due to the hollow core. And MOFs can carry higher power or light in different wavelength range for which material may not be available. Now MOFs are applied in fiber-optic communications, fiber lasers, nonlinear devices, high-power transmission, highly sensitive gas sensors, and other areas.

Polymers, especially PMMA, are also introduced to fabricate MOFs. This kind of MOFs is called microstructured polymer optical fibers (MPOFs). Figure 1.2 shows structures of different kinds of MPOFs which are single-mode, graded-index, twin-core and hollow-core MPOFs [17]. MPOFs have many advantages over MOFs and POFs. First, the collapse of holes occurring during the drawing process strongly depends on the surface tension. So the collapse of holes in MPOFs can be greatly reduced due to the small surface tension [64]. Second, much lower glass transition temperature and the tailorability of polymers offer more flexibilities in the fabrication methods [17]. And low cost to fabricate MPOFs is another advantage. MPOFs have a wide range of applications, such as high-bandwidth transmission (local-area-networks and fibre-to-the-premises), imaging, sensing and high birefringence. MPOFs made from polymers with high glass transition temperatures can be used for high temperature applications (for example in the automotive industry) [17].

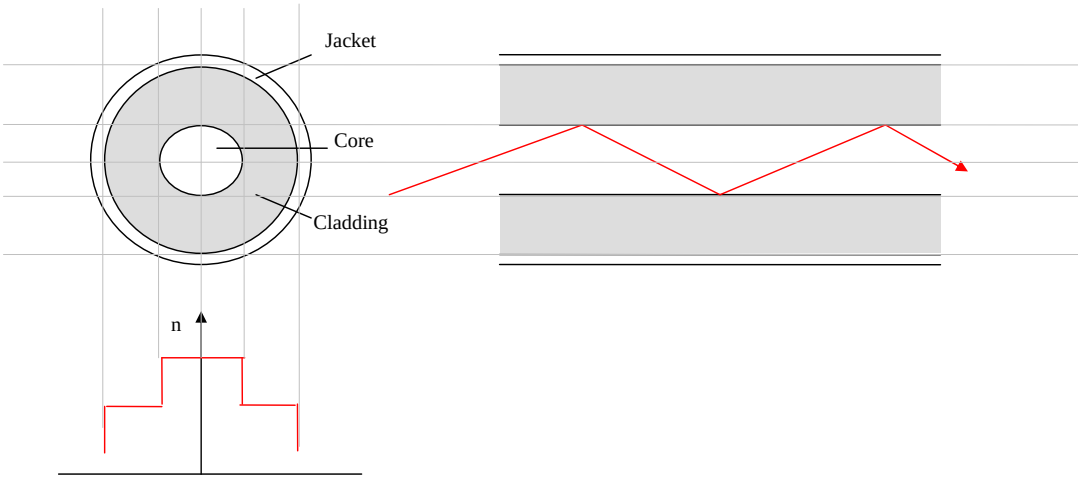

(a)

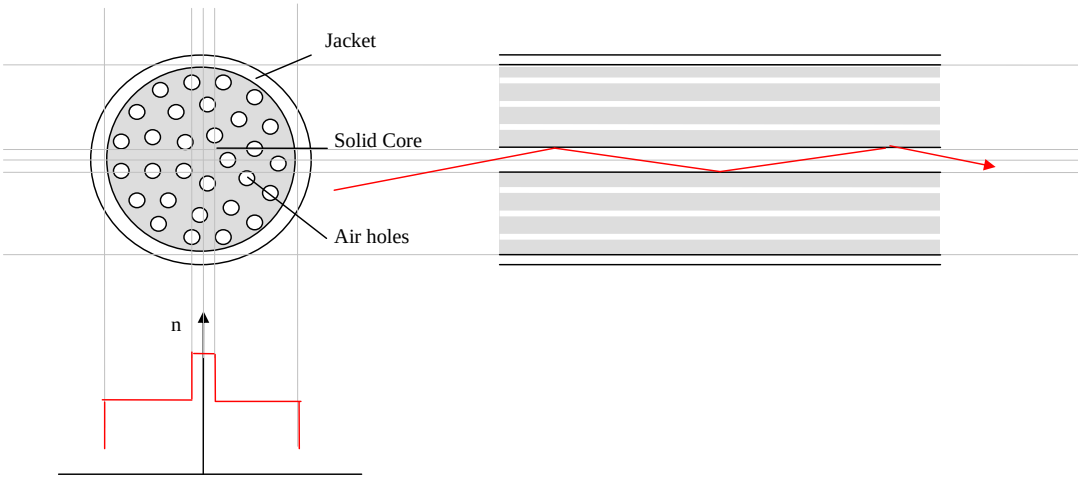

(b)

Figure 1.1: Schematic diagram of (a) Clad-core (b)solid-core PCFs

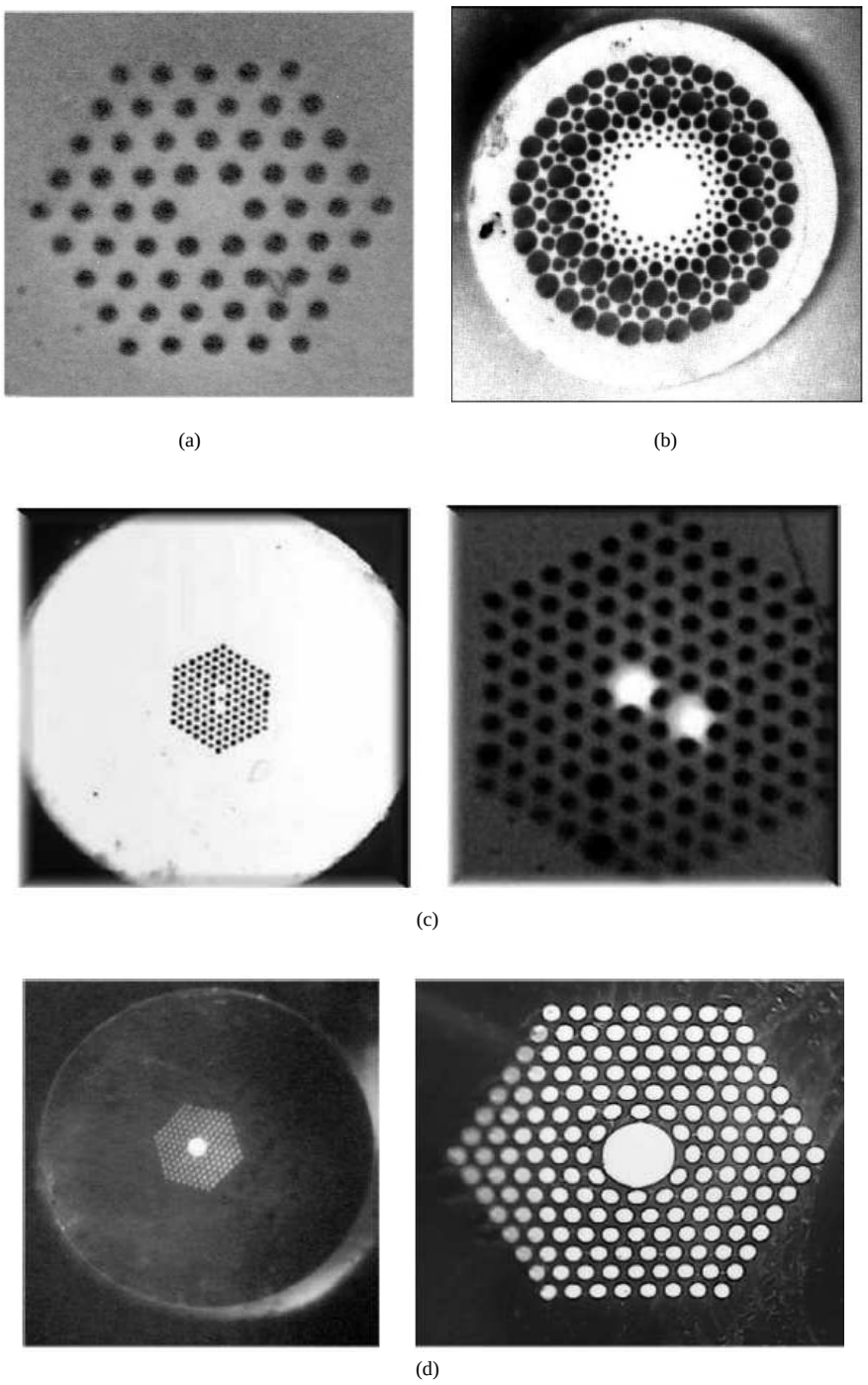

Figure 1.2: Hole pattern in (a) a single-mode MPOF (b) a graded-index MPOF (c) a twin core MPOF (d) a hollow core MPOF

1.2 Manufacturing of hollow optical fiber drawing

1.2.1 Preform

The manufacturing of an optical fiber typically starts with the fabrication of preform. Here a brief introduction to fabrication of preform is presented. There are variety of methods that can be used to fabricate the perform. For conventional solid core glass preform three common approaches are: Modified Chemical Vapor Deposition (MCVD), Outer Vapor Deposition (OVD), and Vapor-Phase Axial Deposition (VAD) [29, 44].

MCVD was first introduced at Bell Laboratory in the early 1970s. The schematic diagram of the MCVD is shown in Figure 1.3. A mixed vapor of $SiCl_4$, $GeCl_4$ and fluorinated hydrocarbons along with oxygen flows through a rotating hollow silica tube. This hollow silica tube horizontally placed is heated up by an external oxyhydrogen flame. The oxidizing reaction occurs in the tube and then produced a thin layer of glass soot deposited inside the tube. Then, the sintered glass layer are heated to the softening point and finally collapsed into a solid preform rod. The refractive index can be controlled layer by layer in the radial direction. MCVD is the most widely used preform fabrication process now.

OVD, which is more complicated than MCVD, was developed at Corning Glass Works in the early 1970s. The schematic diagram of the OVD is shown in Figure 1.4. The glass particles produced by oxidizing reaction are deposited on the surface of a rotating target rod. The core material is deposited first, followed by the cladding. Then, the target rod is removed from the center of the porous preform. Finally, the preform is consolidated into a solid preform rod in a furnace.

VAD was proposed in Japan in 1977. Figure 1.5 shows the basic principle for the VAD process. The methods of deposition and consolidation in the VAD process are the same as in the OVD process. But in the VAD process, the preform can be continuously fabricated in the axial direction because the deposition and consolidation steps are arranged in a single line. However, it is more difficult for VAD to control the refractive index of the preform in the radial direction.

The preforms of microstructured optical fibers have a lot holes. For silica fibers, the

stacking technique is the most popular and convenient way to fabricate the preform. Capillaries and rods are stacked by hand to form the desired geometry on a macroscopic scale. The hole structure is mostly restricted to hexagonal or square close-packed structures due to the stacking technique [34]. For polymers, many fabrication techniques, such as drilling, extrusion and molding, can be used. So it is easy to obtain different geometry on a macroscopic scale for polymers. This is also an advantage of polymers over glass in MOFs fabrication. After the preform fabrication, the fiber can be drawn from the preform in the drawing process.

1.2.2 Fiber drawing process

The manufacture process of typical optical fibers is schematically showed in Figure 1.6 [53]. The continuous fiber manufacture process consists of drawing, cooling, coating and curing processes. First, the preform (typically a few centimeters in diameter) is fed into the drawing furnace by a feed mechanism. Then the preform is heated up to the softening temperature, which is about 1900 K for silica, mostly through radiation heat transfer from the furnace surface. By pulling the softened material, the preform can be drawn down at a chosen draw speed to obtain a fiber (typically 125 μm in diameter). Two common drawing furnaces, namely graphite furnace and zirconia furnace [44], are employed for silica preform drawing. In the drawing furnace, the region where the perform narrows down sharply is called the neck-down region. The shape of the neck-down region is a combined effect of drawing conditions such as the preform feeding speed (the speed of preform), the drawing speed (the exit speed of fiber), the temperature distribution on the furnace wall, etc. The geometry of the final fiber (inner and outer diameters) depends on the shape of the neck-down region.

Leaving the drawing furnace, the fiber is monitored to adjust its diameter and then cooled in the cooling section. Usually forced cooling in an inert gas is applied to cool the fiber. The fiber must be cooled to a certain allowable temperature level for a successful coating process. Then the fiber is coated in the coating cup, which is located below the drawing furnace and the cooling section. The purpose of coating is to protect the fiber surface from external damage and to preserve the original fiber strength. The coating

applicators are classified as open-cup and pressurized. Then the coating is generally cured in a curing oven. After the coating and curing processes, fiber is wrapped up in a winding drum.

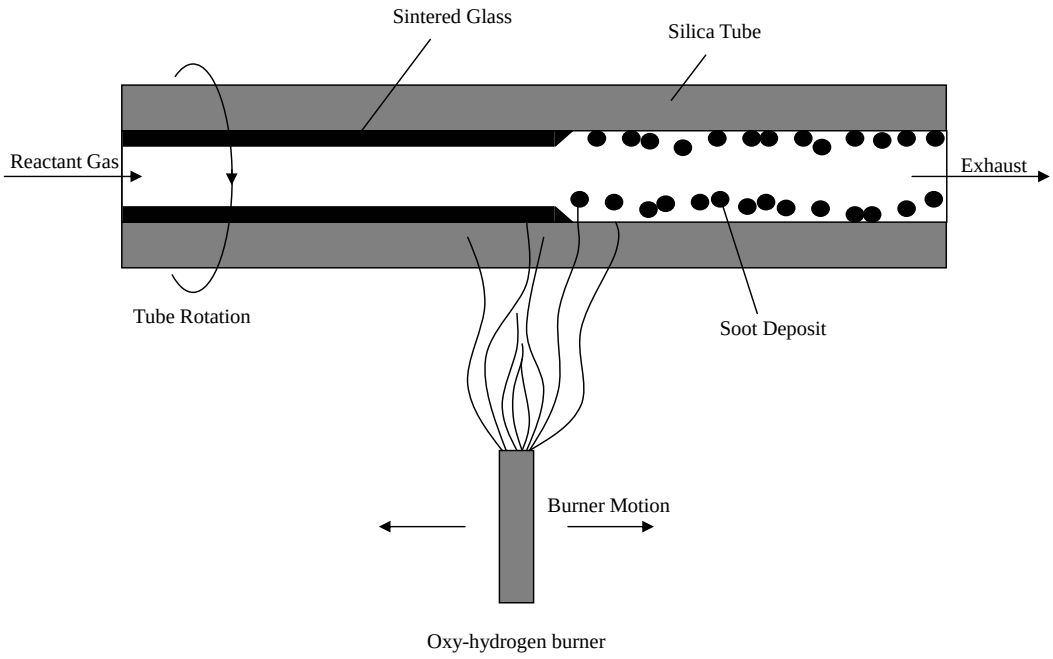

Figure 1.3: Schematic diagram of the MCVD process

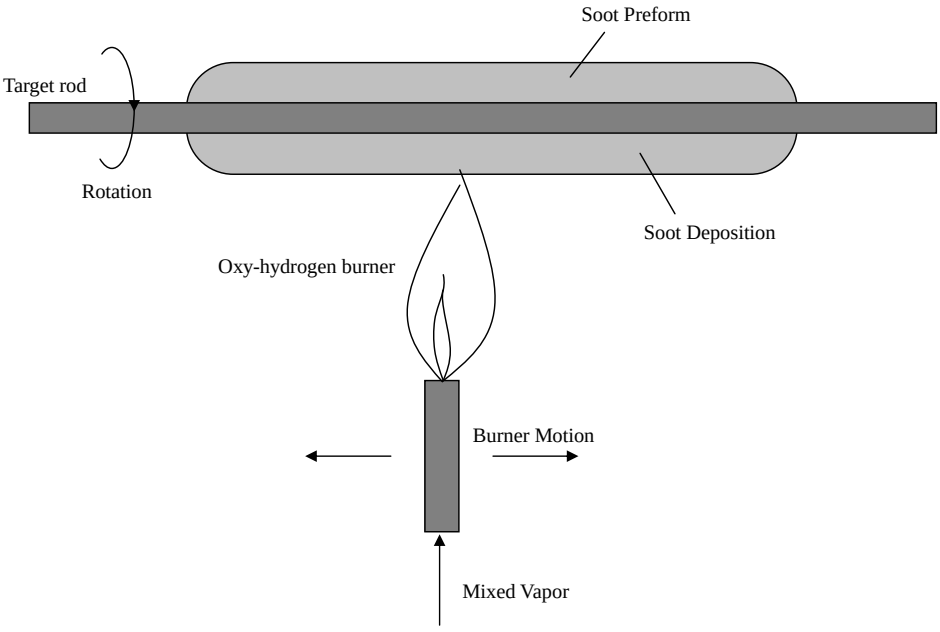

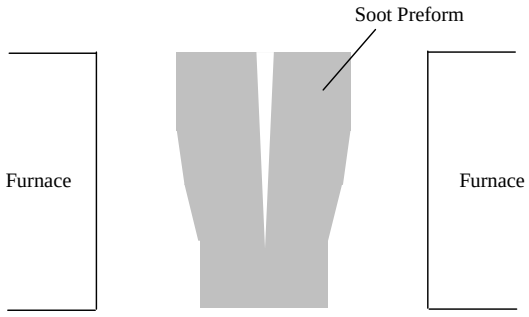

Figure 1.4: Schematic diagram of the OVD process

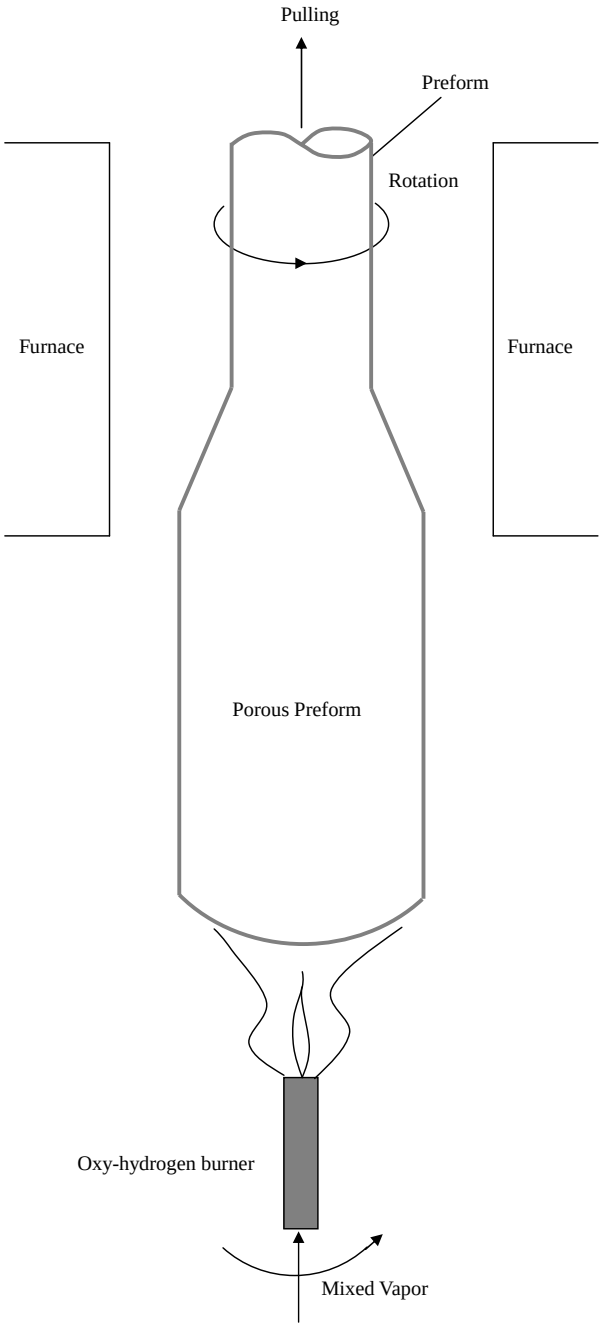

Figure 1.5: Schematic diagram of the VAD process

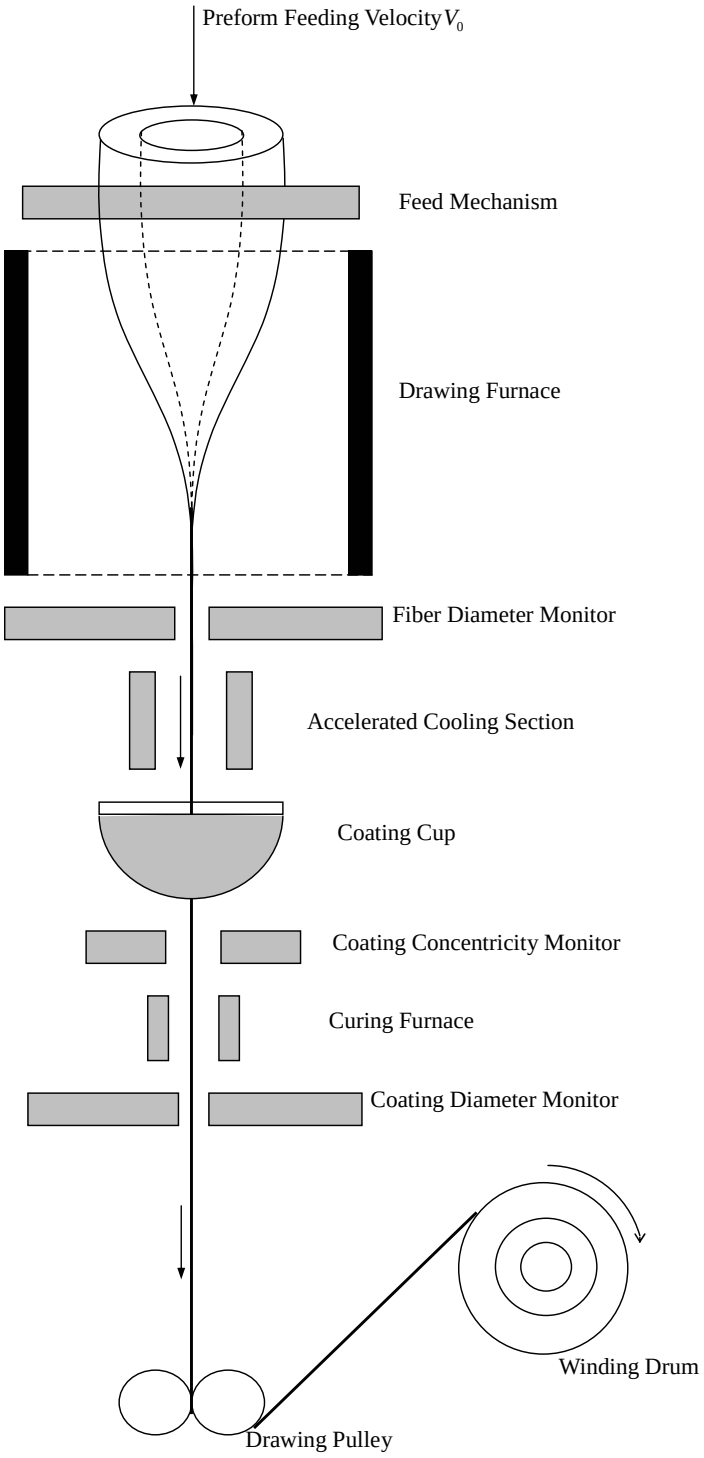

Figure 1.6: Schematic diagram of a fiber drawing tower

1.3 Previous work

A brief overview is presented here. A study on the optical fiber drawing process has been of considerable interest since the late 1960's. After the mid 1970s, a number of researchers investigated the thermal transport in the neck-down region of the solid-core silica glass optical fiber drawing process. Many numerical and theoretical models and experiments were carried out to investigate the radiative and convective heat transport in the furnace, neck-down profile generation, high draw-down ratio, optimization, instability and so on. The radiation was computed using the optically thick approximation in most of the models. Compared to the work done on solid-core fiber drawing, very few investigations have been carried out on hollow optical fiber drawing. Recently, with the development of MPOFs the study in the MPOFs drawing process is important and required. More detailed reviews of related investigations will be provided later in appropriate chapter.

1.4 Present work

1.4.1 Motivation

Drawing hollow optical fibers in the furnace is a very complicated process, which involves a combination of conduction, natural and forced convection, and radiation transport. The geometry of the final fiber plays an important role in the optical characteristics and performance of the fiber. For instance, the wall thickness of the fiber is designed to get low signal loss over a target wavelength region. The geometry of the final fiber is determined by the two neck-down profiles, which strongly depend on the fiber drawing conditions such as the speed of feeding preform, the drawing speed, the temperature distribution of furnace and the draw tension. The presence of a large air core is necessary in hollow fibers for high-power laser delivery. So it is desirable to avoid the air core from closing completely during the process, which may occur under certain drawing conditions. Recently, with the development of MPOFs, the study on the drawing process has attracted more attention.

1.4.2 Objective

The objective of the present study is to carry out an analytical and numerical study to model the drawing process for hollow optical fibers. Then the model can used to predict the geometry and quality of the final fiber and investigate the effects of drawing conditions on the draw tension and the collapse of the central cavity. Then feasible domain for hollow optical fiber drawing process is identified. In the feasible domain, the drawing process can be optimized to get high quality hollow optical fibers at high production rates.

1.4.3 Overview of the dissertation

The present work on the hollow optical fiber drawing process is divided into five distinct chapters. In chapter 2, the general mathematical model is proposed to simulate the drawing process. Axisymmetric flow of gas in the central cavity, as well as the flows of glass and aiding purge gas, is considered. Two neck-down profiles, which represent the inner and outer surfaces of the hollow fiber, are generated by using an iterative numerical scheme. The optically thick assumption is used to model the radiative heat transfer in the model. The effects of variation in different parameters are investigated. The geometry of the final hollow fiber is predicted and feasible combinations of parameters for successful hollow fiber drawing are obtained. The validation of the model is carried out by comparing the predictions with the results for solid-core fiber drawing and with available experimental and numerical results for hollow fibers. It is shown that the results from the model are consistent with the physical trends and agree well with the results in the literature.

In Chapter 3, the zonal method, which is more accurate than optically thick method, is applied to calculate the radiative transport within the glass. The effects of variable properties for air and buoyancy are investigated and results indicate that these can be neglected in most cases for simulating the draw process. The validation of the model is carried out by comparing the results with those obtained by using optically thick method as well as those for a solid-core fiber. The effects of the drawing parameters,

such as the temperature of the furnace, the preform feeding speed and the drawing speed, on the thermal transport in the furnace, the neck-down profiles, the collapse ratio and the draw tension are studied. It is found that the geometry and qualities of the final hollow optical fiber are highly dependent on the drawing parameters, especially the drawing temperature and the preform feeding speed.

The optimal design of the hollow optical fiber drawing process is the topic of chapter 4. A multi-variable and non-constrained optimal design problem in hollow optical silica fiber drawing process is presented. The feasible domain of hollow optical fiber drawing is identified to give the range of the drawing parameters for optimal design. An appropriate objective function, comprised of the maximum velocity lag, defect concentration and draw tension, is proposed to describe the quality of the hollow fiber. The results are curve fitted and the univariate search is applied to obtain the optimal drawing temperature and the preform feeding speed.

Then the previous model is modified to simulate MPOF drawing process in chapter 5. MPOF is considered as a porous media. Effects of the microstructure in MPOF drawing process are described by the effective properties of porous media. The model is also applied to simulate the solid-core fiber and annular hollow fiber drawing processes for validation. The effects of parameters on porosity, which indicates the collapse of MPOF during the drawing process, are studied in detail. It is found that the final porosity of MPOF strongly depends on the geometry of the preform (such as the number of holes and the initial porosity), material properties (such as surface tension) and drawing parameters (such as the drawing speed, the preform feeding speeds and the temperature distribution on the furnace wall).

Major results and conclusions are summarized in the last chapter. Future work is also presented.

Chapter 2

Mathematical Modeling

2.1 Introduction

The drawing process of optical fibers has been introduced in the previous Chapter. The study of the optical fiber drawing process has been of considerable interest. Paek and Runk [48] first presented a physical model for the neck-down profile and temperature distribution based on the one-dimensional assumption and the balance of surface forces. Myers [45] developed a one-dimensional model for unsteady glass flow. Lee and Jaluria [35, 36, 37, 38], Roy Choudhury and Jaluria [53, 54, 55, 56, 57], Yin and Jaluria [68, 69, 70, 71], Cheng and Jaluria [9, 10, 11, 12] developed more comprehensive models to investigate the complete thermal transport and the neck-down profile of optical fiber drawing process with high draw-down ratio. Recently Chen and Jaluria [5, 6] developed a model to study the effect of core-cladding structure in the drawing process.

However few investigations on hollow fiber drawing have been made compared with the work on the solid-sore fiber drawing process. Sarboh, Milinkovic et al [59] developed a one-dimensional mathematical model for the drawing process of glass capillary tubes by studying three basic zones - the heating zone, the drawing zone and the cooling zone - separately. Fitt, Furusawa et al [18, 19] proposed a theoretical framework to simulate the fabrication of small-scale hollow glass capillaries and validated their model with experiments. Their model was only applied to predict the neck-down profiles under isothermal conditions and low preform to fiber draw-down ratio. A numerical study on collapse prediction during hollow optical fiber drawing was made by Chakravarthy and Chiu [4].

In this chapter, a numerical model is developed to investigate the drawing process of hollow optical fibers. The model can simulate the complex thermal transport processes

for high-speed drawing and show the effects of variation of different parameters. The validation of the model is carried out by comparing the predictions with the results for solid-core fiber drawing and with available experimental and numerical results on hollow fibers. It is found that the results from this model are consistent with the physical trends and agree well with the results in the literature.

2.2 Mathematical model

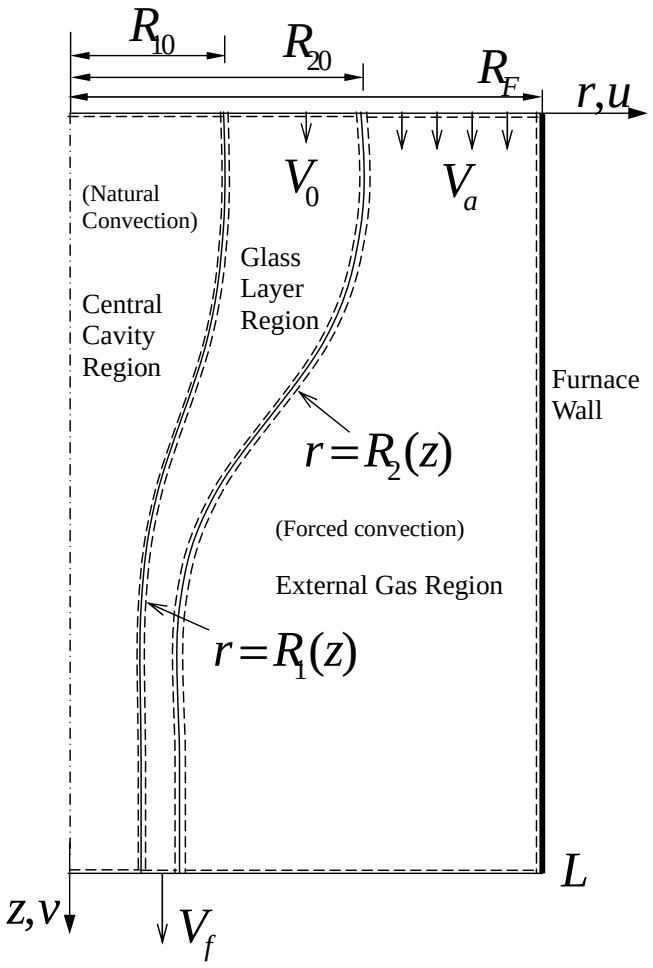

Figure 2.1: Schematic diagram of the hollow optical fiber drawing process

The geometry and coordinate system for the neck-down region in the furnace are shown in Figure 2.1. The flow in the furnace is separated into the three regions of the central cavity, the glass layer and the external gas region by two neck-down profiles $r = R_1$ and $r = R_2$. The typical outer diameter of the preform $2R_{20}$ is about 5.0 cm and the typical outer diameter of the final fiber is about 125 μm. Thus, the preform diameter is reduced by about 2 orders of magnitude during the drawing process. A conjugate problem, involving the gas flow in the central cavity, the flow of glass, and the forced convection flow of aiding purge external gas, is considered. The transport in these three regions is coupled through the boundary conditions at two free surfaces. Conduction, convection, and radiation heat transfer mechanisms are involved in the model.

2.2.1 Governing equations

Laminar flow is assumed due to the high viscosity of glass and the low velocities of the gas flow. The flows of glass, internal and external gases in cylindrical furnace are all taken as incompressible and axisymmetric. Then, the full governing equations for gas and glass are written as [3]:

Continuity equation:

$$\frac{\partial v}{\partial z} + \frac{1}{r}\frac{\partial (ru)}{\partial r} = 0 \tag{2.1}$$

z-momentum equation:

$$\rho\left(\frac{\partial v}{\partial t} + u\frac{\partial v}{\partial r} + v\frac{\partial v}{\partial z}\right) = -\frac{\partial p}{\partial z} + \left(\frac{1}{r}\frac{\partial}{\partial r}\left(\mu\left(\frac{\partial v}{\partial r} + \frac{\partial u}{\partial z}\right)\right)\right) + 2\frac{\partial}{\partial z}\left(\mu\frac{\partial v}{\partial z}\right) - g\beta(T - T_{ref}) \tag{2.2}$$

r-momentum equation:

$$\rho\left(\frac{\partial u}{\partial t} + u\frac{\partial u}{\partial r} + v\frac{\partial u}{\partial z}\right) = -\frac{\partial p}{\partial r} + \left(\frac{2}{r}\frac{\partial}{\partial r}\left(\mu r\frac{\partial u}{\partial r}\right)\right) + \frac{\partial}{\partial z}\left(\mu\left(\frac{\partial v}{\partial r} + \frac{\partial u}{\partial z}\right)\right) \tag{2.3}$$

Energy equation:

$$\rho C\left(\frac{\partial T}{\partial t} + u\frac{\partial T}{\partial r} + v\frac{\partial T}{\partial z}\right) = \frac{1}{r}\frac{\partial}{\partial r}\left(rK\frac{\partial T}{\partial r}\right) + \frac{\partial}{\partial z}\left(K\frac{\partial T}{\partial z}\right) + \Phi + S_r \tag{2.4}$$

where Φ is the viscous dissipation term and S_r is the radiation source term. Φ is kept

only for the glass flow due to the high viscosity of glass.

$$\Phi = \mu\left(2\left[\left(\frac{\partial u}{\partial r}\right)^2 + \left(\frac{u}{r}\right)^2 + \left(\frac{\partial v}{\partial z}\right)^2\right] + \left(\frac{\partial v}{\partial r} + \frac{\partial u}{\partial z}\right)^2\right) \tag{2.5}$$

The Boussinesq approximation [22] is used for the buoyancy effects.

Since the flows in three regions are all taken as axisymmetric, a vorticity stream-function approach is advantageous to use for solving this problem [30]. The stream function and vorticity are defined as,

$$u = -\frac{1}{r}\frac{\partial \psi}{\partial z} \tag{2.6}$$

$$v = \frac{1}{r}\frac{\partial \psi}{\partial r} \tag{2.7}$$

$$\omega = \frac{\partial u}{\partial z} - \frac{\partial v}{\partial r} \tag{2.8}$$

Then the governing equations for the stream function and vorticity are obtained as,

$$\frac{\partial}{\partial r}\left(\frac{1}{r}\frac{\partial \psi}{\partial r}\right) + \frac{\partial^2}{\partial z^2}\left(\frac{\psi}{r}\right) = -\omega \tag{2.9}$$

$$\rho\left(\frac{\partial \omega}{\partial t} + \frac{\partial\left(u\omega\right)}{\partial r} + \frac{\partial\left(v\omega\right)}{\partial z}\right) = \mu\left(\frac{\partial}{\partial r}\left(\frac{1}{r}\frac{\partial\left(r\omega\right)}{\partial r}\right) + \frac{\partial^2 \omega}{\partial z^2}\right) + S_\mu \tag{2.10}$$

where S_μ is the source term due to the variable viscosity and is given as,

$$\begin{aligned} S_\mu &= \frac{\partial \mu}{\partial z}\left(2\frac{\partial^2 u}{\partial r^2} + 2\frac{\partial^2 u}{\partial z^2} + \frac{2}{r}\frac{\partial u}{\partial r} - 2\frac{u}{r^2}\right) \\ &\quad -\frac{\partial \mu}{\partial r}\left(2\frac{\partial^2 v}{\partial r^2} + 2\frac{\partial^2 v}{\partial z^2} + \frac{1}{r}\left(\frac{\partial v}{\partial r} + \frac{\partial u}{\partial z}\right)\right) \\ &\quad + \left(\frac{\partial^2 \mu}{\partial z^2} - \frac{\partial^2 \mu}{\partial r^2}\right)\left(\frac{\partial u}{\partial z} + \frac{\partial v}{\partial r}\right) + 2\frac{\partial^2 \mu}{\partial r \partial z}\left(\frac{\partial u}{\partial r} - \frac{\partial v}{\partial z}\right) \end{aligned} \tag{2.11}$$

To include radiation heat transfer in the furnace, the optically thick method is applied to model the radiative transport within glass here. A more accurate method, the zonal method, is used in the next chapter. In the optically thick method, the effect of radiation within glass is considered as thermal diffusion. So the radiation source term S_r in Equation (2.4) equals to zero. The resulting radiative conductivity can be obtained from Equation (2.12), given below:

$$\begin{aligned} K &= K_c(T) + K_r(T), \\ K_r &= \frac{16 n^2 \sigma T^3}{3a} \end{aligned} \tag{2.12}$$

In the optically thick method, surface heat flux due to radiation must be taken into account. In hollow fiber drawing, the radiative heat flux at the outer neck-down profile can be determined by considering the enclosure outside the glass, which is comprised of the furnace wall, the outer neck-down profile and two end-gaps. The radiative heat flux at the inner neck-down profile can be calculated by considering the enclosure inside the glass, which is comprised of the inner neck-down profile and two end-gaps. This method is very simple. However, a medium is considered to be optically thick when its optical thickness is greater than 5 [61]. In the lower neck-down region, because the thickness of the fiber is very small (around 30 μm), the optical thickness is less than 5. So, the optically thick assumption is not applicable in the lower neck-down region. The optically thick method is not very accurate, especially in the lower neck-down region.

2.2.2 Boundary conditions

The boundary conditions are schematic shown in Figure 2.2 and specified as given below:

At the top of the preform ($z = 0, R_{10} \leq r \leq R_{20}$):

$$u = 0, v = V_0, T = T_0$$

At the fiber exit ($z = L, R_1(L) \leq r \leq R_2(L)$), axial diffusion is neglected, i.e.,

$$\frac{\partial^2 u}{\partial z^2} = 0, \frac{\partial^2 v}{\partial z^2} = 0, \frac{\partial^2 T}{\partial z^2} = 0$$

Along the furnace wall ($r = R_F, 0 \leq z \leq L$):

$$u = v = 0, T = T_w(z)$$

Along the axis ($r = 0, 0 \leq z \leq L$) due to symmetry:

$$u = 0, \frac{\partial v}{\partial r} = 0, \frac{\partial T}{\partial r} = 0$$

At the top of external purge gas ($z = 0, R_{20} \leq r \leq R_F$):

$$u = 0, v = V_a, T = T_0$$

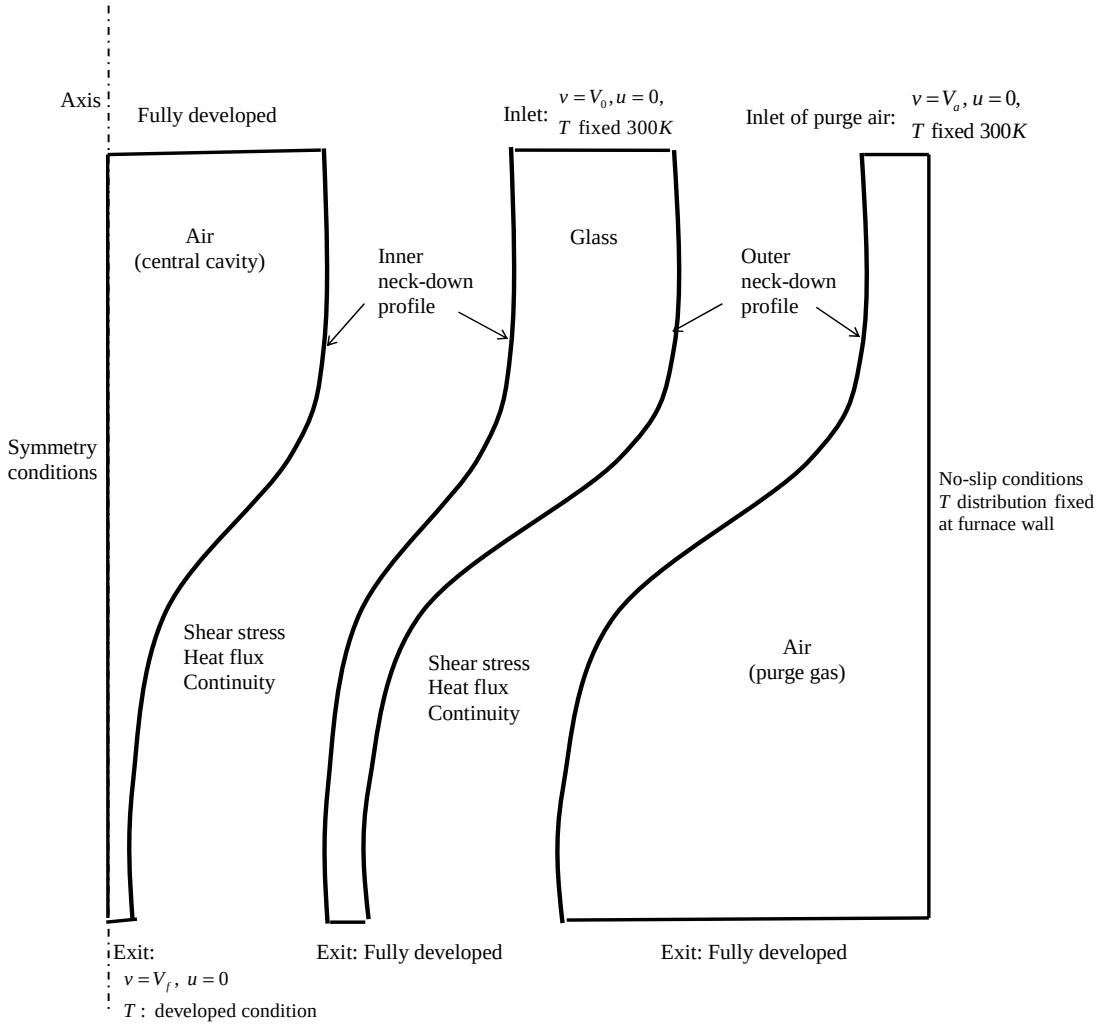

Figure 2.2: Boundary conditions in the model

At the exit of external purge gas ($z = L, R_2(L) \leq r \leq R_F$):

$$\frac{\partial^2 u}{\partial z^2} = 0, \frac{\partial^2 v}{\partial z^2} = 0, \frac{\partial^2 T}{\partial z^2} = 0$$

Along the interfaces ($r = R_1(z)$ and $r = R_2(z)$), the stream-function values are set equal to constant values and a force balance and continuity of velocity, temperature and heat flux are applied. The relations for velocity are obtained from the balance of tangential stresses, which can be written as:

$$\mu \left.\frac{\partial v}{\partial n}\right|_1 = \mu_a \left.\frac{\partial v}{\partial n}\right|_{1(c)}$$

$$\mu \left.\frac{\partial v}{\partial n}\right|_2 = \mu_a \left.\frac{\partial v}{\partial n}\right|_{2(a)}$$

The surface tension effects are essentially neglected because the surface tension between glass and gas (air) is very small [39, 53]. At the interfaces, the normal velocity is zero. Therefore,

$$u = v \cdot tan(\theta) = v\frac{dR}{dz}$$

The continuity of heat flux can be expressed as:

$$-K \left.\frac{\partial T}{\partial n}\right|_1 = -K_a \left.\frac{\partial T}{\partial n}\right|_{1(c)} + q_{flux}$$
$$-K \left.\frac{\partial T}{\partial n}\right|_2 = -K_a \left.\frac{\partial T}{\partial n}\right|_{2(a)} + q_{flux}$$

At the top of the inner central cavity ($z = 0, 0 \leq r \leq R_{10}$):

$$\frac{\partial^2 u}{\partial z^2} = 0, \frac{\partial^2 v}{\partial z^2} = 0, \begin{cases} \frac{\partial^2 T}{\partial z^2} = 0 & \text{when } v < 0 \\ T = T_0 & \text{when } v \geq 0 \end{cases}$$

At the bottom of the inner central cavity ($z = L, 0 \leq r \leq R_1(L)$):

$$u = 0, v = V_f, \frac{\partial^2 T}{\partial z^2} = 0$$

where V_f is the drawing speed, i.e., the velocity of the fiber at the exit. Since the diameter of the central cavity at the bottom is very small (about 50 μm) and the fiber moves very fast (about 10 m/s) at the exit, the assumption that gas at the exit of the central cavity will move at the same speed as the adjacent fiber velocity due to the viscous drag is reasonable and is applied. The stream-function value at the interface $r = R_1$ is set equal to zero as a reference value of the stream function.

2.2.3 Coordinate transformation

Three regions (the central cavity, the glass layer and the external gas regions) are transformed to regular cylindrical regions first. The transformed coordinate systems for the three regions are given below [5, 8],

In the central cavity:

$$\eta = \frac{r}{R_1(z)}, \beta = \frac{z}{L} \tag{2.13}$$

In the glass layer:

$$\eta = \frac{r - R_1(z)}{R_2(z) - R_1(z)}, \beta = \frac{z}{L} \tag{2.14}$$

In the external gas region:

$$\eta = \frac{R_F - r}{R_F - R_2(z)}, \beta = \frac{z}{L} \tag{2.15}$$

The equations and boundary conditions are all transformed to the new coordinates, as discussed in detail by Chen and Jaluria [5]. The equations in terms of non-dimensional variables under the transformed coordinates are shown in Appendix A.

2.3 Correction of the neck-down profiles

The neck-down profiles at steady state are influenced by the drawing conditions. The major difference between the drawing process of the hollow fiber and the solid-core fiber is that it is necessary to determine and control one additional profile, the neck-down profile of the central cavity. Here a correction scheme for the neck-down profiles in hollow fiber drawing is proposed. The two neck-down profiles of the hollow fiber are determined based on the balance of the surface forces and mass conservation. Since the variation of pressure in the radial direction is quite small, which is proved by the analyses of Fitt et al [18], radially lumped pressure is employed in the correction scheme. A one dimensional lumped axial velocity assumption is reasonable for the correction scheme as noted by earlier studies on the velocity distribution. As given by Paek and Runk [48], the expression for axial velocity can be written as follow:

$$V_z = V_0 + C_1 \int_0^z \frac{dz}{\mu\left(R_2^2 - R_1^2\right)} - \frac{\rho g}{3} \int_0^z \frac{1}{\mu\left(R_2^2 - R_1^2\right)} \left(\int_0^z \left(R_2^2 - R_1^2\right) dz \right) dz$$
$$- \frac{4}{3} \int_0^z \left(\frac{\int_0^z \left(\xi_2 R_2' R_2 H_2 - \xi_1 R_1' R_1 H_1\right) dz}{\mu\left(R_2^2 - R_1^2\right)} \right) dz \tag{2.16}$$

where

$$C_1 = \frac{(V_f - V_0) + \frac{\rho g}{3} \int_0^L \frac{\int_0^z \left(R_2^2 - R_1^2\right) dz}{\mu\left(R_2^2 - R_1^2\right)} dz + \frac{4}{3} \int_0^L \frac{\int_0^z \left(\xi_2 R_2' R_2 H_2 - \xi_1 R_1' R_1 H_1\right) dz}{\mu\left(R_2^2 - R_1^2\right)} dz}{\int_0^L \frac{1}{\mu\left(R_2^2 - R_1^2\right)} dz}$$

$$H = \frac{1}{2} \frac{\frac{1}{R}\left(1 + \left(\frac{dR}{dz}\right)^2\right) - \frac{d^2R}{dz^2}}{\left(1 + \left(\frac{dR}{dz}\right)^2\right)^{1.5}} \tag{2.17}$$

Here, H is the mean curvature of the surface. Once the axial velocity is determined, a relationship between the two neck-down profiles is obtained from the mass conservation equation, as:

$$R_2(z)^2 - R_1(z)^2 = \frac{\left(R_{20}^2 - R_{10}^2\right) V_0}{V_z} \tag{2.18}$$

It is necessary to get one more equation to determine the two neck-down profiles. The normal force balance equations at the two profiles are expressed as follows:

$$p(z) - p_c = 2\mu \left.\frac{\partial u_n}{\partial n}\right|_1 - 2\mu_a \left.\frac{\partial u_n}{\partial n}\right|_c - 2\xi_1 H_1 \tag{2.19}$$

$$p(z) - p_a = 2\mu \left.\frac{\partial u_n}{\partial n}\right|_2 - 2\mu_a \left.\frac{\partial u_n}{\partial n}\right|_a + 2\xi_2 H_2 \tag{2.20}$$

where $\frac{\partial u_n}{\partial n}$ can be written as:

$$\frac{\partial u_n}{\partial n} = \frac{\frac{\partial u}{\partial r} - \frac{dR}{dz}\left(\frac{\partial v}{\partial r} + \frac{\partial u}{\partial z}\right) + \frac{\partial v}{\partial z}\left(\frac{dR}{dz}\right)^2 + v\frac{dR}{dz}\frac{d^2R}{dz^2}}{1 + \left(\frac{dR}{dz}\right)^2} \tag{2.21}$$

By eliminating pressure $p(z)$ and ignoring the contributions of the normal stresses caused by gas shear, which are very small compared with other terms in the equations due to very small gas viscosity, we obtain the follow equation,

$$2\mu \left.\frac{\partial u_n}{\partial n}\right|_2 - 2\mu \left.\frac{\partial u_n}{\partial n}\right|_1 = -2(\xi_1 H_1 + \xi_2 H_2) - (p_a - p_c) \tag{2.22}$$

Also, due to radially lumping of the axial velocity, $v = v(z)$. The velocity component in the r direction, $u(r, z)$, can be determined from the continuity equation, as

$$u = -\frac{1}{2}\frac{dv}{dz}r + \frac{c(z)}{r} \tag{2.23}$$

where $c(z)$ is a function of z. The expression for u at the interface $r = R_1$ can be obtained from the boundary condition:

$$u|_{r=R_1} = v\frac{dR_1}{dz} \tag{2.24}$$

Then plugging the expression for the velocity components into equation (2.21), we end up with:

$$\left.\frac{\partial u_n}{\partial n}\right|_1 = -v\frac{1}{R_1}\frac{dR_1}{dz} - \frac{dv}{dz} \tag{2.25}$$

At the interface $r = R_2$, we also get:

$$\left.\frac{\partial u_n}{\partial n}\right|_2 = -v\frac{1}{R_2}\frac{dR_2}{dz} - \frac{dv}{dz} \tag{2.26}$$

Now the equation (2.22) can be reduced to:

$$\frac{R_1(z)}{R_2(z)} = \frac{R_{10}}{R_{20}} exp\left(\int_0^z \frac{1}{2\mu v}(-2(\xi_1 H_1 + \xi_2 H_2) + \Delta p)dz\right) \tag{2.27}$$

Where $\Delta p = p_a - p_c$ Thus, the inner and outer profiles can be determined from equations (2.18) and (2.27).

2.4 Numerical scheme

A finite difference method is applied to solve the problem. The non-uniform grid scheme developed by Lee [37] is applied for the present study. The optimal grid numbers are determined when the mesh-independent results are obtained. The optimal grid size for the transport equations is obtained as 369×41 (in axial and radial directions, respectively) for the central cavity, 369×21 for the fiber region and 369×61 for the external gas region. The stream function, vorticity and energy equations are solved by using the false transient scheme. These equations are discretized using second-order central differencing and are solved using an alternating direction implicit (ADI) approach by alternating traverses in the z and r directions, respectively. Successive Under-Relaxation (SUR) is applied because the equations are highly non-linear and coupled due to the temperature dependent viscosity of glass. In order to save computational time, the neck-down profiles are corrected before the steady state is reached. This strategy was proposed by Roy Choudhury [54]. And Roy Choudhury has demonstrated that 1500-2000 steps are adequate for the purpose of neck-down profile correction within a reasonable number of corrective iterations. Therefore, the above false transient iterative procedure is carried out for about 1500 steps for any given neck-down profiles. Then the neck-down profiles are modified by the numerical corrective procedure. For further details on the numerical scheme, see Roy Choudhury and Jaluria [53].

In the profile correction procedure, the axial velocity distribution is calculated from equation (2.16) when the preform feeding speed and the drawing speed are given. Then

equations (2.18) and (2.27) are used to get the inner and outer diameters of the final hollow fiber. However in most practical cases, the outer diameter of the final hollow fiber and the drawing speed are given, not the preform feeding speed. In solid-core fiber drawing, the preform feeding speed can be calculated by the mass conservation, provided the diameter of the fiber and the drawing speed are given. But in hollow fiber drawing, the preform feeding speed can not be calculated by the mass conservation due to the unknown inner diameter of the final hollow fiber. The preform feeding speed must be adjusted to make the outer diameter of the final fiber reach the target value, typically 125 μm. The numerical corrective procedure for an unknown preform feeding speed is shown in Figure 2.3. First a guessed preform feeding speed is used to obtain the temporary axial velocity distribution and radius ratio between inner and outer neck-down profiles. Then the preform feeding speed is modified by using the temporary final inner diameter and the neck-down profiles for this corrective step are calculated. The convergence criterion was varied, along with the grid, to ensure the results are independent of values chosen. The convergence criterion were obtained as 10^{-4} for the stream function, vorticity and temperature and the neck-down profiles. It typically takes about 10$\sim$15 neck-down profiles iterative steps to achieve the converged neck-down profiles.

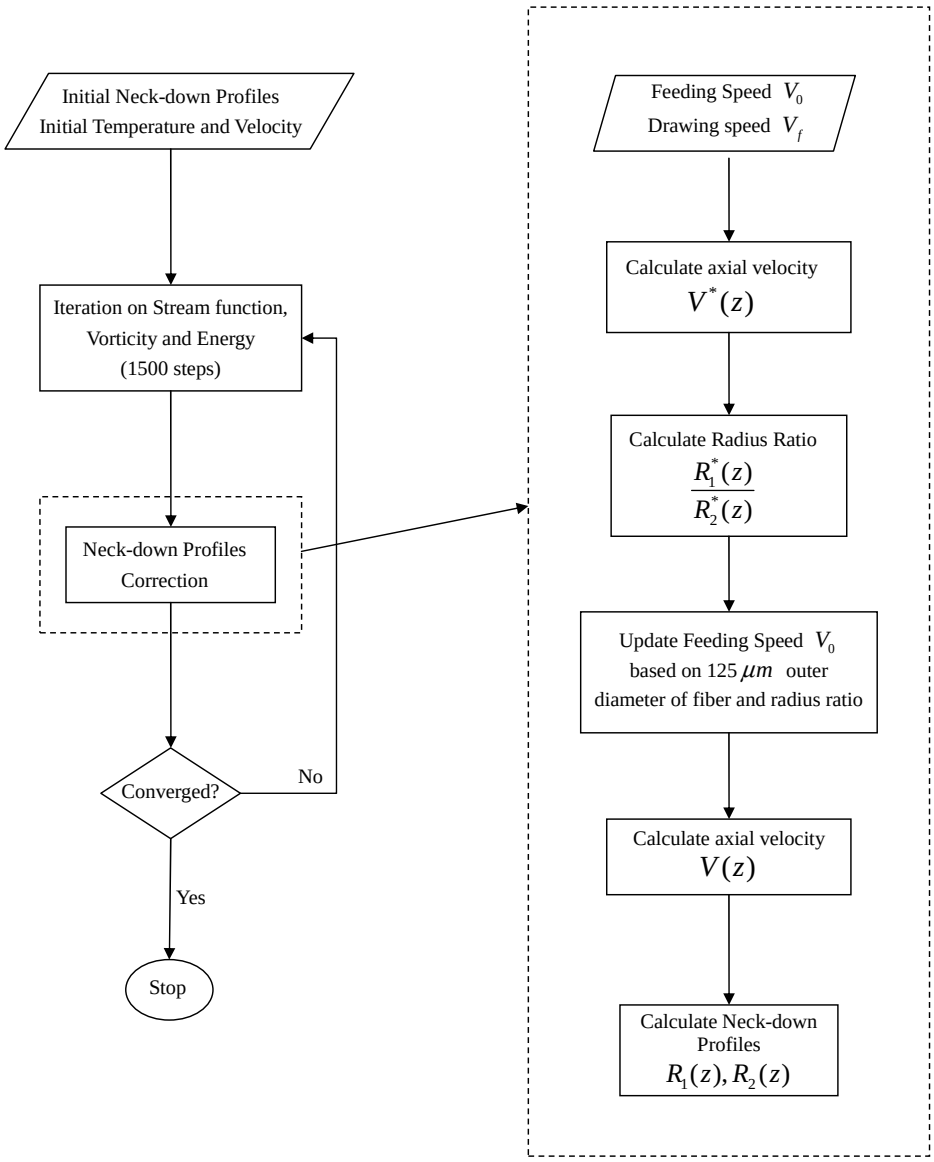

Figure 2.3: Numerical procedure for hollow optical fiber drawing process

2.5 Results

2.5.1 Validation

In order to check the validity of the method, comparisons were made with the theoretical predictions from Fitt et al [18]. The inner and outer diameters of the preform are the same as mentioned in the paper. The furnace length is chosen to be 30 cm and the temperature profile along the furnace is assumed to be parabolic, the maximum temperature of which is referred to as the furnace temperature. It is clear from Figure 2.4 that the results from the present model match the results from Fitt et al very well. It is physically expected that faster drawing speeds, higher furnace temperature and lower preform feeding speeds all result in small final inner and outer diameters of the final hollow fiber. The experiments from Fitt et al show that the collapse of the central cavity occurs and the radius ratio of the final hollow fiber increases with an increase in the preform feeding speed or a decrease in the furnace temperature. All these trends are consistent with the trends for collapse ratio, as discussed previously.

The comparisons between the results from the present model and results from solid-core fiber are also carried out. The neck-down profiles for the hollow fiber for different preform radius ratios and the profile for the solid-core fiber by using the optically thick method are shown in Figure 2.5. The thicker black line is the neck-down profile for solid-core fiber. The preform outer diameters of hollow fibers and solid-core fiber are all equal to 5 cm. All the other drawing parameters are the same. It is seen from Figure 2.5 that the outer neck-down profile moves closer to the profile of solid-core fiber when the preform radius ratio decreases. This trend is reasonable because the solid-core fiber can be regarded as the limiting case of the hollow fiber with the zero preform radius ratio.

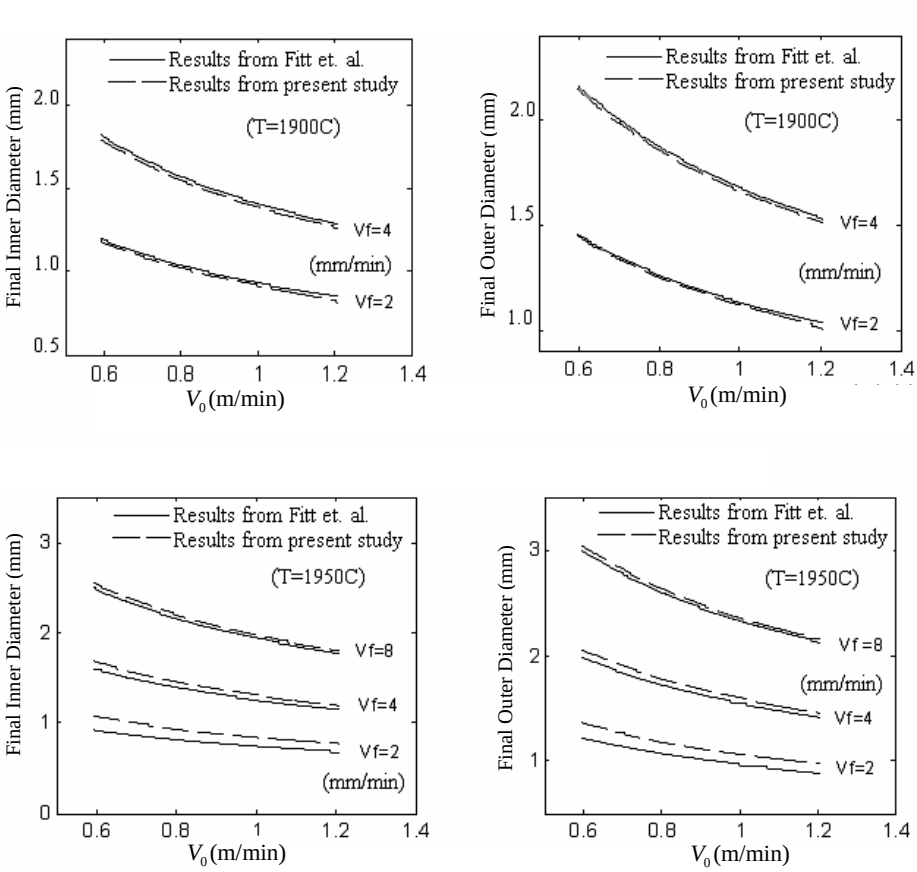

Figure 2.4: Prediction of the geometry of the final hollow fiber and the results from Fitt et al (2001)

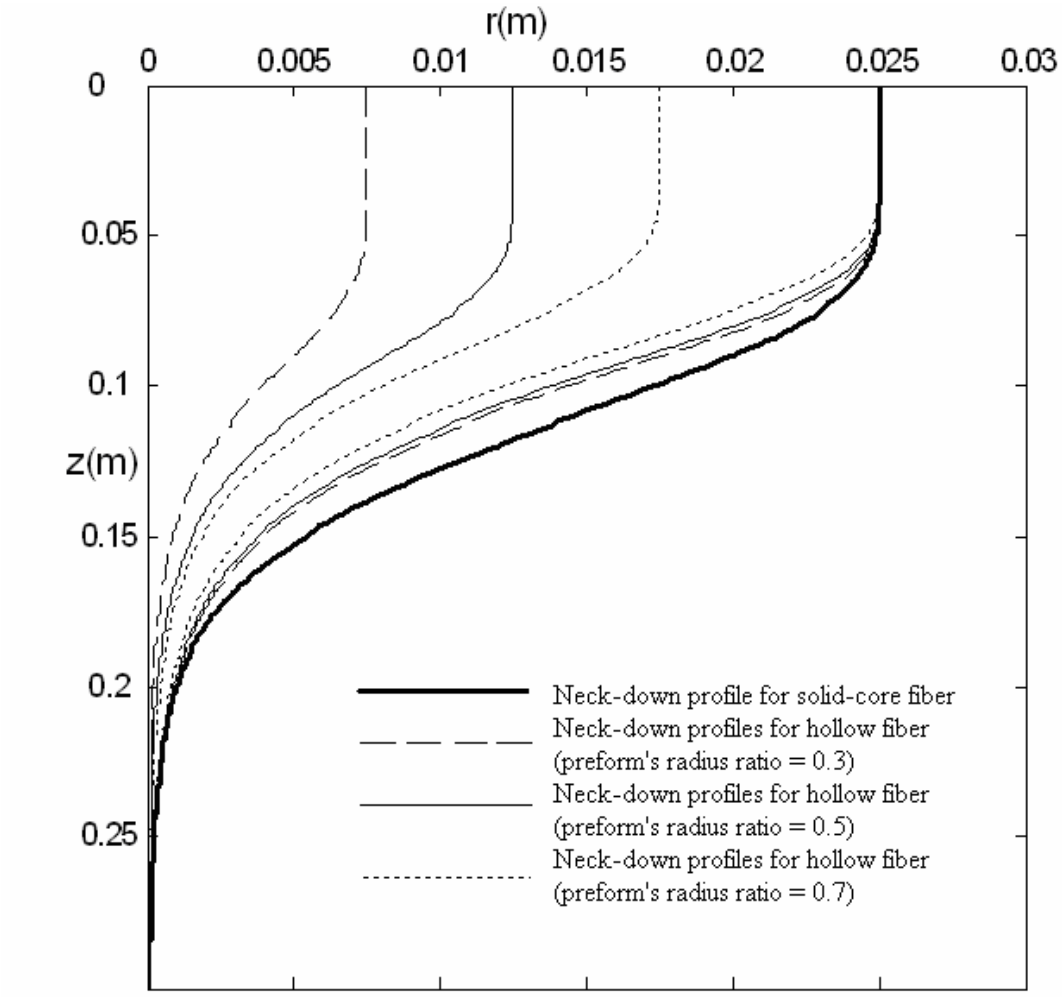

Figure 2.5: Neck-down profiles for different perform radius ratios and for a solid-core fiber

Table 2.1: Drawing parameters for a typical case

Furnace Diameter	Furnace Length	Preform Inner Diameter	Preform Outer Diameter
7 cm	30 cm	2.5 cm	5 cm
outer diameter of fiber	Drawing Speed	Inlet Velocity of the purge gas	
125 μm	10 m/s	0.1 m/s	

2.5.2 Parametric study

The combined conduction, convection and radiation heat transport problem in hollow fiber drawing is studied first. The properties of the gas, taken as Nitrogen at 300 K, are assumed to be constant. The glass properties taken from Fleming [20] are shown in Appendix B. Unless otherwise mentioned, the drawing conditions are given in Table 2.1. The furnace temperature is assumed to be a parabolic profile with the maximum in the middle and minimum at the two ends. The maximum furnace temperature is 2500 K and minimum is 2000 K. Pressurization of the gas in the core is neglected. The temperature of the preform T_0 is 300 K.

The results in terms of streamlines and isotherms for a typical case are shown in Figure 2.6. The thicker black lines in Figure 2.6 present the two neck-down profiles. The values of the isotherms are the non-dimensional temperature, with the softening temperature of silica glass 1900 K as the characteristic temperature. It is clear that the flow and temperature distributions in the fiber and in the external gas in hollow fiber drawing are similar to those in solid-core fiber drawing [53]. In the central cavity, the gas enters from the top boundary near the axis. One part of the gas quickly flows outward at the top boundary due to buoyancy effects. The other part flows down and leaves at the bottom boundary due to the fiber viscous drag. The magnitude of the velocity of the natural convection flow is so small that thermal diffusion dominates in the central cavity.

Surface heat fluxes due to radiation along the two neck-down surfaces are shown in Figure 2.7 The surface heat flux due to radiation along the inner surface is almost zero compared with that along the outer surface. So the contribution of the surface

heat flux along the inner surface to the temperature distribution in the glass can be neglected in the optically thick method.

In order to investigate the bouyancy effect in the central cavity, a comparison of two cases with different Grashof number is carried out. The smaller Grashof number can be obtained by increasing the kinematic viscosity of gas. The streamlines and isotherms for a case with a smaller Grashof number are shown in Figure 2.8. The Grashof number for this case is two order of magnitude smaller than that for the typical case which shown in Figure 2.6. It is seen from Figure 2.8 that the effect of thermal buoyancy is so small that the flow in the central cavity is mainly caused by the viscous drag. There is no gas leaving at the top boundary. By comparing Figure 2.6 and 2.8, the temperature distribution almost does not change because conduction is still the dominant mode of heat transfer.

Then the effects of the inlet velocity of the purge gas on the flow and the temperature field are studied. Figure 2.9 shows the streamlines and isotherms for different inlet velocities of the purge gas. An opposing flow arises near the flow exit when the velocity is low. The gas adjacent to the fiber surface moves very fast due to the large drawing speed, which leads to this reverse flow. As the velocity increases, this reverse flow is swept away. This reverse flow causes the different temperature field of purge gas at the exit shown in isotherms for this case. Unlike the flow field at low inlet velocity of purge gas, circulation arises outside the neck-down region due to the high inlet velocity of purge gas. These phenomena are the same as that seen in the results for solid-core fiber drawing.

In order to study the effects of gases properties, Helium has been considered here since it has a much larger thermal conductivity than Nitrogen. Figure 2.10 shows the streamlines and isotherms for Helium. The thermal field of purge gas is quite different from that shown in Figure 2.6 for Nitrogen. Helium heats up more quickly to a higher temperature level due to its higher thermal conductivity. This explains why the isotherms for Helium at the external gas region are much flatter than those for Nitrogen.

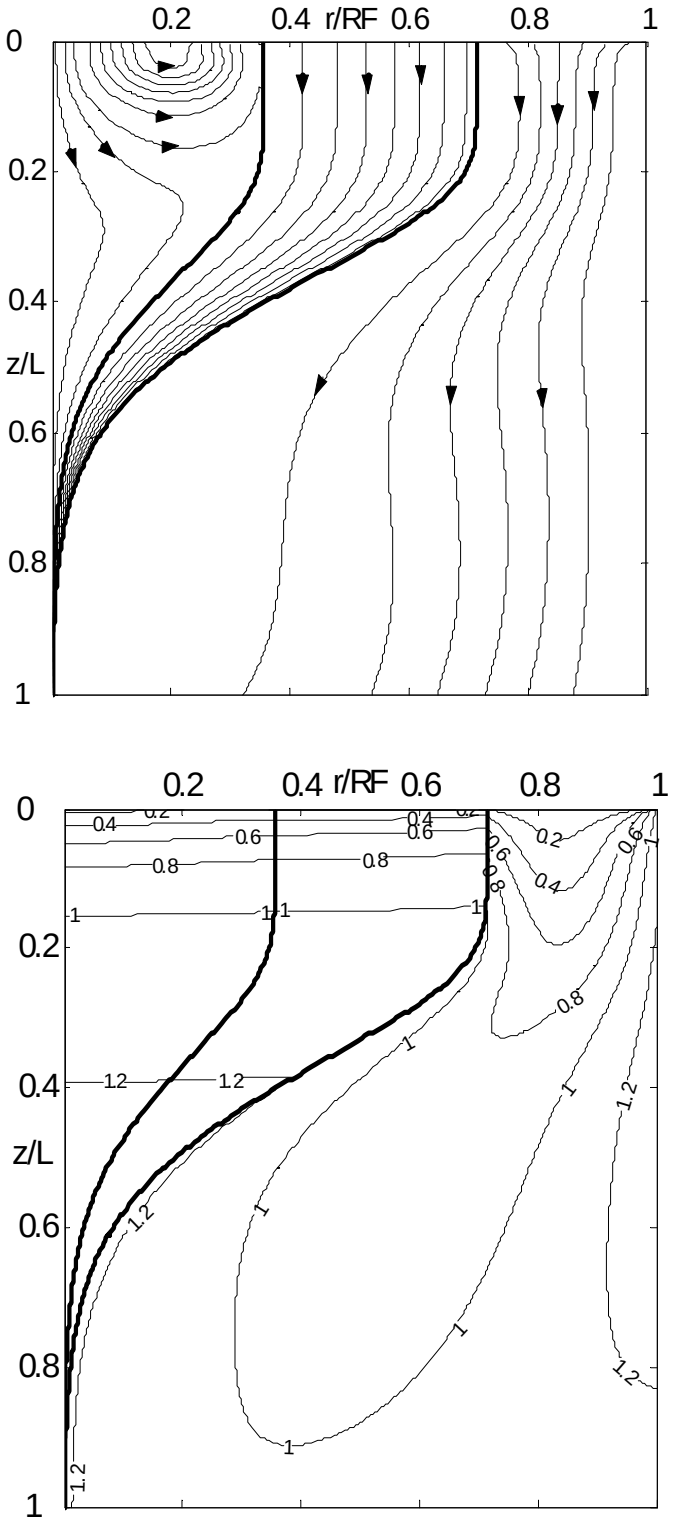

Figure 2.6: Streamlines and isotherms in the furnace for a typical case with a parabolic furnace temperature distribution (maximum: 2500 K, minimum: 2000 K) at a drawing speed of 10m/s

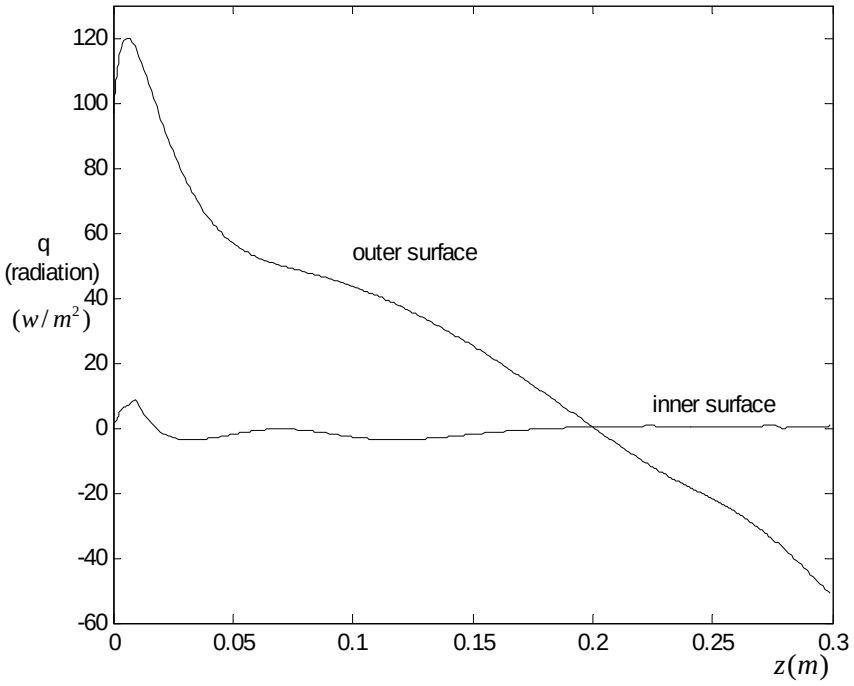

Figure 2.7: Surface heat fluxes due to radiation at the two neck-down surfaces

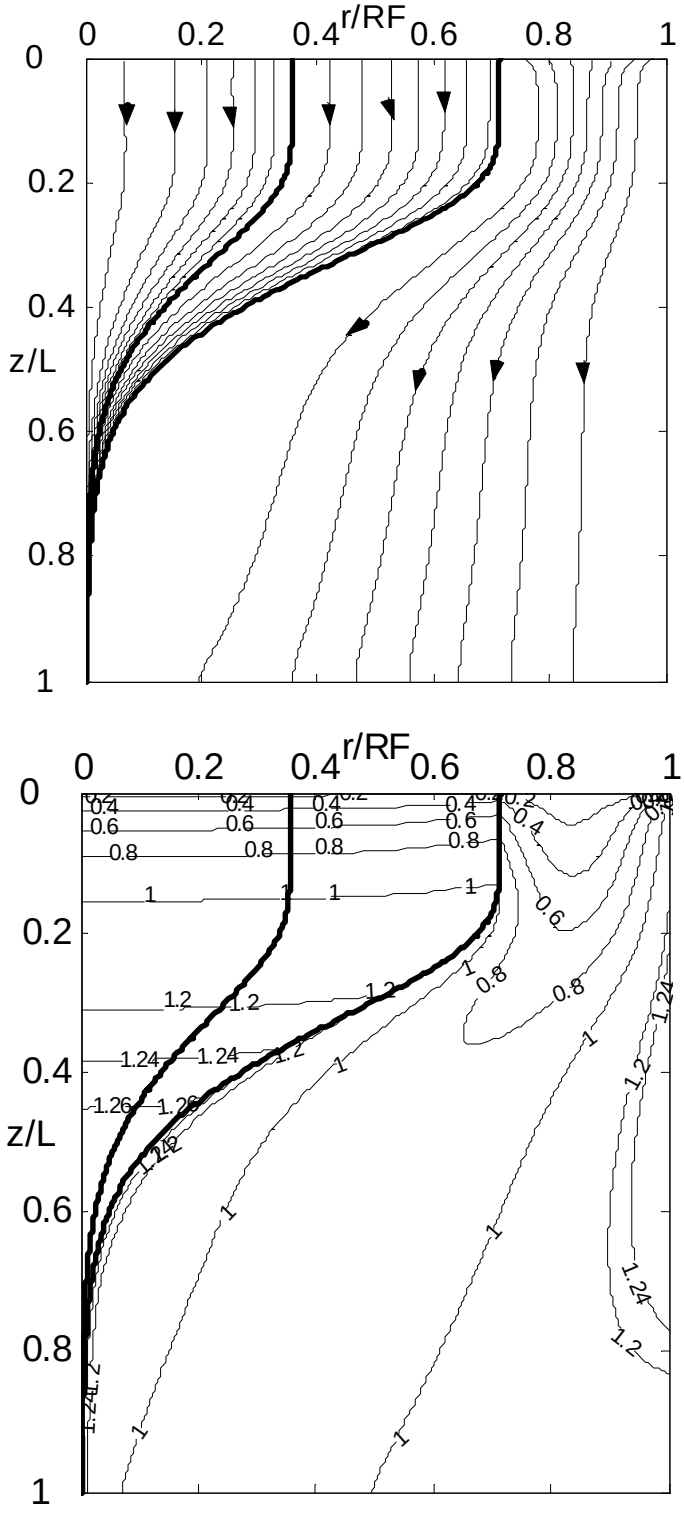

Figure 2.8: Streamlines and isotherms for a case with smaller Gr number

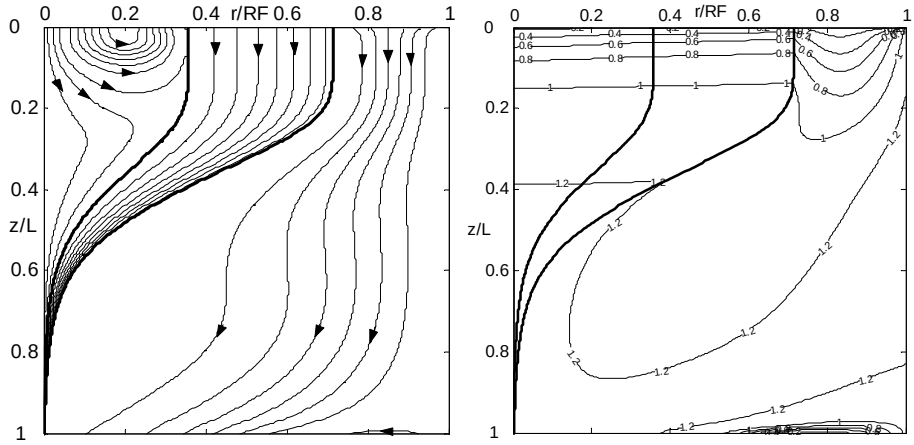

(a) Va=0.05m/s

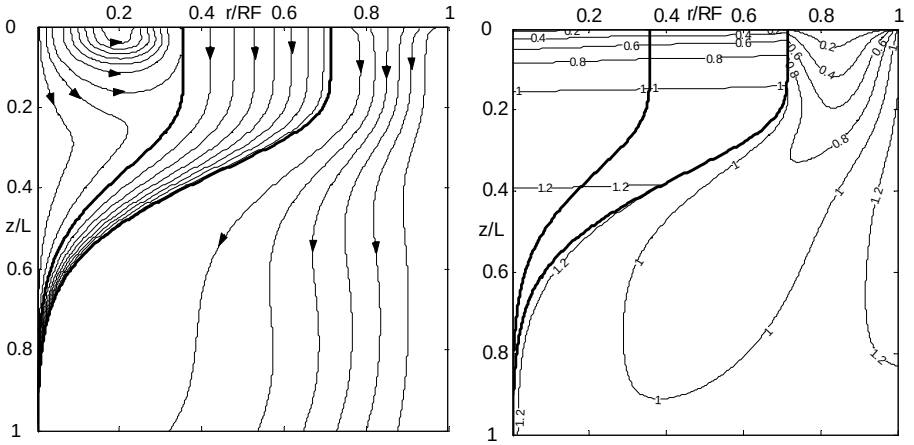

(a) Va=0.1m/s

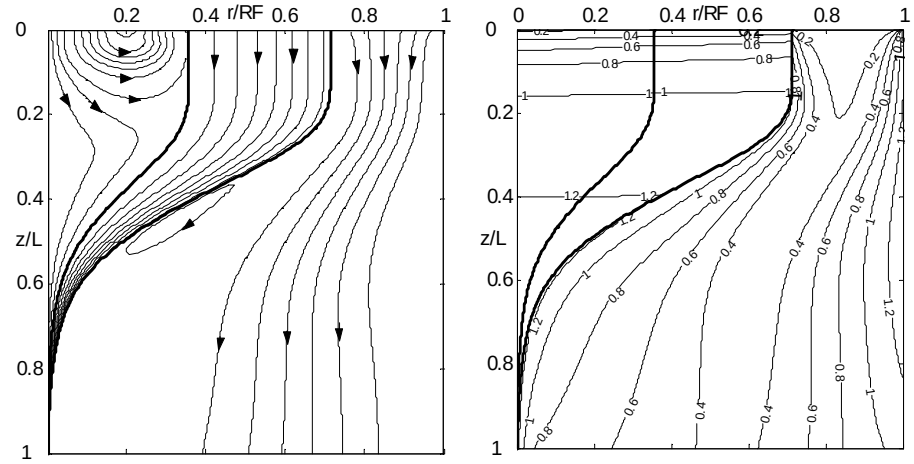

(a) Va=0.5m/s

Figure 2.9: Streamlines and isotherms for different external flow velocity

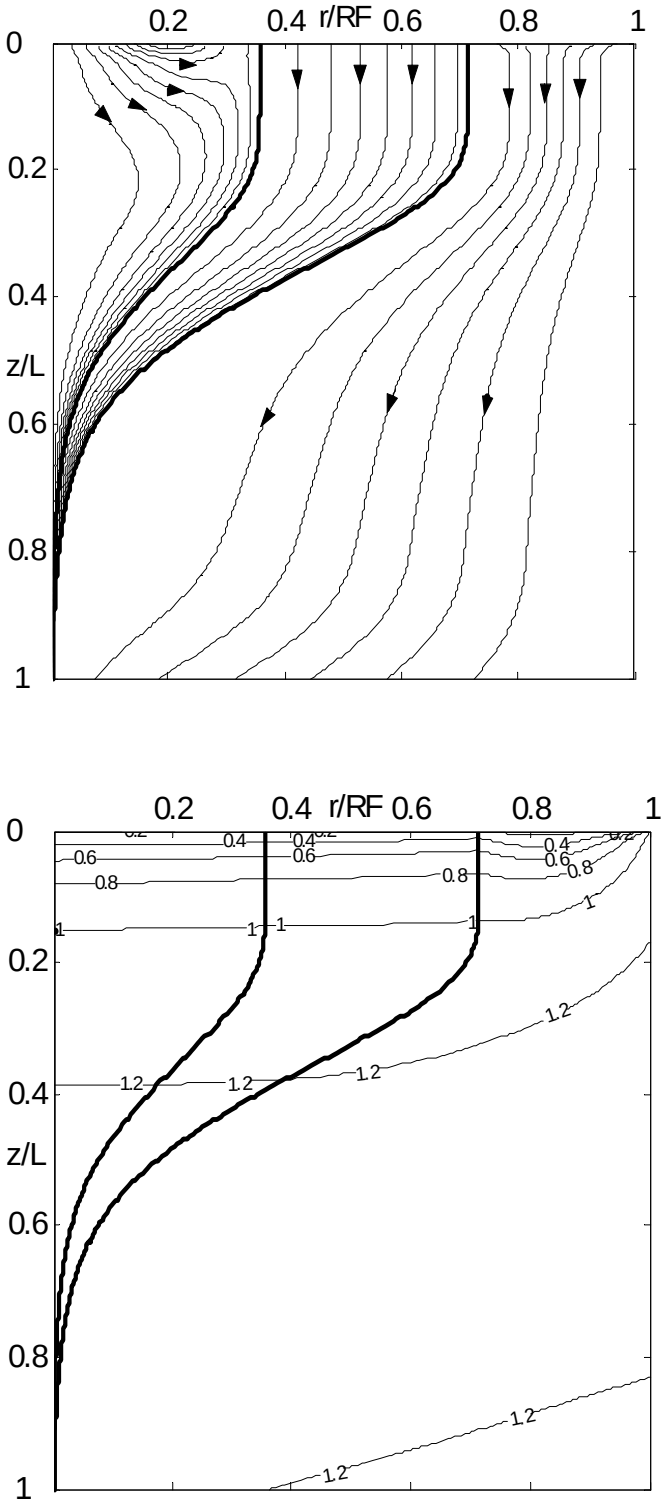

Figure 2.10: Streamlines and isotherms for Helium

2.5.3 Collapse ratio

Several physical and drawing process parameters are varied to study their effects on the geometry of the final hollow fiber. The starting neck-down profiles are taken as the results for the solid-core double-layer fiber. The profile correction scheme is applied to get the final converged neck-down profiles. The default preform radius ratio is equal to 0.5. The preform feeding speed and the drawing speed are fixed and the outer diameter of the final hollow fiber is decided by the model. The base preform feeding speed and the drawing speed are taken as 3.75 mm/min and 10 m/s, respectively. The furnace temperature profile is assumed to be parabolic. The base maximum and minimum furnace temperatures are 2500 K and 2000 K, respectively. The maximum temperature is referred to as the furnace temperature and the difference between the maximum and minimum temperatures is fixed at 500 K.

The effects of the preform feeding speed, the drawing speed and the drawing temperature on the collapse of the central cavity are studied. A collapse ratio C is defined to describe the collapse process, as:

$$C(z) = 1 - \frac{R_1(z)/R_2(z)}{R_{10}/R_{20}} \tag{2.28}$$

Thus, $C = 0$ when the radius ratio of the final fiber equals the initial radius ratio, and $C = 1$ when the central cavity is closed.

The drawing speed is varied from 1 m/s to 20 m/s and the preform feeding speed is in the range of 0.75 mm/min to 7.5 mm/min. The variations of the collapse ratio with the axial length, obtained from this model, for different preform feeding and drawing speeds and for different furnace temperatures are shown in Figure 2.11(a) and (b). It is seen in Figure 2.11(a) that the collapse ratio increases along with the axial length and increases with a decrease in the drawing speed or a decrease in the preform feeding speed. The effect of the preform feeding speed on the collapse ratio is much larger than that of the drawing speed. Figure 2.11(b) shows that the collapse ratio increases at larger furnace temperature. All these trends are similar to the results from Chakravarthy and Chiu [4]. The effects of drawing conditions on the collapse ratio are also studied further by the zonal method, which will be discussed in the next chapter.

2.5.4 Draw tension

The draw tension plays a very important role in the characteristics, quality and geometry of the final hollow fiber and can be practicably controlled during drawing process. The draw tension applied at the end of fiber is balanced with several forces. These forces are the viscous, surface tension, gravity, inertia and shear forces. The last one is exerted by the internal and external gas. Since the gas viscosity is small, compared with the viscosity of glass, the shear force due to internal and external gas can be ignored. As given by Manfre [41], the draw tension F_T for hollow fiber drawing can be expressed as:

$$\begin{aligned} F_T &= F_\mu + F_\xi + F_I - F_g \\ &= 3\pi\mu\left(R_2^2 - R_1^2\right)\frac{\partial v}{\partial z} + 2\pi\left(\xi R_2^2 H_2 + \xi R_1^2 H_1\right) \\ &\quad +\pi\rho\int_z^L \left(R_2^2 - R_1^2\right) v\frac{\partial v}{\partial z}dz - \pi\rho g\int_z^L \left(R_2^2 - R_1^2\right) dz \end{aligned} \tag{2.29}$$

Where F_μ is the force due to glass viscous stress, F_ξ is the force due to surface tension of the two neck-down profiles, F_I is the force due to inertia, F_g is the force due to gravity.

The draw tension and all the components calculated for a typical case are shown in Figure 2.12. All the forces in hollow fiber drawing have the same trends as in solid-core fiber. The overall draw tension is nearly constant along the axial direction and the contributions of the viscous force and gravity force dominate to determine the draw tension.

Figure 2.13 shows the effects of the drawing speed and the furnace temperature on the draw tension. Here, the outer diameter of the final hollow fiber is fixed as 125 μm. The preform feeding speed is decided by the model. The draw tension increases with an increase in the drawing speed at a given furnace temperature. The reason is that a faster drawing gives rise to greater viscous force. Draw tension decreases with an increase in furnace temperature for the same drawing speed due to reduced viscosity. Also the cross-sectional areas are smaller at higher furnace temperature. Therefore, higher furnace temperature or lower drawing speeds result in low draw tension. The draw tension is also investigated by the zonal method, which will be discussed in the next chapter.

2.5.5 Feasible domain

Combinations of parameters for feasible fiber drawing are identified for hollow fiber drawing by using the optically thick method. The outer diameter of the final hollow fiber is fixed to be 125 μm. The hollow fiber cannot be drawn at any arbitrary combination of critical drawing parameters. The furnace temperature and the drawing speed are investigated here since these are the most commonly varied parameters in practical systems. The air core may close at high furnace temperature or low drawing speeds. Also, the drawing process may fail at low furnace temperature or high drawing speeds because the drawing stress is higher than the glass breaking stress. Therefore, two limits exist for the drawing speed at the same furnace temperature. The glass breaking stress is about 100 Mpa, given by the empirical formula of Scholze [60]. Figure 2.14 shows the feasible domain for the drawing speed in the range of 1 m/s to 20 m/s and the furnace temperature in the range of 2400 K to 2700 K. The domain between two dash lines shown in Figure 2.14 is the feasible domain, in which the drawing process is possible. The slope of the upper dashed line is positive because the draw tension is small at higher furnace temperature and lower speeds. And the slope of the lower dashed line is also positive because it is easy for the central core to close at higher furnace temperature and lower drawing speeds.

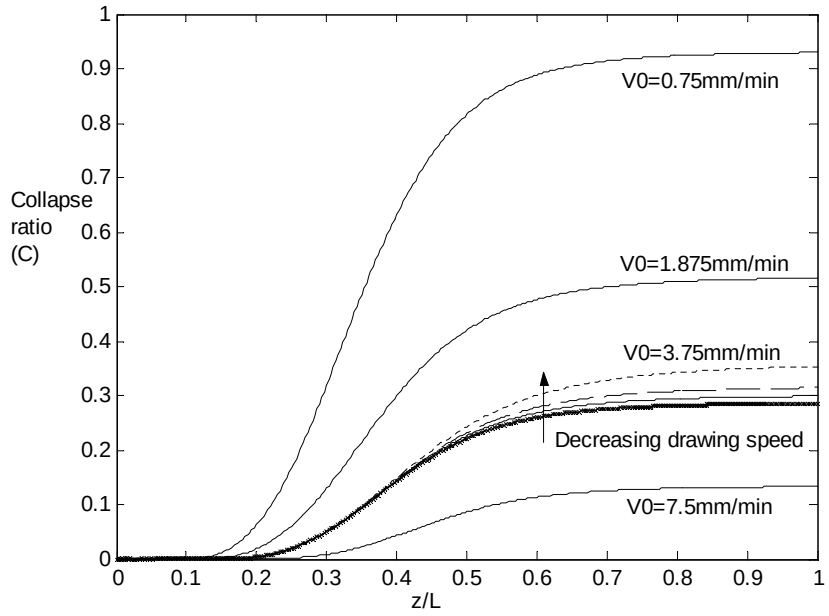

(a)

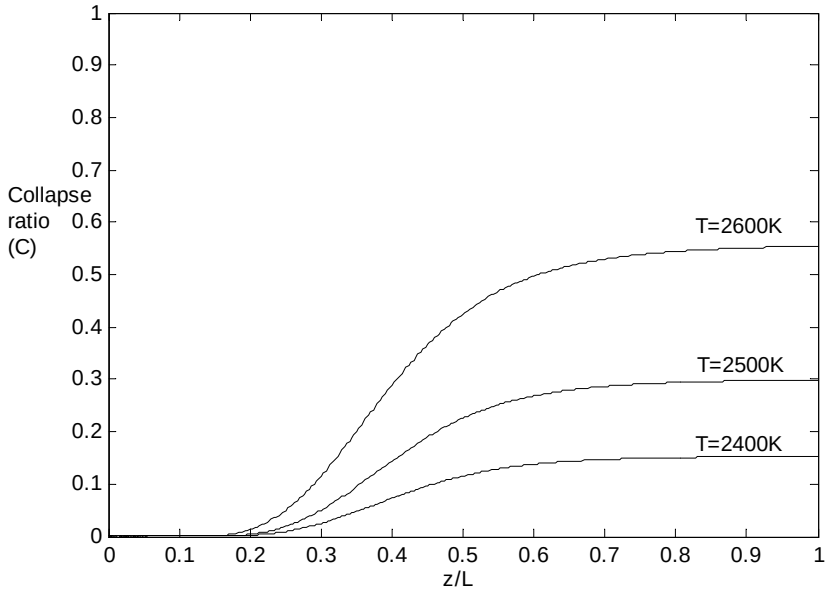

(b)

Figure 2.11: The variation of collapse ratio along the axial length for different (a) Drawing speeds and preform feeding speeds (b) Highest furnace temperatures

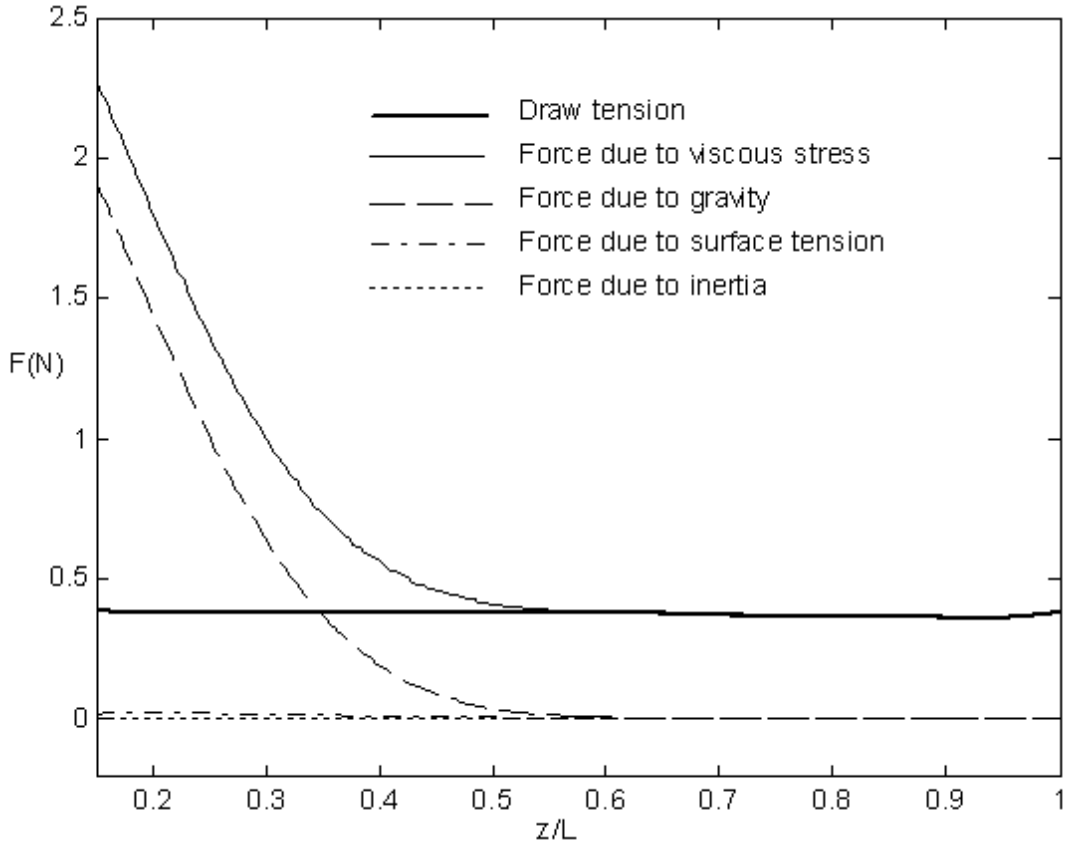

Figure 2.12: The variation of different force components and draw tension along the axis for a typical case

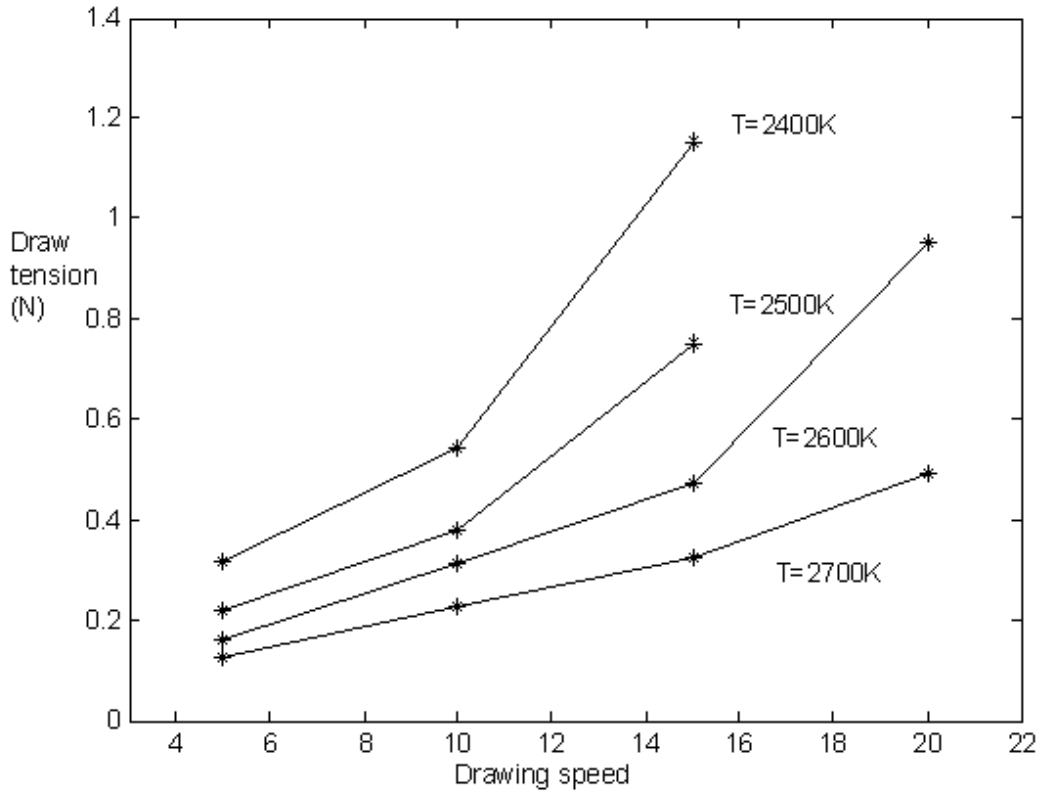

Figure 2.13: The variations of draw tension with the drawing speed for different furnace temperatures

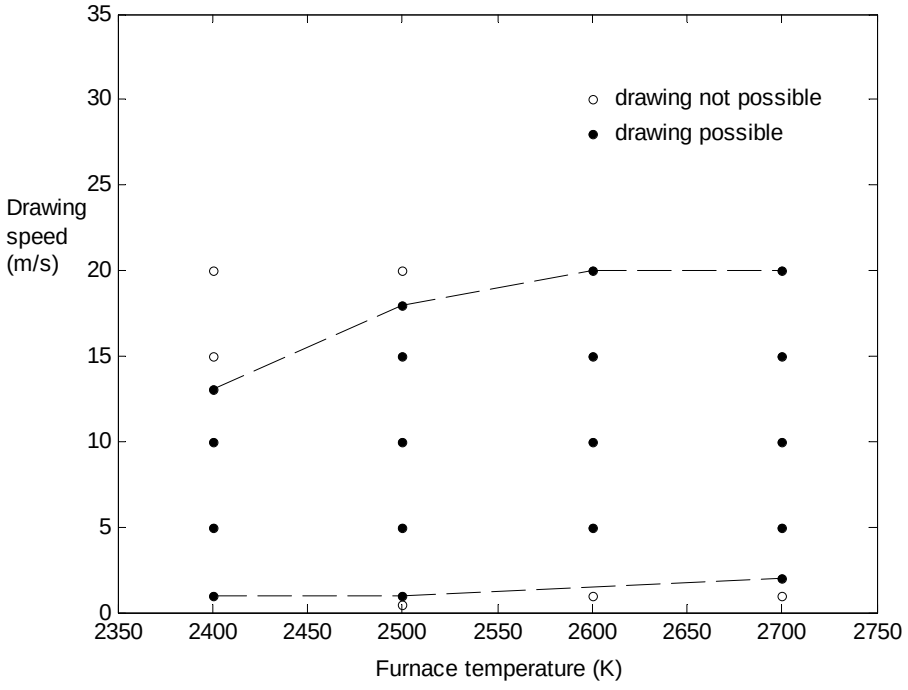

Figure 2.14: Feasible domain for a hollow fiber drawing with a parabolic furnace temperature distribution in terms of the drawing speed and the maximum furnace temperature

2.6 Summary

A numerical model has been presented for hollow glass fiber drawing with the generation of the two neck-down profiles. Equations (2.18) and (2.27) can be used to determine the inner and outer neck-down profiles. The optically thick method is applied in this chapter. The model can simulate the complex transport process of hollow fiber drawing, which involves a combination of conduction, natural and forced convection and radiation transport. The final fiber geometry is highly dependent on the drawing parameters. The collapse ratio and the draw tension are simply studied in this chapter. The collapse ratio of the final hollow fiber increases when the drawing speed or the preform feeding speed decreases or the furnace temperature increases. A faster drawing speed or preform feeding speed or lower furnace temperature can avoid the collapse of the central cavity. Draw tension, a crucial factor in the fiber quality, is nearly constant along the axial direction. Higher furnace temperature or lower drawing speeds can reduce the draw tension. The results from the model are validated by comparing with existing experimental and numerical results for hollow and solid fibers. It turns out that the results are in agreement with those in the literature. Finally, the feasible domain for hollow optical fiber drawing process is identified to guide the hollow fiber manufacture.

Chapter 3

Simulation of Hollow Optical Fiber Drawing with the Zonal Method for Radiation Transport

3.1 Introduction

The main mode of heat transfer in the drawing furnace is radiation. Glass is considered to be a participating media. To calculate the radiative transport in the glass, the optically thick approximation (also called Rosseland approximation) is used in many analytical and numerical models. Homsy and Walker [28] investigated the heat transfer in the neck-down region of a laser drawn optical fiber by using the optically thick approximation. Paek and Runk [48] proposed a one-dimensional numerical model with optically thick approximation to study the thermal transport in solid-core fiber drawing process. Lee, Roy Choudhury and Jaluria [35, 53] developed a two-dimensional numerical model to simulate the optical fiber drawing process. The optically thick method is also used for radiation in their model. In the model presented in the previous chapter, the optically thick method is applied to simulate the radiation in the hollow optical fiber drawing process. However, this approximation is valid only at the upper neck-down region where the glass media is thick. When the preform gets thinner or the preform is hollow, this approximation is not valid. A more accurate method is needed for the radiative transport. The P1 method was used by Kaminski [32] to compute the radiation transfer in the upper neck-down region. A two-band model for absorption coefficient of silica glass was first proposed by Myers [45]. Yin and Jaluria [69] presented the zonal method to investigate the optical fiber drawing process. Results show that the zonal method is more accurate in the lower neck-down region than the optically thick method. Recently, Chen and Jaluria [7, 8] used the zonal method to analyze the drawing process of a two-layer, cladding-core, optical fiber. Wei et al [63] investigated

the spectral radiative transfer and the transient temperature field in a semitransparent glass rod by using the discrete ordinates method.

In this present work, the zonal method is applied to model the radiative transport in the hollow optical fiber drawing process. The results obtained by using the zonal method and the optically thick method are compared. The effects of buoyancy and variable properties for air on the simulation of silica hollow fiber drawing process are also investigated. Finally, the effects of drawing parameters on collapse ratio and draw tension are studied.

3.2 Analysis

3.2.1 Radiation heat transfer model

The zonal method is applied to model the radiative transport within glass. The assumptions made in the zonal method are the following:

(1) The furnace is considered to be a gray and diffuse surface, with an emissivity 0.75 [23]. The inner and outer surfaces of hollow fiber are modeled as diffuse spectral surfaces.

(2) Glass is assumed to be a semi-transparent and non-scattering participating medium with banded absorption coefficients. Myers' two-band model [45] is applied, which is expressed as:

$$\begin{aligned} a &= 4.0cm^{-1}, \text{ for } 3.0\mu m \leq \lambda < 4.8\mu m \\ a &= 150.0cm^{-1}, \text{ for } 4.8\mu m \leq \lambda < 8.0\mu m \end{aligned} \tag{3.1}$$

Due to the lack of optical properties of the glass, constant refractive index and hemispherical total transmissivities and reflectivities are applied in the model. The refractive index is assumed constant 1.42 [35]. The hemispherical total transmissivities and reflectivities are $\rho^{1,c} = \rho^{2,o} = 0.08$, $\tau^{1,c} = \tau^{2,o} = 0.92$, $\rho^{1,g} = \rho^{2,g} = 0.54$ and $\tau^{1,g} = \tau^{2,g} = 0.46$ [62].

(3) Top and bottom openings of purge gas and central cavity are approximated as black surfaces at ambient temperature. Top and bottom ends of hollow fiber are

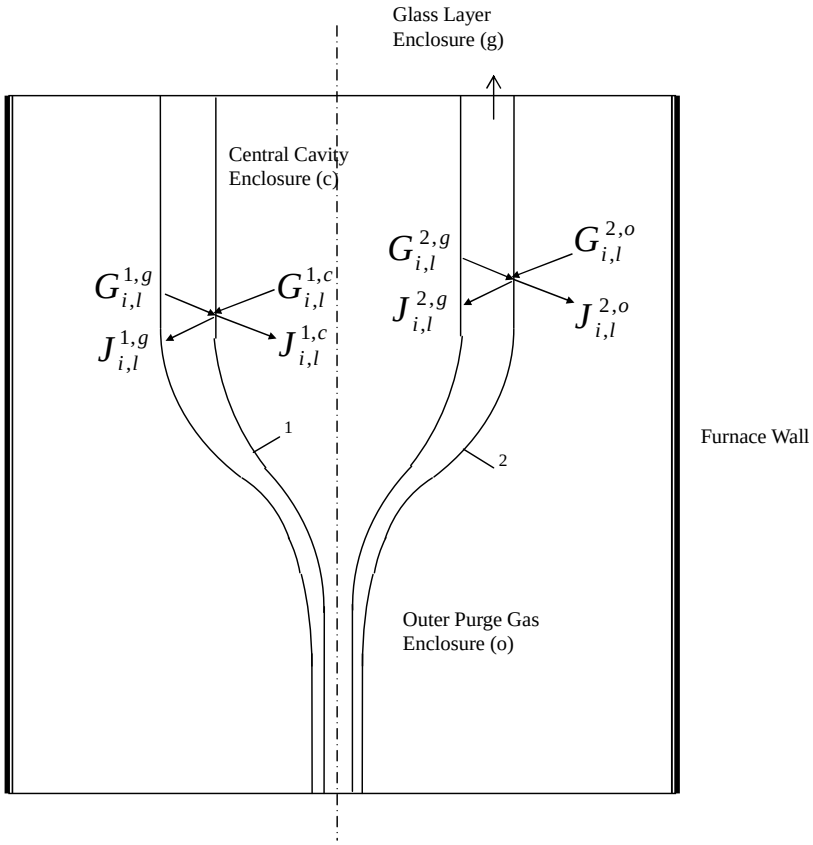

Figure 3.1: Schematic diagram for the zonal method

assumed to be black surfaces for simplification.

The discretization scheme used for the zonal method is similar to that of Yin [69]. The radiative source term can be obtained by considering three enclosures in the furnace shown in Figure 3.1. One is the outer purge gas enclosure composed of the furnace surface, the outer neck-down profile of hollow fiber and the top and bottom openings of purge gas. The other is the glass layer enclosure composed of the inner and outer neck-down profiles and the top and bottom ends of hollow fiber. The last one is the central cavity enclosure which consists of inner neck-down profile and top and bottom openings

of the central cavity. Superscript o, g and c denote these three enclosures, respectively, in the radiative energy equations. Superscript 1 denotes the interface between hollow fiber and the central cavity and the interface between hollow fiber and the purge gas is denoted with superscript 2. The subscript l denotes the l^{th} absorbing band. The radiative energy equations in the form of radiosity and irradiation for each absorption band are given below.

The irradiation equations for the surface zones on the central cavity and the outer purge gas enclosures are expressed as:

$$G_{i,\,l}^{<c,\,o>} = \sum_{j=1}^{N_{<c,\,o>}} F_{i-j} J_{j,\,l}^{<c,\,o>} \tag{3.2}$$

where $N_{<c,\,o>}$ is the total number of surface zones. F_{i-j} is the view factor between two discretized surface zones on the central cavity enclosure or the outer purge gas enclosure. The radiosity equation for zones at furnace surface and top and bottom openings of the central cavity and the purge gas is expressed as:

$$J_{i,\,l} = \epsilon_i \sigma T_i^4 f_{i,\,l} + (1 - \epsilon_i) G_{i,\,l} \tag{3.3}$$

The radiosity equations for the zones at surface 1 and 2 on the central cavity and the outer purge gas enclosures are

$$J_{i,\,l}^{1,\,c} = \rho^{1,\,c} G_{i,\,l}^{1,\,c} + \tau^{1,\,g} G_{i,\,l}^{1,\,g} \tag{3.4}$$

$$J_{i,\,l}^{2,\,o} = \rho^{2,\,o} G_{i,\,l}^{2,\,o} + \tau^{2,\,g} G_{i,\,l}^{2,\,g} \tag{3.5}$$

The irradiation equation for surface zones on the glass enclosure is:

$$G_{i,\,l}^{g} = \frac{1}{A_i} \left(\sum_{j=1}^{N_s^g} \overline{S_j S_i} J_{j,\,l}^{g} + \sum_{j=1}^{N_g^g} \overline{G_j S_i} n^2 \sigma T_j^4 f_{j,\,l} \right) \tag{3.6}$$

where N_s^g and N_g^g denotes the total number of the surface zones and volume zones in the glass enclosure respectively. $\overline{S_j S_i}$ is the direct exchange area between two discretized surface zones and $\overline{G_j S_i}$ is the direct exchange area between a discretized volume zone and a discretized surface zone. The radiosity equations for the zones at surface 1 and 2 in the glass enclosure are given as:

$$J_{i,\,l}^{1,\,g} = \rho^{1,\,g} G_{i,\,l}^{1,\,g} + \tau^{1,\,c} G_{i,\,l}^{1,\,c} \tag{3.7}$$

$$J_{i,l}^{2,g} = \rho^{2,g} G_{i,l}^{2,g} + \tau^{2,o} G_{i,l}^{2,o} \tag{3.8}$$

The radiosity equations for the zones at the top and bottom ends of hollow fiber are:

$$J_{i,l}^{g} = \epsilon_i \sigma T_i^4 f_{i,l} + (1-\epsilon_i) G_{i,l}^{g} \tag{3.9}$$

The irradiation and radiosity equations are solved by using Gauss-Seidel iteration with a convergence criteria of 10^{-5} . Then the radiative source term can be obtained.

$$S_{rk} = \frac{1}{V_k} \sum_{l=1}^{M} \left[\sum_{i=1}^{N_s^g} \overline{S_i G_k} \left(J_{i,l} - n^2 \sigma T_k^4 f_{k,l} \right) + \sum_{j=1(j\neq k)}^{N_g^g} \overline{G_j G_k} n^2 \sigma \left(T_j^4 f_{j,l} - T_k^4 f_{k,l} \right) \right] \tag{3.10}$$

where $\overline{G_j G_k}$ denotes the direct exchange area between two discretized volume zone.

In order to save computational time, a 30×5 coarse grid developed by Yin [68, 69] is used for radiation. But this coarse grid size is verified to be fine enough to produce grid-independent results. The calculations of $\overline{S_i S_j}$, $\overline{S_i G_j}$ and $\overline{G_i G_j}$ are described in Appendix C. The radiative source terms obtained from the coarse grid are interpolated into the finer grid by using a bi-linear interpolation algorithm. A parallel programming with the message-passing interface (MPI) is developed for the computation of the direct exchange areas. For the further details, see Chen and Jaluria [5, 7].

3.2.2 Numerical scheme

The grid and numerical scheme used in this chapter is the same as described in the last chapter. For any given neck-down profiles, the iterative procedure for the governing equations is carried out for about 2000 steps to save computational time. In this chapter, the preform feeding speed and the drawing speed are given. The outer diameter of the final fiber is determined by the numerical corrective procedure.

The drawing conditions for a typical drawing process are shown in Table 3.1. The glass properties taken from Fleming [20], which are shown in Appendix B, are functions of the temperature. The properties of the gas air are assumed to be constant at room temperature. The furnace temperature profile with cooling at two ends is shown in Figure 3.2. Pressurization of the gas in the core and the effects of buoyancy are neglected. The zonal method is applied to simulate the radiation heat transport in the

Table 3.1: Drawing parameters for a typical case in this chapter

Furnace Diameter	Furnace Length	Preform Inner Diameter	Preform Outer Diameter
7 cm	30 cm	2.5 cm	5 cm
Feeding Speed	Drawing Speed	Inlet Velocity of the purge gas	
3.75mm/min	10 m/s	0.1 m/s	

furnace. The profile correction scheme is applied to get the final converged neck-down profiles. The results in terms of streamlines and isotherms for this case are shown in Figure 3.3. The thicker black lines in Figure 3.3 present the two neck-down profiles. The values of the isotherms are the non-dimensional temperature with the softening temperature of silica glass 1900 K as the characteristic temperature. It is clear that the flow and temperature distributions in hollow fiber drawing are similar to those in solid-core fiber drawing. In the central cavity, air flows down and leaves at the bottom boundary due to the fiber viscous drag and the temperature distribution is determined by thermal diffusion.

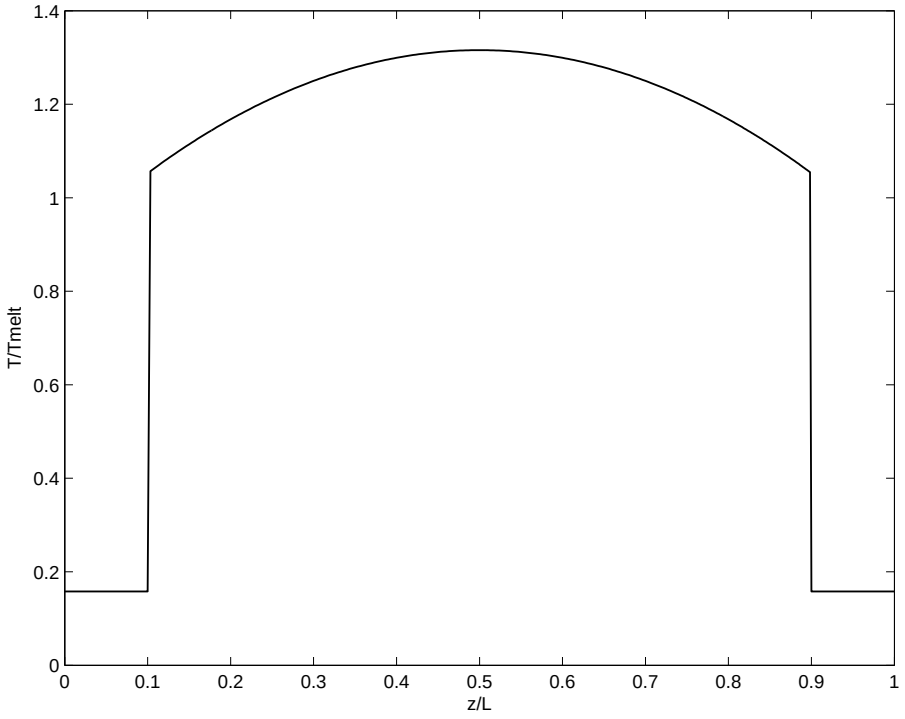

Figure 3.2: Furnace temperature profile

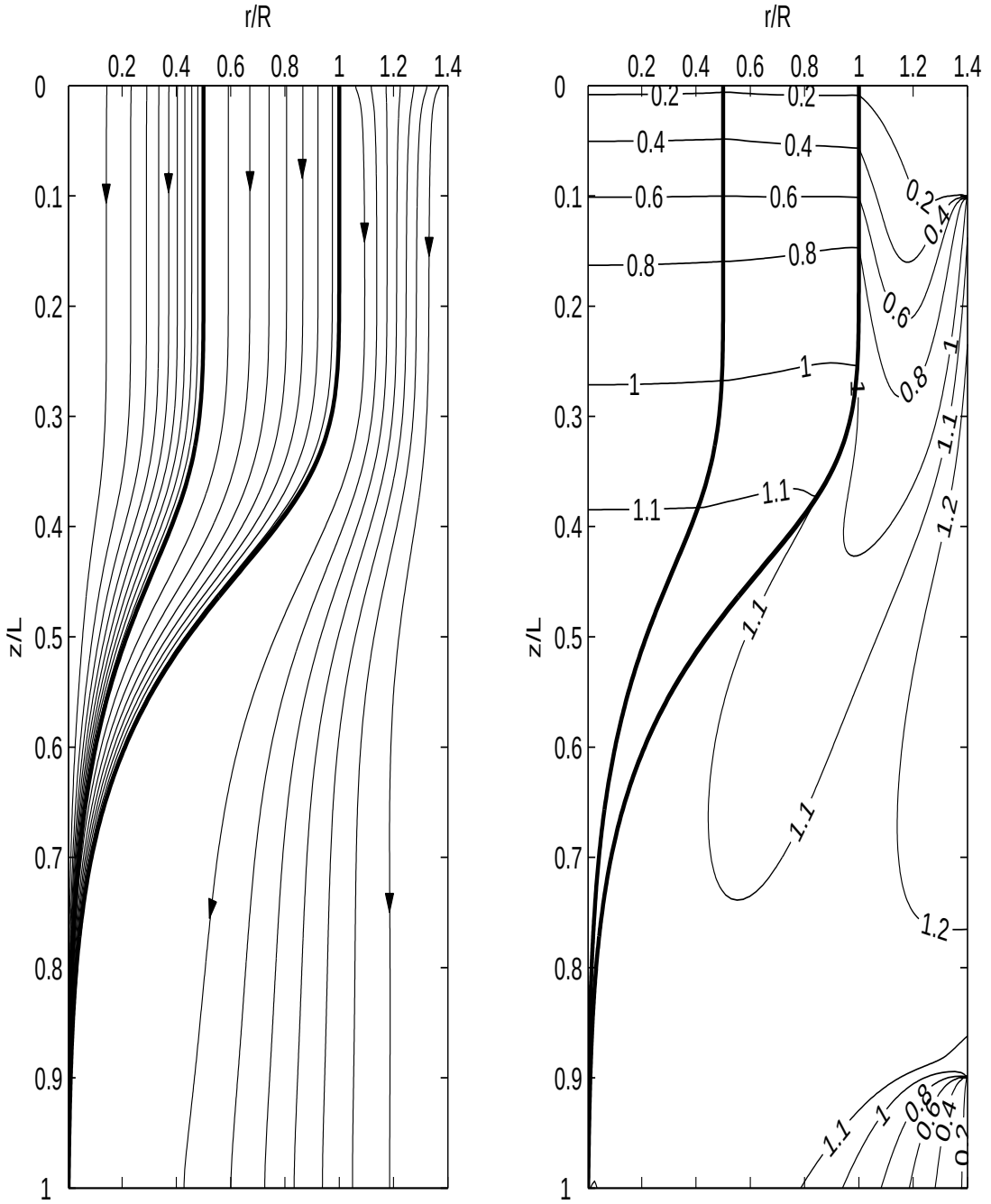

Figure 3.3: Streamlines and isotherms for a case with cooling at two ends distributed furnace temperature

3.3 Results and discussions

3.3.1 The effect of buoyancy and variable properties for air

The effects of temperature dependent properties of gas and buoyancy are investigated. The furnace temperature profile is assumed to be parabolic with a maximum value of 2500 K in the middle and a minimum 2000 K at both ends. Silica optical fiber is drawn over a large temperature range where the properties of air change substantially. In order to investigate the effects of variable properties and buoyancy, cases with constant properties, variable properties and buoyancy term included are compared. The variable properties for air can be computed using the state equation of an ideal gas and power law correlations [21], respectively, which are expressed as follows:

$$\frac{\rho}{\rho_{ref}} = \frac{T_{ref}}{T} \tag{3.11}$$

$$\frac{C}{C_{ref}} = \left(\frac{T}{T_{ref}}\right)^{0.104} \tag{3.12}$$

$$\frac{\mu}{\mu_{ref}} = \left(\frac{T}{T_{ref}}\right)^{0.65} \tag{3.13}$$

$$\frac{K}{K_{ref}} = \left(\frac{T}{T_{ref}}\right)^{0.79} \tag{3.14}$$

where $T_{ref} = 300$ K.

The Boussinesq approximations are used for the buoyancy effects. Figures 3.4 and 3.5 shows the contours of the streamline function and temperature for the case without and with the buoyancy effects, respectively. It is clear that streamlines in the central cavity in Figures 3.5 are quite different from those in Figures 3.4. In Figure 3.4, at the top boundary all the gas is driven down by the moving fiber due to the fiber viscous force. In Figure 3.5, only one part of gas is driven down by the moving fiber. The other part of gas flows up due to the buoyancy effects. However, the thermal field in the central cavity in Figure 3.5 is almost similar to that without buoyancy effects being included. Conduction is still the dominating heat transfer method compared with free convection in the central cavity. In the purge gas region, the contours of the

streamline function and temperature are almost the same for the case with and without the buoyancy effects.

The geometry and the quality of the hollow optical fiber depend on the neck-down profiles and the temperature distribution along the fiber. Hence, in order to investigate the effect of variable properties for gas and buoyancy, it is important to compare the two neck-down profiles and the temperature distributions along the fiber. Figure 3.6 and Figure 3.7 show the temperature distributions along the outside preform and neck down profiles for these three cases. The results from these three cases are very close. It is seen that the effects of variable properties for gas and buoyancy can be neglected when the hollow optical fiber drawing process is simulated to predict the geometry and quality of hollow optical fiber.

3.3.2 Validation

Comparison between the zonal method and the optically thick method is carried out. Unless otherwise mentioned, drawing parameters are the same as the typical case. The furnace temperature profile is assumed to be parabolic with a maximum value of 2500 K in the middle and a minimum 2000 K at both ends. The temperature distribution and heat flux along the outer surface obtained from these two methods are shown in Figure 3.8 and 3.9. The optically thick method assumes that all the radiation is absorbed at the surface and then reradiated as a diffusion process due to absorption over a very short optical distance [61]. So there is no radiation that is transmitted directly through the medium. But the zonal method allows it. This explains why the temperature at the outer surface obtained from the optically thick method is higher than that from the zonal method. The heat flux along the outer surface from the zonal method is higher than that from the optically thick method. This is due to the lower temperature distribution along the outer surface from the zonal method. The neck-down profiles obtained from these two methods, shown in Figure 3.10, are similar, but there are significant differences. The neck-down region of the profiles obtained from the optically thick method begins earlier than that from the zonal method, since the temperature at the outer surface computed from the optically thick method is slightly higher than that

from the zonal method, as seen in Figure 3.8. The zonal method is more accurate than the optically thick method, particularly in hollow fiber drawing because of the air core.

3.3.3 Thermal transport in the drawing furnace

The temperature distributions along the neck-down profiles are investigated. Figure 3.11 shows the temperature distributions along the furnace wall and the two neck-down profiles for a typical case. In the lower neck-down region the temperature is almost constant along the axis and there is essentially no temperature difference between the two neck-down profiles. This indicates that there is negligible temperature difference in either axial or radial direction in the lower neck-down region. In the upper neck-down region, the difference of temperature along these two neck-down profiles is relatively large. The temperature along the inner neck-down profile is lower than the temperature along the outer neck-down profile due to the thermal inertia. These temperature trends in the hollow optical fiber drawing process are the same as that in the solid-core fiber drawing process [53]. The maximum temperature difference in the radial direction is 161 K. It is noticed that the temperature difference mostly exists at the heating up region where the temperature of fiber is below the softening temperature.

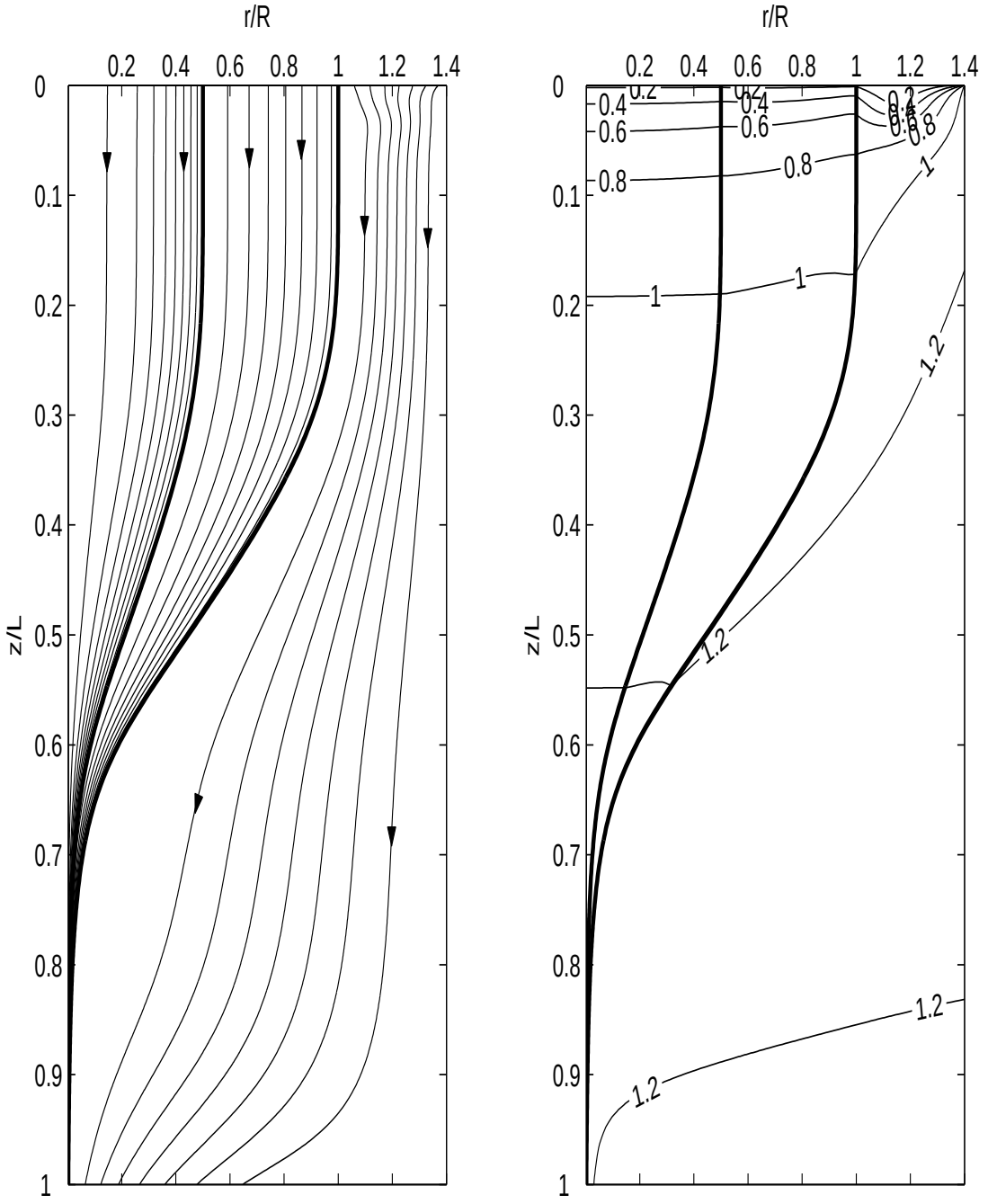

Figure 3.4: Streamlines and isotherms for a typical case with parabolic distributed furnace temperature without buoyancy effects

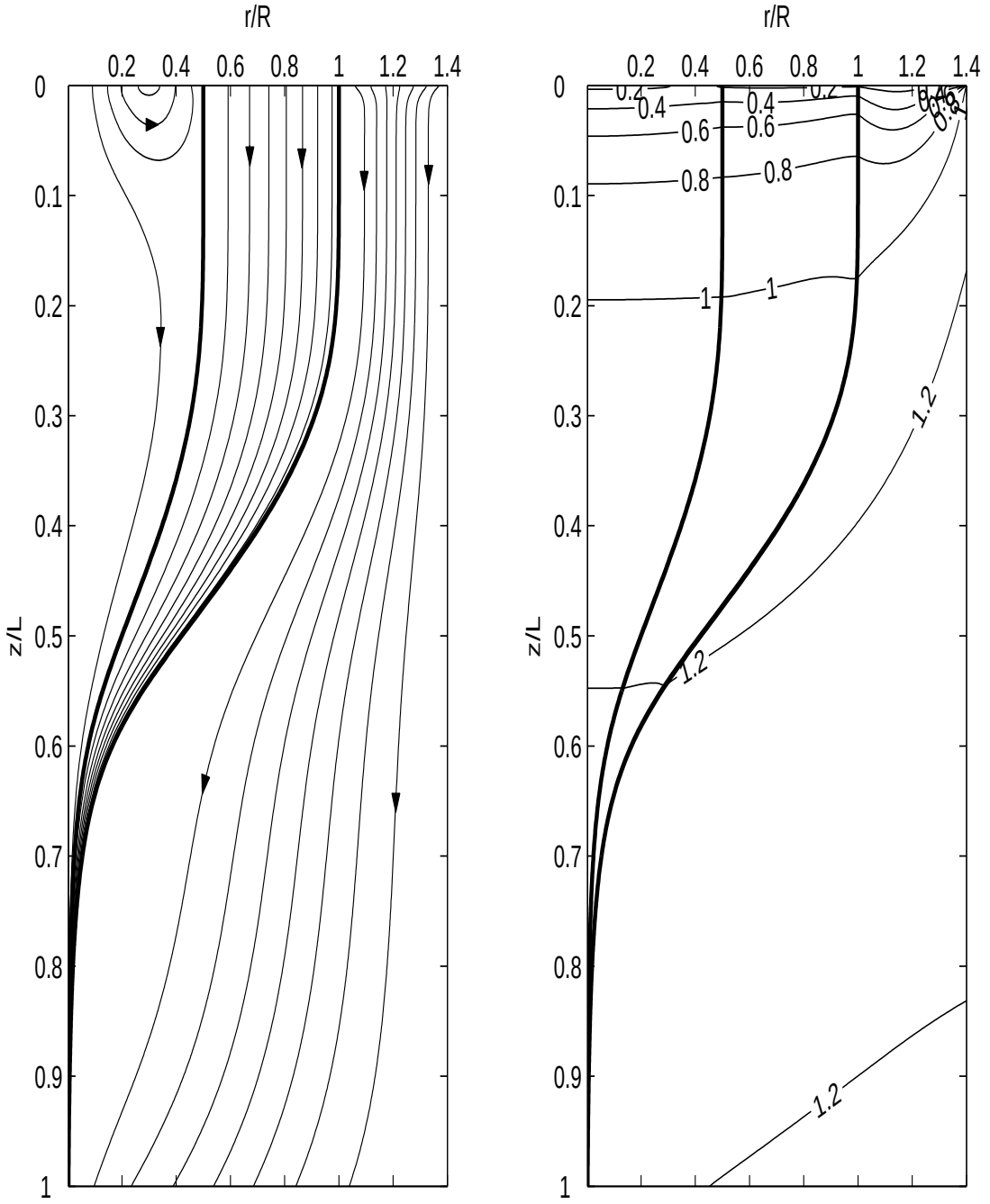

Figure 3.5: Streamlines and isotherms for a typical case with parabolic distributed furnace temperature with buoyancy effects

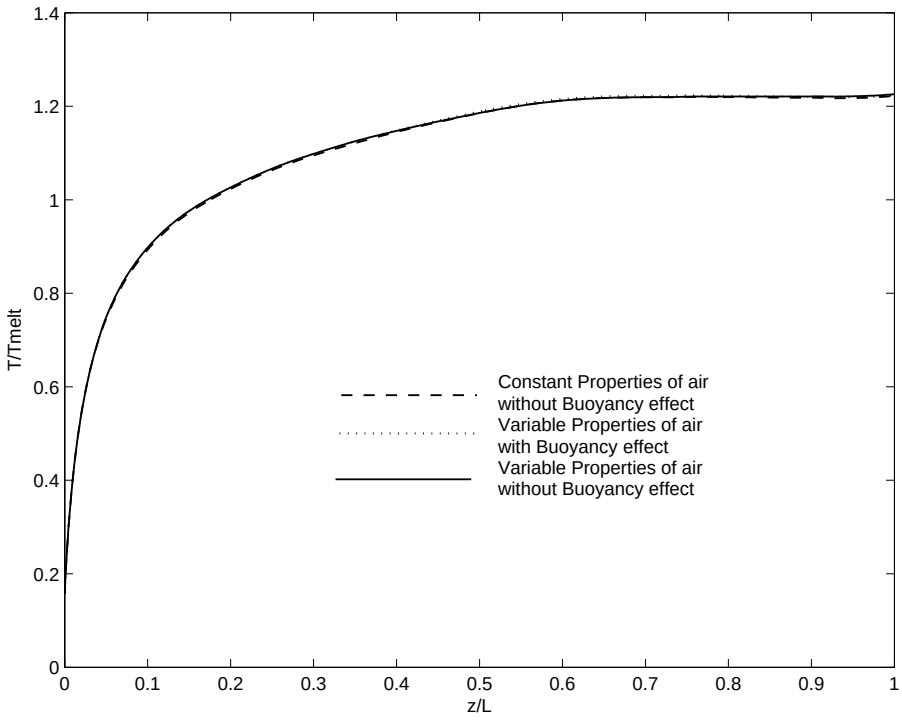

Figure 3.6: Temperature distributions along the axis for cases with constant properties, variable properties and buoyancy effects included

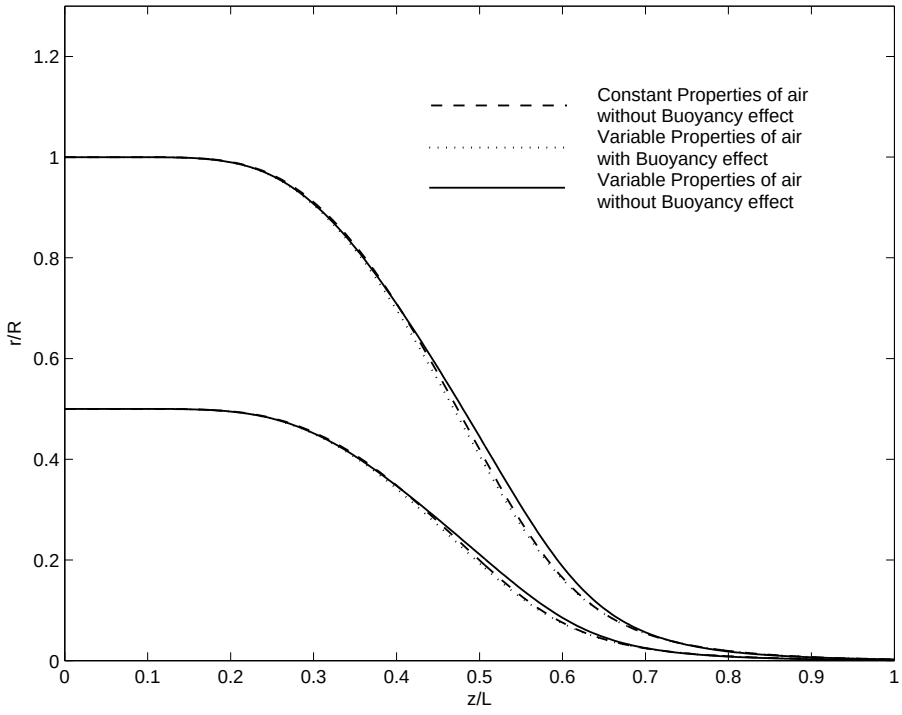

Figure 3.7: Neck-down profiles for cases with constant properties, variable properties and buoyancy effects included

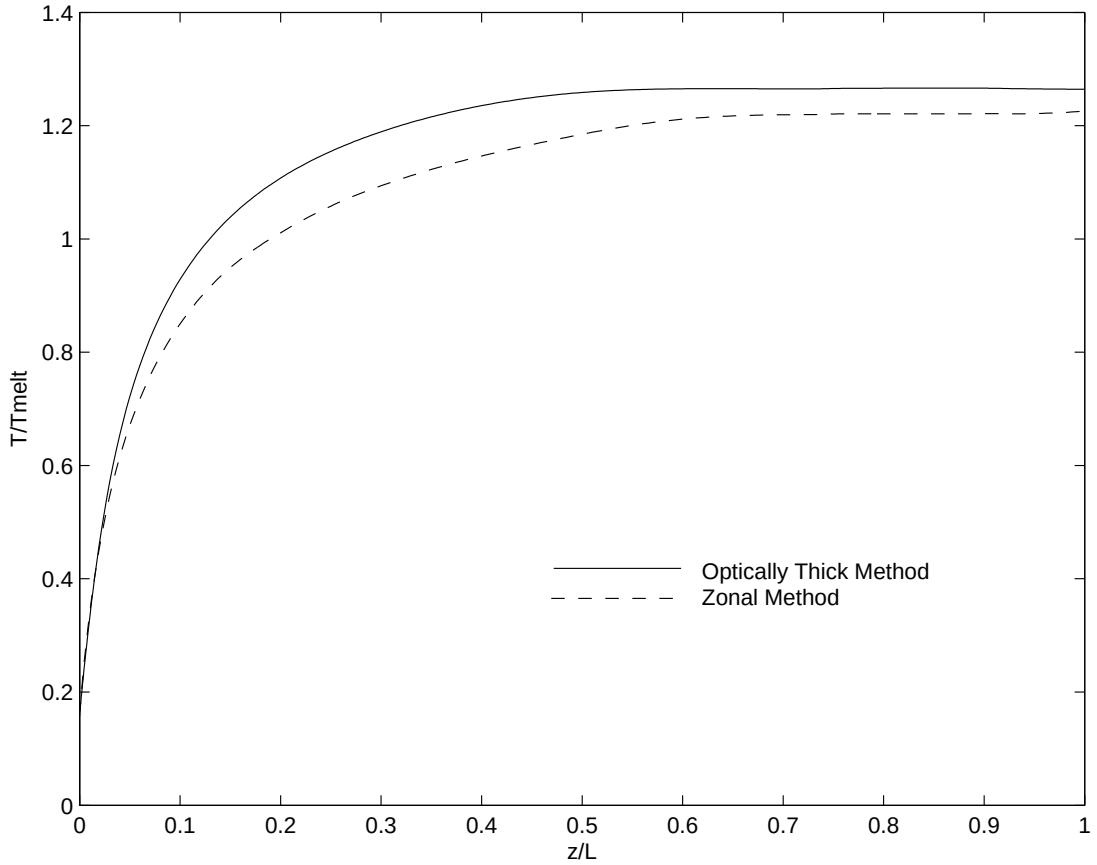

Figure 3.8: Temperature distributions at the outer surface computed by using the zonal method and the optically thick method

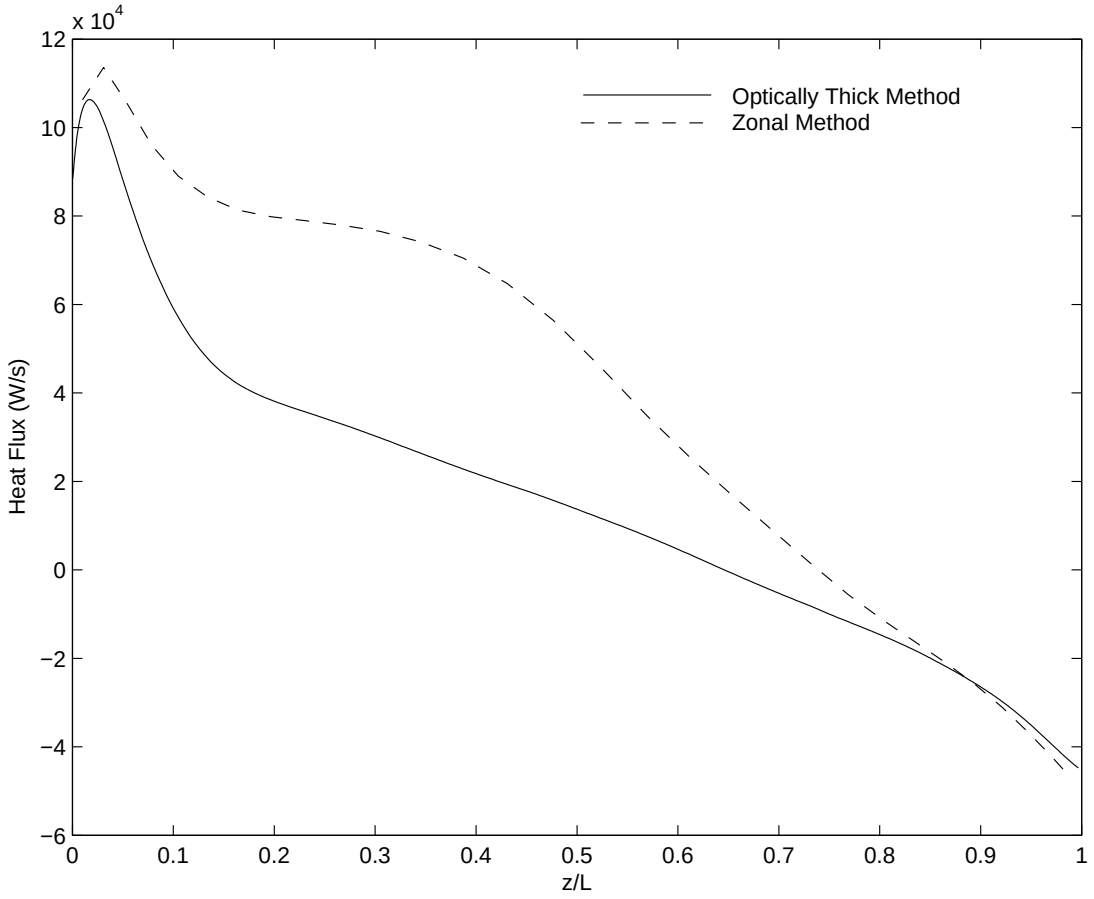

Figure 3.9: Heat flux along the outer surface computed by using the zonal method and the optically thick method

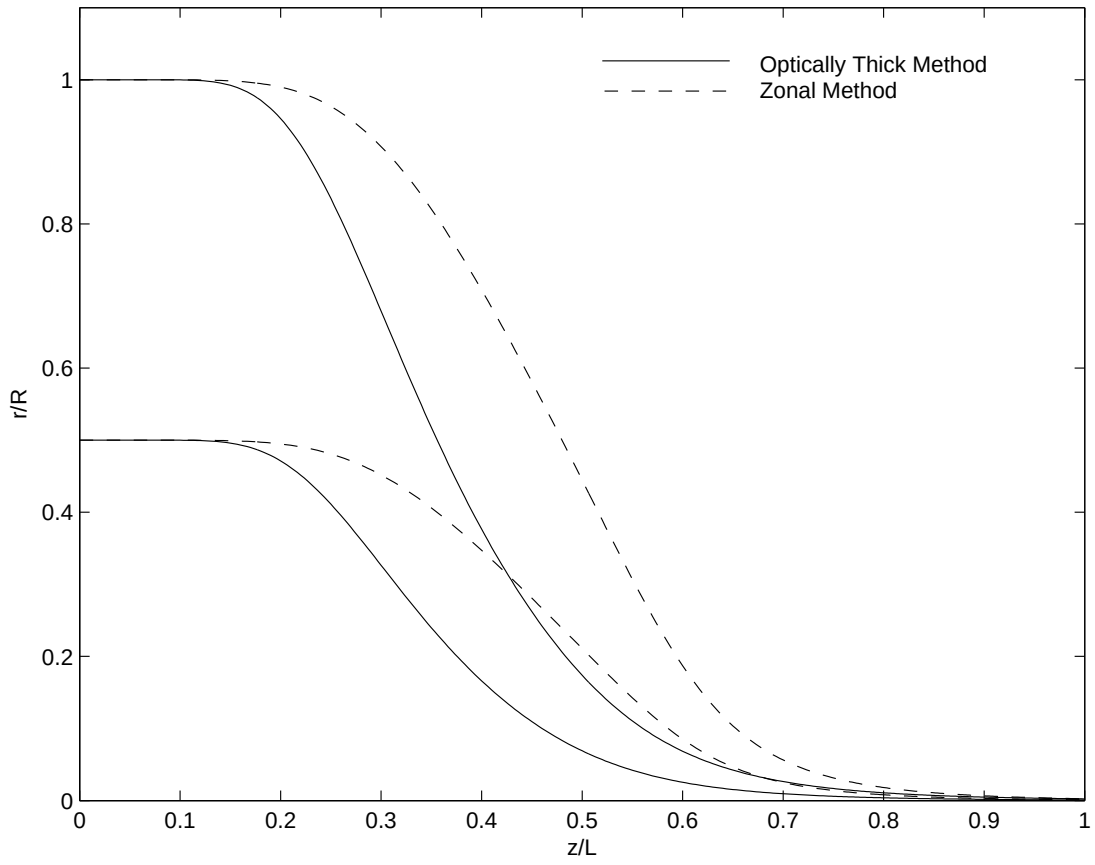

Figure 3.10: Neck-down profiles for hollow fiber drawing generated by using the zonal method and the optically thick method

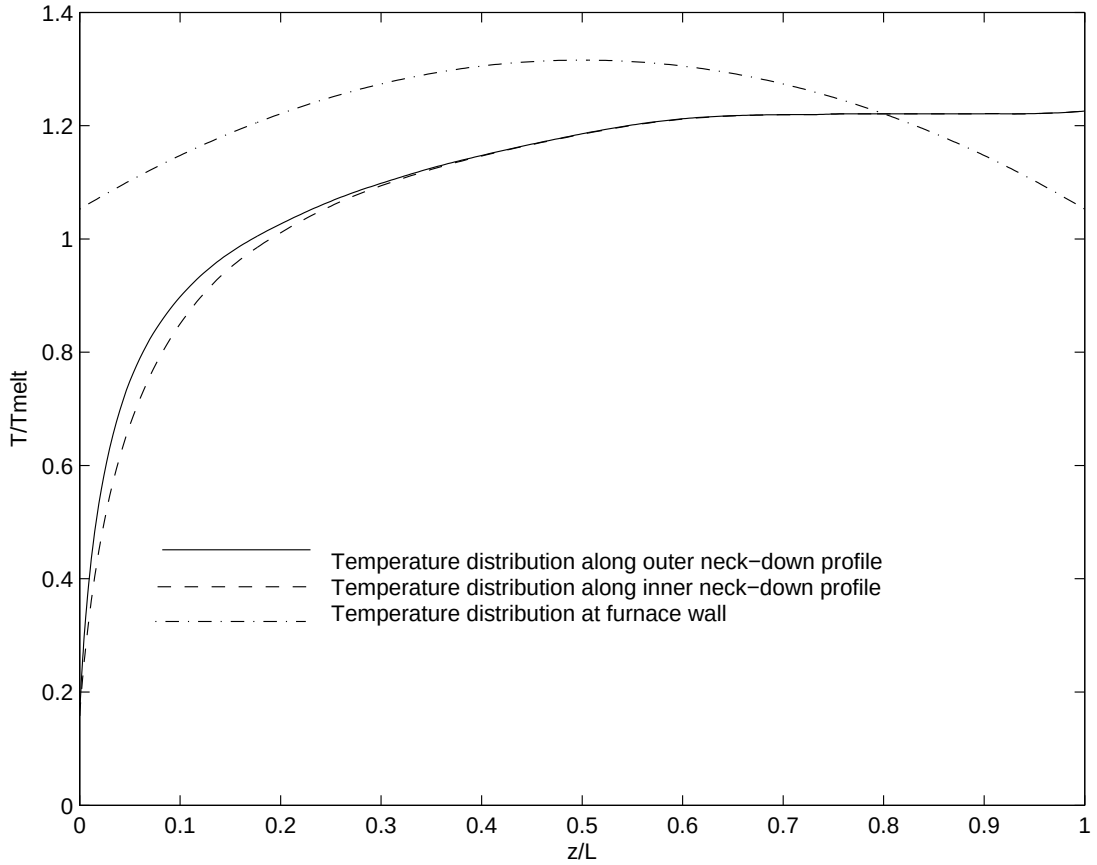

Figure 3.11: Temperature distributions along the furnace wall and the two neck-down profiles for a typical case

Drawing temperature

The temperature distribution on the furnace wall is a very important parameter in the drawing process. In order to investigate the effect of the shape of drawing temperature profiles, three different drawing temperature profiles shown in Figure 3.12 are compared here. The areas under these three profiles, which expressed as below, are equal.

$$A = \int_0^L T_w(z)dz \tag{3.15}$$

TP-I is the uniform distributed profile with the value of 2333.33 K. TP-II is the parabolic distributed profile with maximum 2450 K in the middle and minimum 2100 K in the two ends. TP-III is also the parabolic distributed profiles with maximum 2500 K in the middle and minimum 2000 K in the two ends. The differences between maximum and minimum temperatures of the drawing temperature for these three different profiles are 0 K, 350 K and 500 K, respectively. Figure 3.13 shows the temperature distributions along the surface of the preform/fiber. It is obvious that the preform is heated up to the softening point faster under the uniform distributed furnace temperature (TP-I). This is due to the higher temperature near the top entrance for TP-I. The final temperature of the fiber for TP-III is highest in these three different temperature profiles because the maximum temperature of TP-III is highest. So TP-III is most efficient to heat up the fiber in the drawing process.

Then three drawing temperature profiles with the same shape but different maximum values are compared. These three profiles, shown in Figure 3.14, have 500 K temperature difference between maximum and minimum. The temperature distributions along the surface of the preform/fiber for these three drawing temperature are shown in Figure 3.15. It is seen that the temperature of the fiber dramatically increases with an increase in the drawing temperature. This is expected since higher drawing temperature leads to higher heat flux. Therefore, both the shape and magnitude of the drawing temperature play an important role in the drawing process.

Preform feeding speed and drawing speed

The effect of the preform feeding speed on the temperature distribution along the surface of the preform/fiber is shown in Figure 3.16. The temperature of the preform/fiber increases with a decrease in the preform feeding speed. This is because the time spent by the preform/fiber in the furnace increases when the preform feeding speed decreases. Figure 3.17 shows the effect of the drawing speed on the temperature distribution along the surface of the preform/fiber. The temperature distributions along the surface of the preform/fiber are almost the same for different drawing speed. So the temperature distribution along the outer surface is quite insensitive to the drawing speed.

Radius ratio of preform

The effect of the geometry of the preform, indicated by the radius ratio of the preform, is studied. The radius ratio of the preform is also called the *initial radius ratio*. Figure 3.18 shows the temperature distributions along the surface of the preform/fiber for different values of the initial radius ratio. It is obvious that the temperature of the preform/fiber slightly increases with an increase in the initial radius ratio. This is because the preform with a higher radius ratio has a smaller thermal inertia due to the less mass.

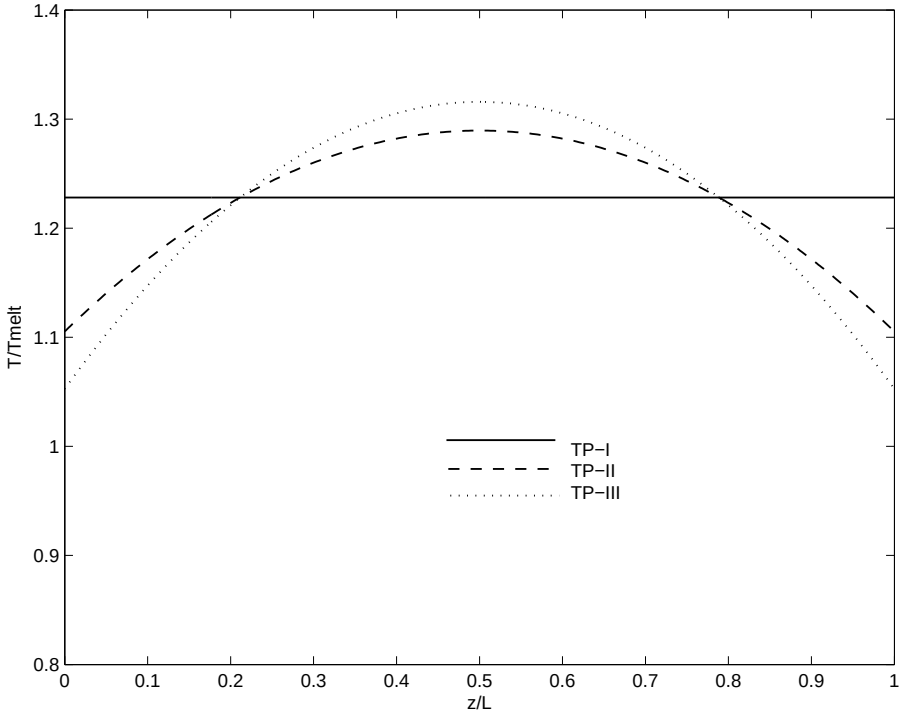

Figure 3.12: Three different temperature profiles on the furnace wall

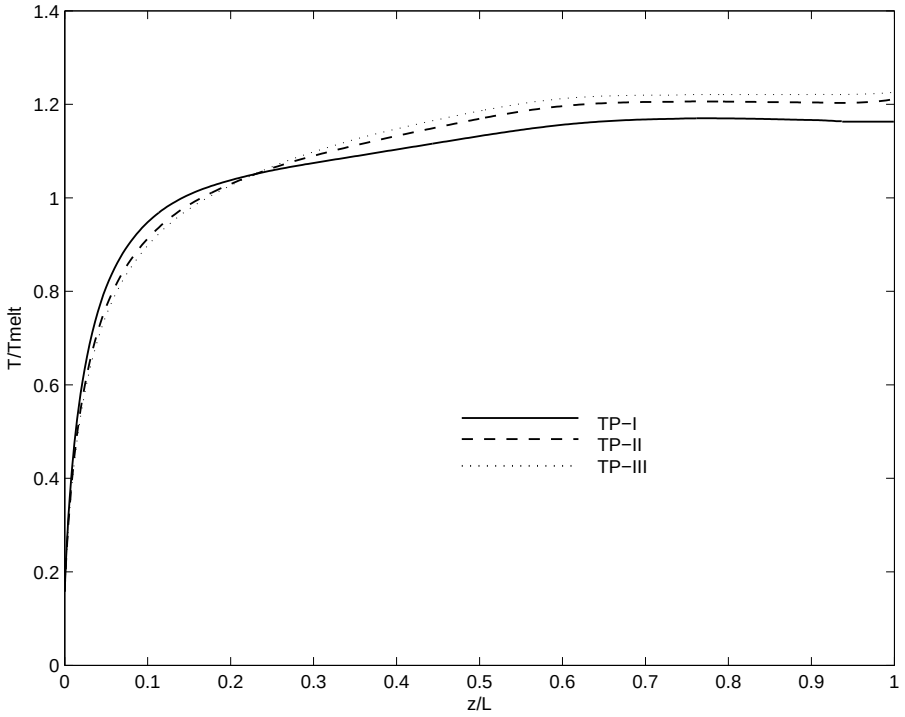

Figure 3.13: Temperature distributions along the outer surface of the fiber for different drawing temperature profiles

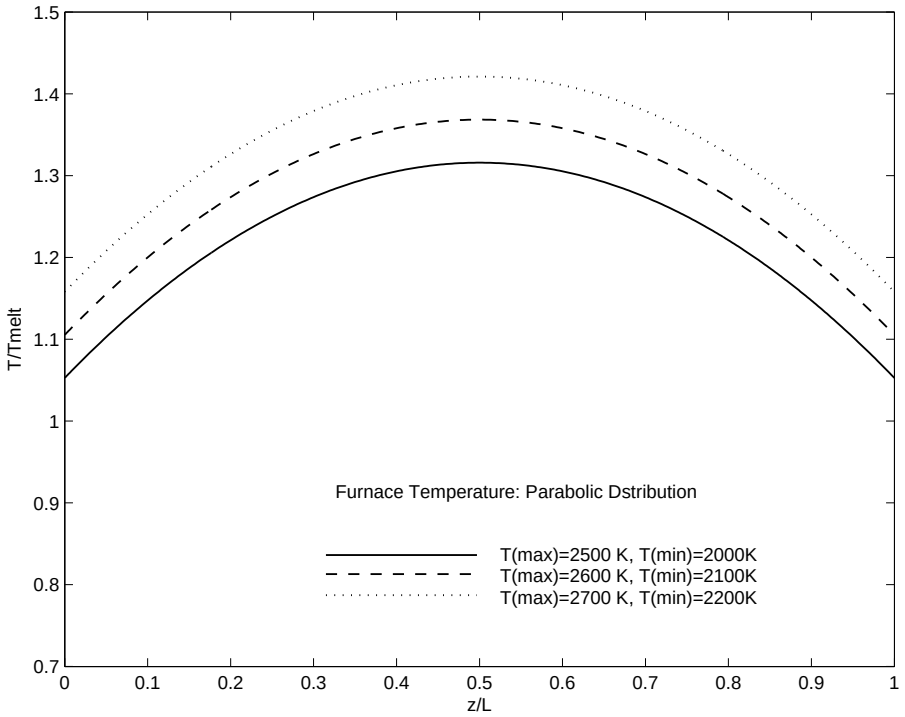

Figure 3.14: Three different drawing temperature distributions with the same shape but different magnitudes

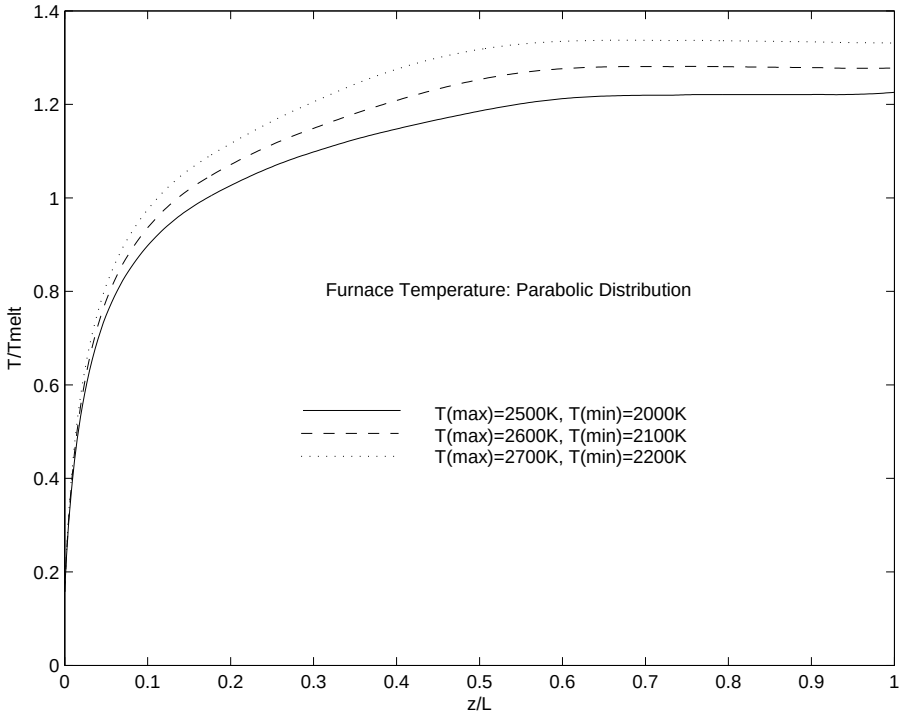

Figure 3.15: Temperature distributions along the outer surface of the fiber for different drawing temperatures

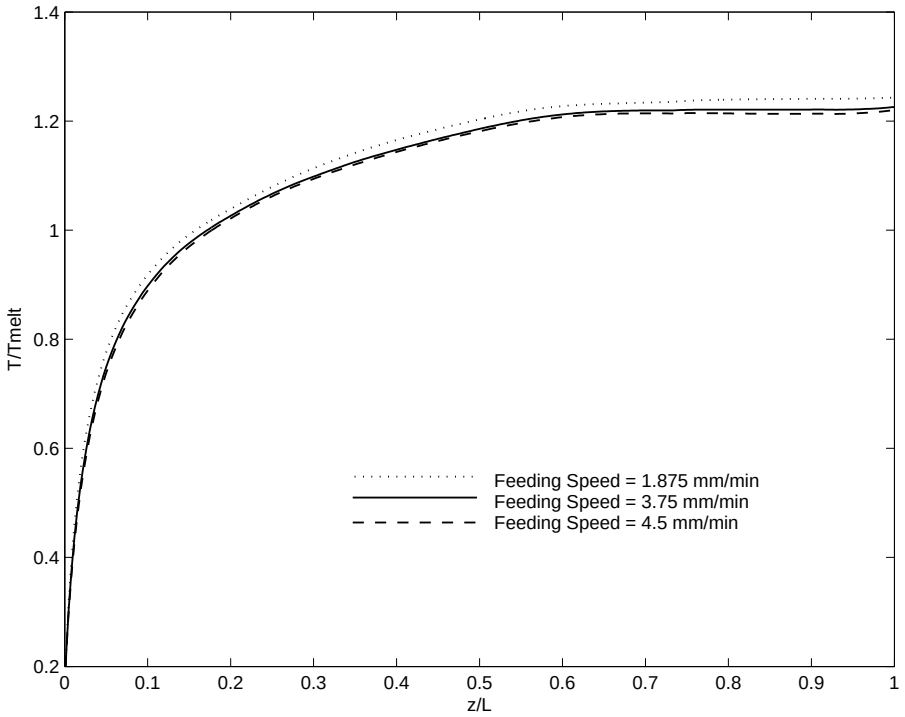

Figure 3.16: Temperature distributions along the outer surface of the fiber for different preform feeding speeds

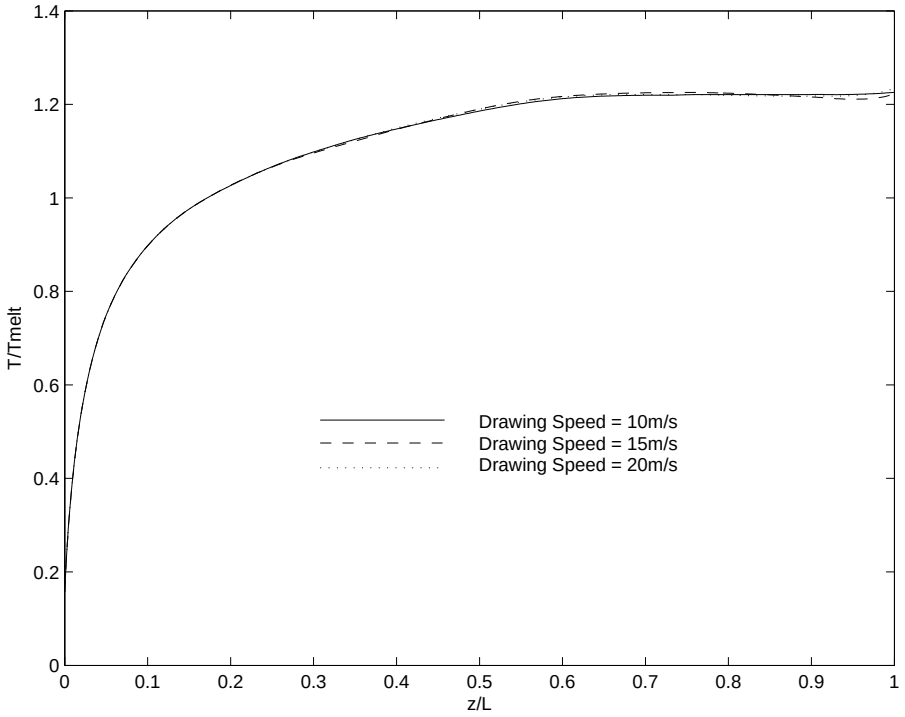

Figure 3.17: Temperature distributions along the outer surface of the fiber for different drawing speeds

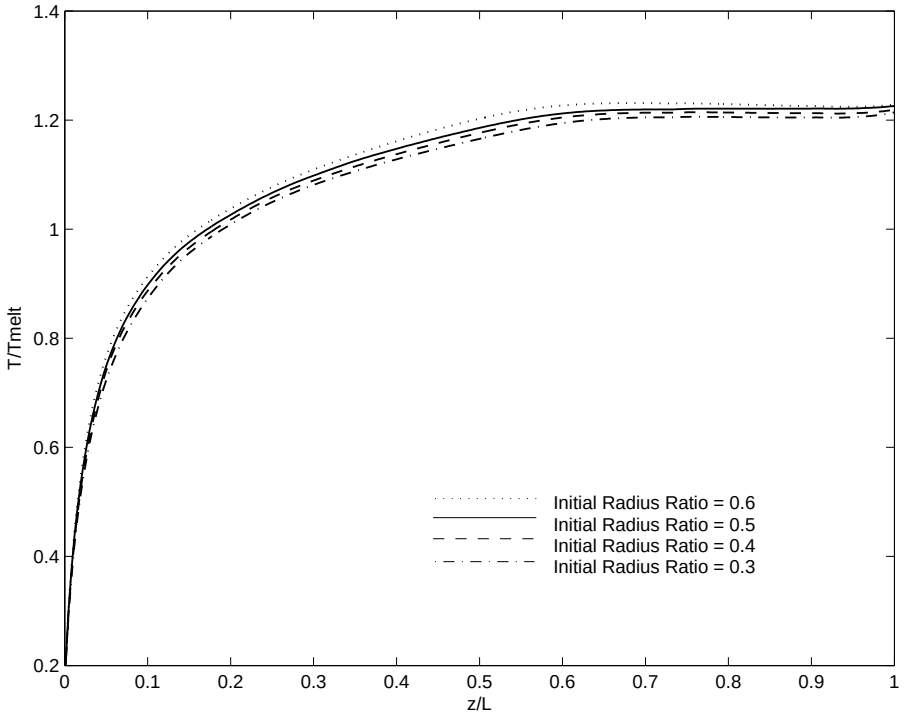

Figure 3.18: Temperature distributions along the outer surface of the fiber for different initial radius ratios

3.3.4 Neck-down profiles in hollow optical fiber drawing

Drawing temperature

The neck-down profiles strongly depend on the temperature of the preform/fiber in the furnace. The effect of the drawing temperature on the neck-down profiles is studied first. The neck-down profiles for TP-I, TP-II and TPIII are shown in Figure 3.19. The start point of necking occurs more upstream for TP-I. This is because the temperature of the fiber reaches the softening point faster for TP-I as shown before.

The neck-down profiles for different drawing temperature profiles, which have the same shape, are compared in Figure 3.20. It is clear that the neck-down profiles have significant changes for different drawing temperatures. The start point of necking occurs further upstream for higher drawing temperatures. This also can be explained by the higher temperatures in the preform/fiber for higher drawing temperatures.

Preform feeding speed and drawing speed

The effects of the preform feeding speed and the drawing speed on the neck-down profiles are shown in Figure 3.21 and 3.22, respectively. The neck-down profiles are very close for different drawing speeds. But the preform feeding speed is still a dominating factor in the neck-down profiles. It is seen that the necking starts earlier at lower preform feeding speed. These phenomena are due to the effects of the preform feeding speed and the drawing speed on the temperature of the preform/fiber in the furnace. As shown before, the temperatures of the preform/fiber are almost the same for different drawing speeds, but increase with a decrease in the preform feeding speed. Higher temperatures of the preform/fiber can lead to earlier start point of necking.

Radius ratio of preform

Figure 3.23 shows the neck-down profiles for different initial radius ratios. The necking of the outer neck-down profile starts further downstream for smaller initial radius ratio. This trend is in agreement with that obtained earlier from optically thick method. The reason is that the temperature of the preform/fiber in the furnace decreases with a decrease in the initial radius ratio. In conclusion, the neck-down profiles are strongly dependent on the temperature history of the preform/fiber.

3.3.5 Collapse in hollow optical fiber drawing

Effect of the pressure difference between the purge gas and the central cavity

Equation (2.27) indicates that the collapse ratio depends on the pressure difference between the purge gas and the central cavity ($\Delta p = p_a - p_c$). Here the effect of the pressure difference on the collapse ratio is investigated first. The variations of the collapse ratio along the axis with different pressure differences are shown in Figure 3.24. The black thicker line represents the case without pressure difference. It is seen that the collapse ratio of the final fiber decreases with a decrease in the pressure difference. This is because higher pressure in the central cavity has the effects to prevent collapse of the central cavity. This was also demonstrated by Fitt [19]. It is shown from Figure

3.24 that when $\Delta p = p_a - p_c = -50Pa$, the collapse ratio can be negative during the drawing process. This indicates that high negative pressure difference may cause the central cavity to enlarge during the drawing process. This is called "explosion" in the drawing process.

It is also seen in Figure 3.24 that the line with $\Delta p = 1Pa$ is very close to the line without pressure difference ($\Delta p = 0Pa$). This indicates that the effect of the pressure difference on the collapse ratio is neglectable when the magnitude of the pressure difference is less than one. The magnitude of the pressure difference between the purge gas and the central cavity for a typical case can be estimated as,

$$p_a - p_c \approx \circ(\rho U_a^2) = 0.01Pa \tag{3.16}$$

This order is so small that its effect on the collapse ratio can be neglected. So the assumption of neglecting pressurization of the gas in the core used before is reasonable.

Surface tension

It has been known that surface tension can lead to the collapse of the central cavity [19]. By plugging the equation (2.27) into equation (2.28), the collapse ratio can be expressed as:

$$C(z) = 1 - \frac{R_1(z)/R_2(z)}{R_{10}/R_{20}} = 1 - exp\left(\int_0^z \frac{-1}{\mu v}(\xi_1 H_1 + \xi_2 H_2)dz\right) \tag{3.17}$$

where the effect of pressure difference between the purge gas and the central cavity is neglected. The surface tension coefficient plays an important role in the collapse ratio. Equation (3.17) indicates that the collapse ratio equals zero, which means there is no collapse, when the surface tension coefficient equals zero. Figure 3.25 shows the variation of collapse ratio with surface tension coefficient. The collapse ratio increases almost linearly with an increase in the surface tension coefficient. A lower surface tension coefficient can reduce the distortion and collapse of the central cavity. This can also explain why the polymer PMMA (surface tension: 0.032 N/m) has an advantage over silica (surface tension: 0.3 N/m) in the preservation of the shape due to the relatively low surface tension.

Table 3.2: Collapse ratio for different drawing temperature profiles

Drawing temperature profiles	TP-I	TP-II	TP-III
Collapse Ratio	0.03	0.08	0.12

Drawing parameters

Several drawing parameters are varied to study their effects on the geometry of the final hollow fiber.

The effects of different temperature distributions at the furnace wall on the collapse ratio of the final fiber are investigated. Three different drawing temperature profiles TP-I, TP-II and TP-III shown in Figure 3.12 are compared. Table 3.2 gives the final collapse ratio for TP-I, TP-II and TP-III. There exist significant differences. The collapse ratio for TP-III is three times that for TP-I. Therefore, the collapse ratio is strongly dependent on the temperature profile on the furnace wall. A more uniform temperature distribution on the furnace wall can decrease the final collapse ratio.

The effects of other drawing conditions on the collapse ratio is also investigated. The temperature distribution on the furnace wall is assumed to be a parabolic profile, with the maximum in the middle and minimum at the two ends. The difference between maximum and minimum temperatures is fixed at 500 K. The maximum temperature of the parabolic distribution is referred to as the drawing temperature. The default drawing temperature is 2500 K. The other parameters are the same as the typical case. Figure 3.26 shows the variation of the collapse ratio of the final hollow fiber with the drawing temperature for difference drawing speeds. It is seen that the collapse ratio increases with an increase in the drawing temperature and with a decrease in the drawing speed. The collapse ratio increases 5 times at a drawing speed of 10 m/s when the drawing temperature increases from 2500 K to 2700 K, but decreases only about 2% at a drawing temperature of 2500 K when the draw speed goes up from 10 m/s to 20 m/s. Therefore, the drawing temperature affects the collapse ratio very significantly while the influence of the drawing speed is quite small.

The effect of the feed speed on the collapse ratio are shown in Figure 3.27. The collapse ratio increases about 40% when the preform feeding speed decreases from 4.5

mm/min to 3.0 mm/min. So the collapse ratio is also sensitive to the preform feeding speed.

These changes in the collapse ratio can be explained by considering the time spent by the preform/fiber in the drawing furnace. The total time of preform/fiber in the furnace, which depends on the preform feeding speed and the drawing speed, is the sum of the time to heat the preform up and the time for the preform/fiber to deform. At the same preform feeding and drawing speeds, the total time of preform/fiber in the furnace is almost constant. The time to heat the preform is shorter at higher furnace temperatures, which implies that the time for collapse increases. Therefore, the collapse ratio increases at a higher furnace temperature. When the drawing speed or the preform feeding speed decreases, the total time of preform/fiber in the furnace will increase. The collapse ratio increases since the time to heat the preform is nearly the same for different drawing speeds or preform feeding speeds at the same drawing temperature. Since the drawing speed is much greater than the preform feeding speed, the collapse time is more sensitive to the preform feeding speed than the drawing speed. So the collapse ratio is more sensitive to the preform feeding speed than the drawing speed.

The effect of the preform radius ratio on the collapse ratio is also investigated. Figure 3.28 shows the variation of the collapse ratio with the initial radius ratio. The collapse ratio changes very slightly with the initial radius ratio, indicating that the initial radius ratio is not an important factor in the final collapse ratio.

These results suggest that increasing the drawing speed or the preform feeding speed or decreasing the furnace temperature can avoid the central cavity from collapsing. Since the geometry of the final hollow fiber depends on the collapse ratio, the drawing temperature and the preform feeding speed, which are the dominating factors in the collapse of central cavity, can be used to control the geometry of the final hollow fiber.

3.3.6 Draw tension

Draw tension is crucial to fiber quality and process feasibility. Higher draw tension can lead to viscous rupture of the fiber. So the effects of the drawing parameters, i.e., the

drawing temperature, the preform feeding speed, the drawing speed and initial radius ratio, on the draw tension are investigated. Figure 3.29 shows the variation of the draw tension with the drawing temperature for different drawing speeds. The variation of the draw tension with the preform feeding speed is shown in Figure 3.30. It is clear that the draw tension increases with a decrease in the drawing temperature and an increase in the drawing speed and the preform feeding speed. These phenomena can be explained by the temperature of the fiber in the drawing furnace. Higher drawing furnace temperature, lower drawing speed or lower preform feeding speed can cause higher temperature of the fiber. Higher temperature of the fiber decreases the viscous force dramatically because glass viscosity decreases exponentially with an increase of temperature, as indicated by Equation (B.10) in Appendix B.

The effects of the drawing parameters on the draw tension are considered to obtain the sensitivity of the draw tension to these parameters. The draw tension increases about 20 times for 10 m/s drawing speed when the drawing temperature decreases less than 10% from 2750 K to 2500 K. A 50% increase of the drawing speed from 10 m/s to 15 m/s increases the draw tension by only about 15% at the 2500 K drawing temperature. A 50% increase of the preform feeding speed, from 3.0 mm/min to 4.5 mm/min, increases the draw tension by 60% at the 2500 K drawing temperature. So the drawing temperature is the most dominating factor in determining the draw tension. The draw tension is more sensitive to the preform feeding speed than the drawing speed. The sensitivities of the draw tension to the drawing temperature, the drawing speed and the preform feeding speed are the same as those of the collapse ratio.

The draw tensions with different preform radius ratio are shown in Figure 3.31. It is seen that the draw tension increase about 2 times when the preform radius ratio decreases from 0.6 to 0.3. This phenomenon is attributed to the variation of viscosity and the cross-sectional area of the fiber. It is known that the temperature of preform/fiber in the drawing furnace increases with an increase in the initial radius ratio. Higher temperature of the fiber will decrease the viscous force, which is dominating to the draw tension, due to the reduced viscosity. In addition, higher preform radius ratio means the smaller cross-sectional areas of the fiber. The smaller cross-sectional area

of the fiber leads to lower draw tension. Therefore, the preform radius ratio is another important factor in the draw tension, besides the drawing temperature and the preform feeding speed.

3.4 Summary

A numerical model, with the generation of the two neck-down profiles, has been presented for the hollow optical fiber drawing process in this chapter. The effects of variable properties of air and of buoyancy are investigated first. The results show that these effects can be neglected in the model. The radiative transport within glass is solved by the zonal method, which is more accurate than the optically thick method in hollow optical fiber drawing. A comparison between the zonal method and the optically thick method is carried out for validation.

The thermal transport and the neck-down profiles in hollow optical fiber drawing process are investigated. The neck-down profiles are strongly dependent on the temperature distribution along the preform/fiber in the furnace. Then the geometry and quality of the final hollow fiber, namely the collapse ratio and the draw tension, are studied in detail. The collapse ratio of the final hollow fiber increases when the drawing speed or the preform feeding speed decreases or the furnace temperature increases. So a faster drawing speed or preform feeding speed or lower furnace temperature can avoid the collapse of the central cavity. In addition, collapse of the central cavity can be effectively controlled by changing the pressure difference between the purge gas and the central cavity. The draw tension is dependent on the drawing parameters and the preform geometry. The numerical results show that a higher drawing speed, higher preform feeding speed, lower furnace temperature, or lower preform radius ratio can increase the draw tension. Through the study of sensitivity of drawing parameters, the drawing temperature and the preform feeding speed are found to be the most important factors in determining the geometry of the final hollow fiber and the draw tension. The preform radius ratio also plays an important role in the draw tension.

The model presented here can also be applied to simulate the drawing process

of hollow optical fibers made by other materials, such as polymers like polymethyl methacrylate (PMMA).

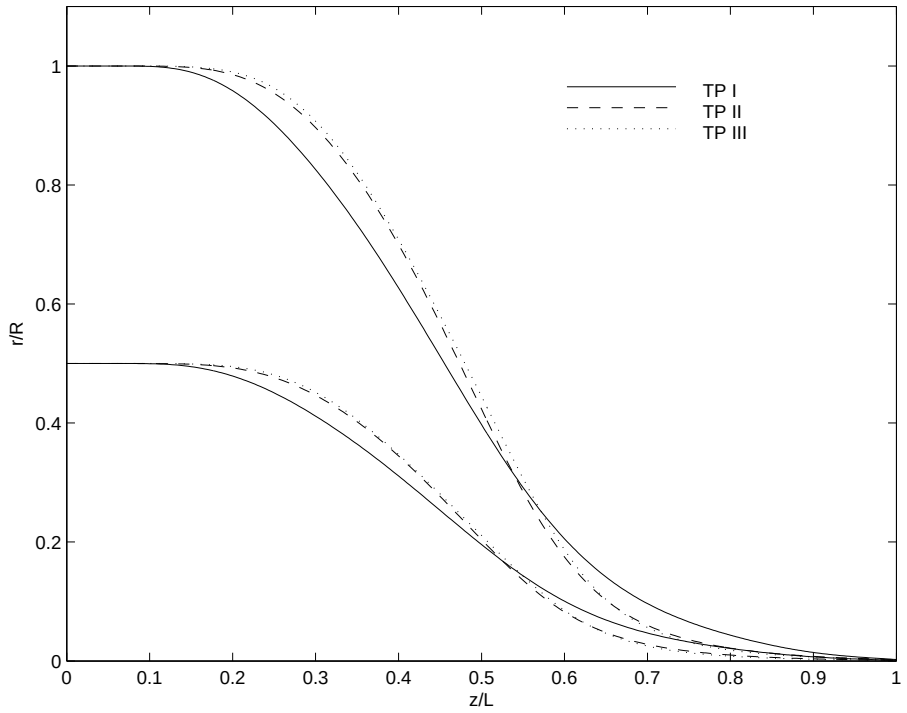

Figure 3.19: Neck-down profiles for different drawing temperature profiles

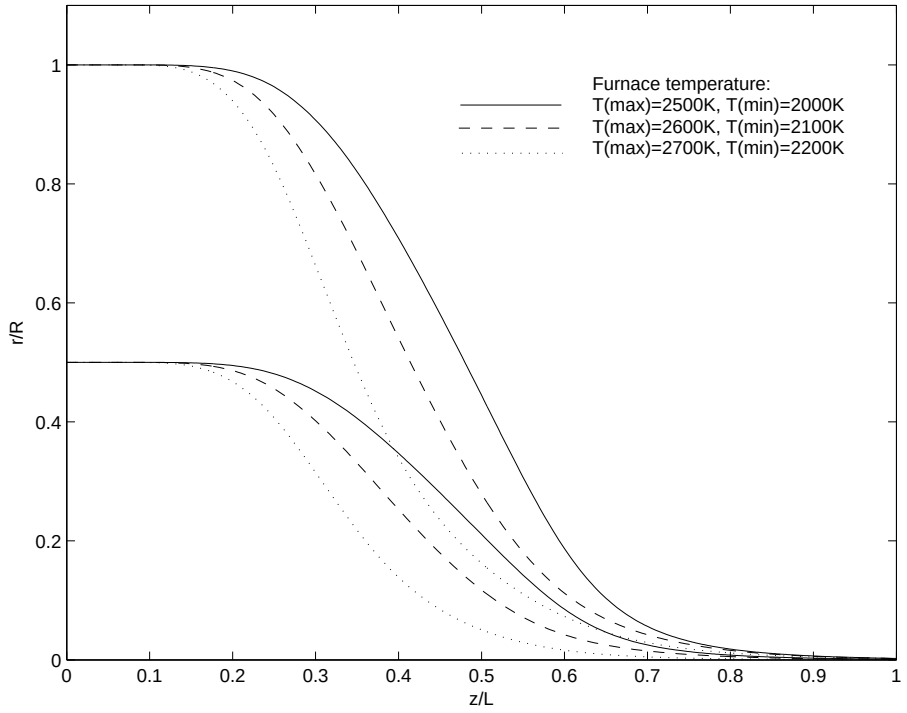

Figure 3.20: Neck-down profiles for different drawing temperatures

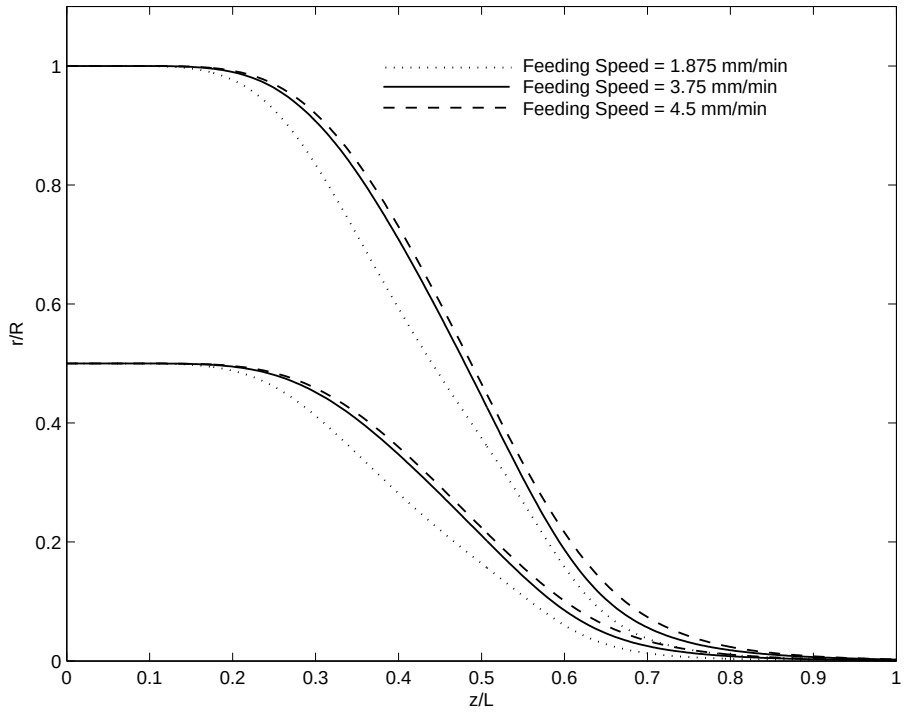

Figure 3.21: Neck-down profiles for different preform feeding speeds

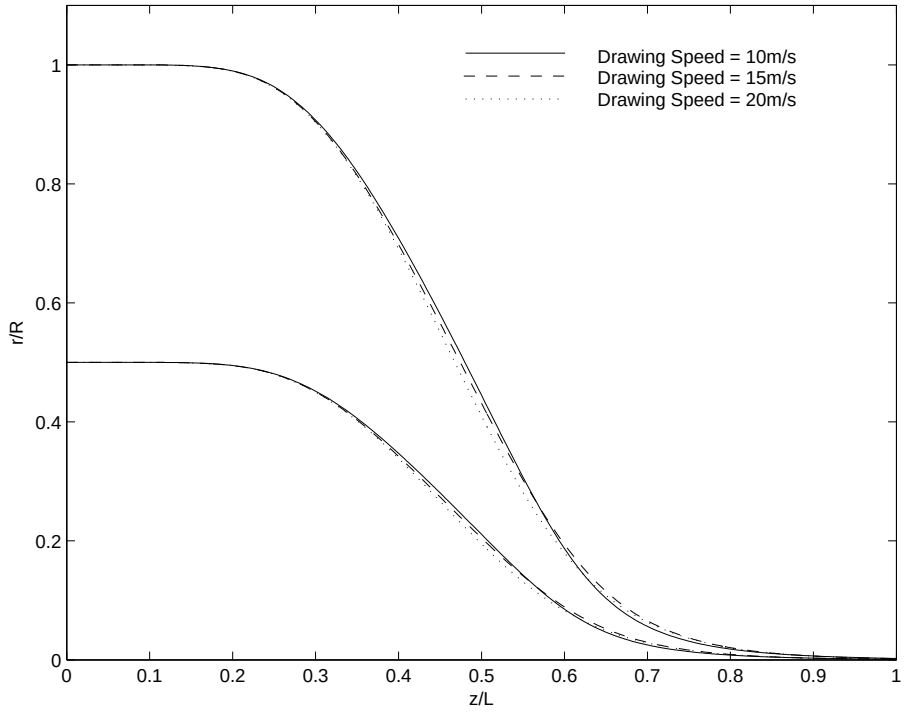

Figure 3.22: Neck-down profiles for different drawing speeds

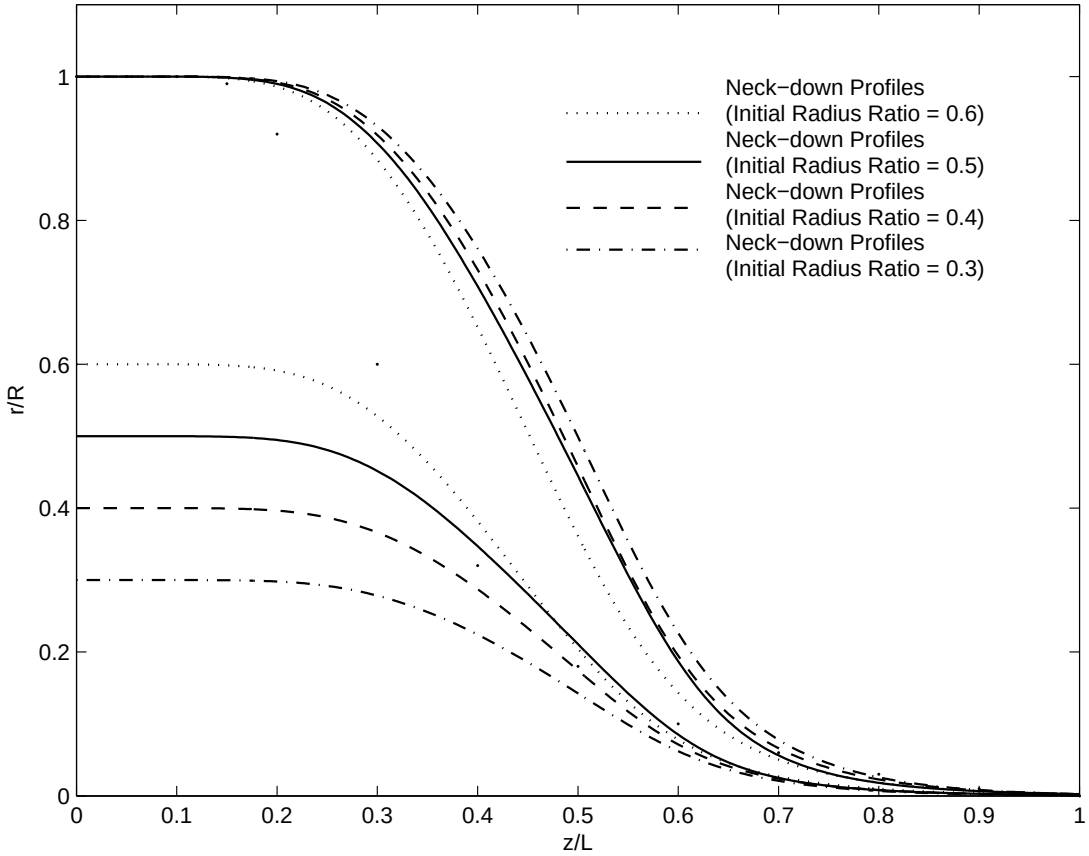

Figure 3.23: Neck-down profiles for different initial radius ratios

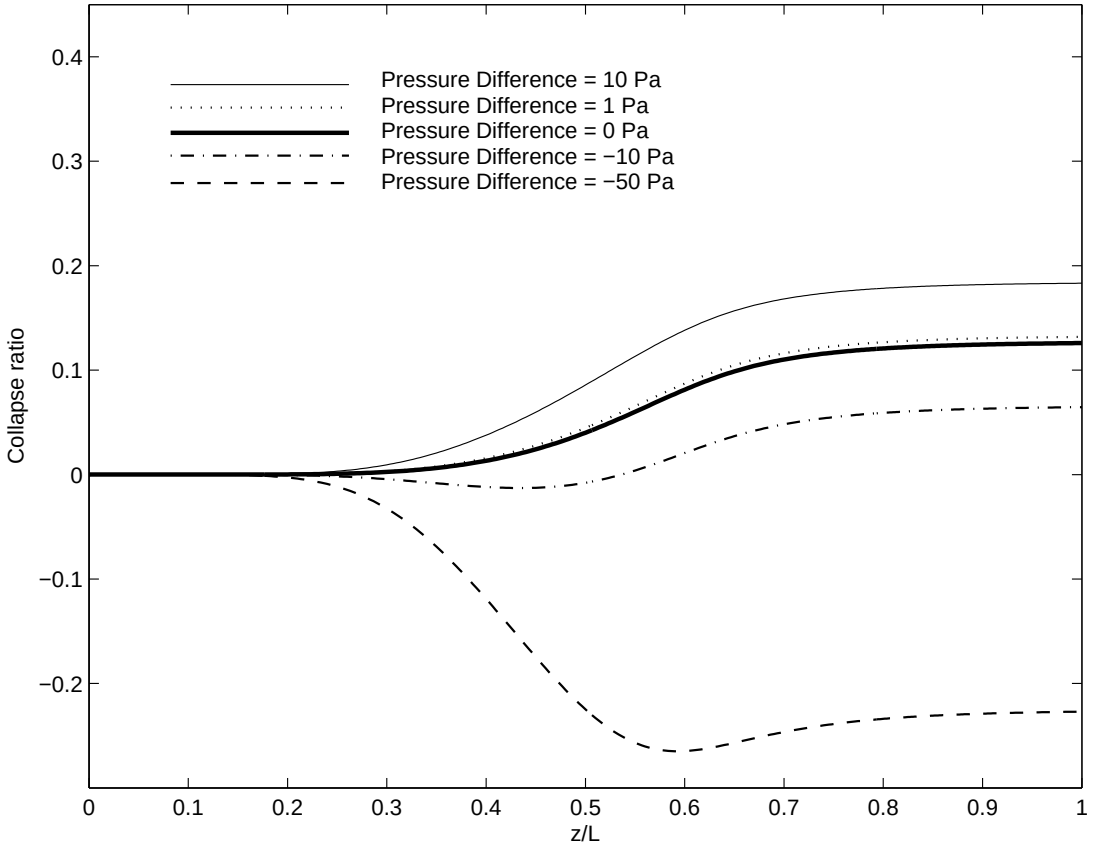

Figure 3.24: Variation of collapse ratio along the axis with different pressurizations in the core

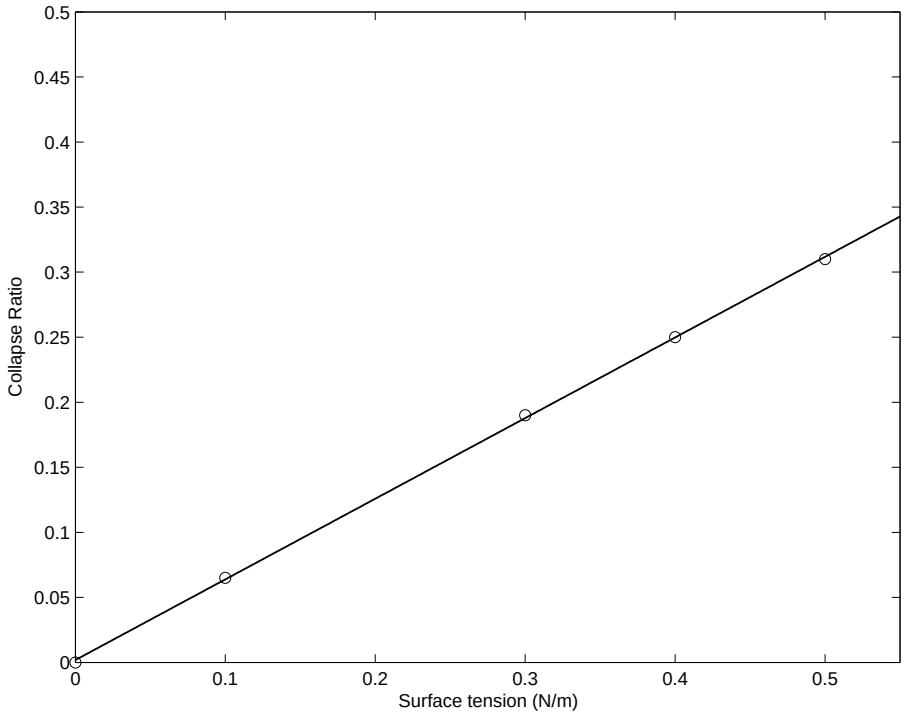

Figure 3.25: Variation of the collapse ratio with the surface tension

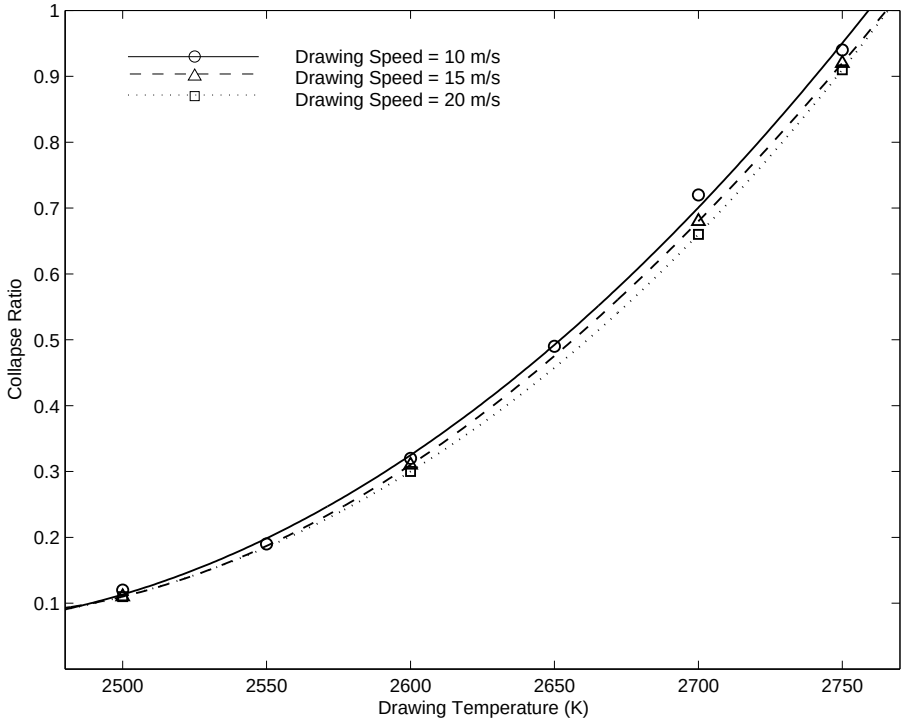

Figure 3.26: Variation of the collapse ratio with the drawing temperature for different drawing speeds

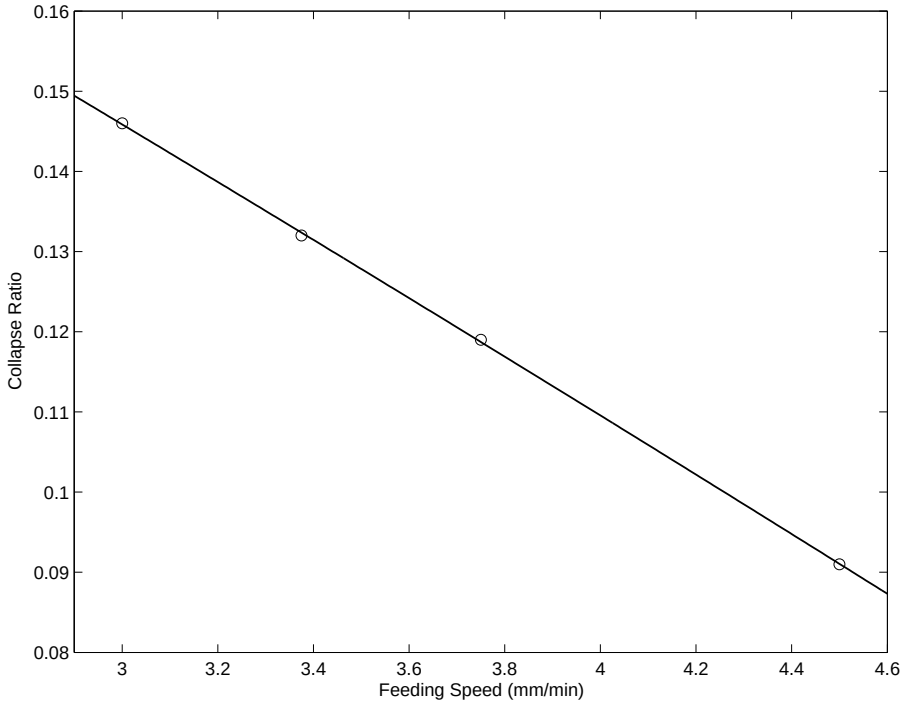

Figure 3.27: Variation of the collapse ratio with the preform feeding speed

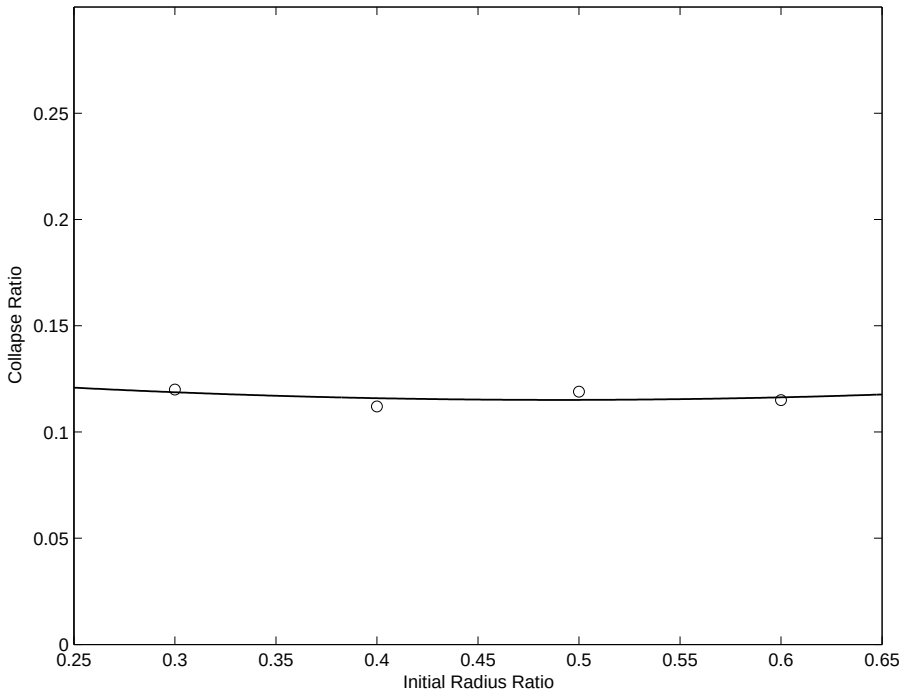

Figure 3.28: Variation of the collapse ratio with the initial preform radius ratio

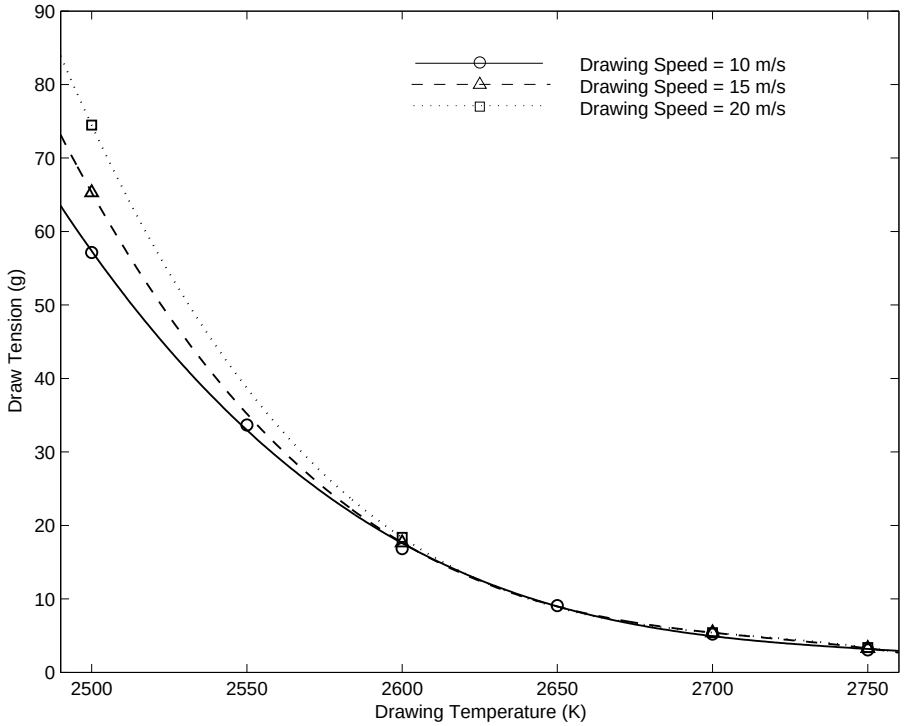

Figure 3.29: Variation of the draw tension with the drawing temperature for different drawing speeds

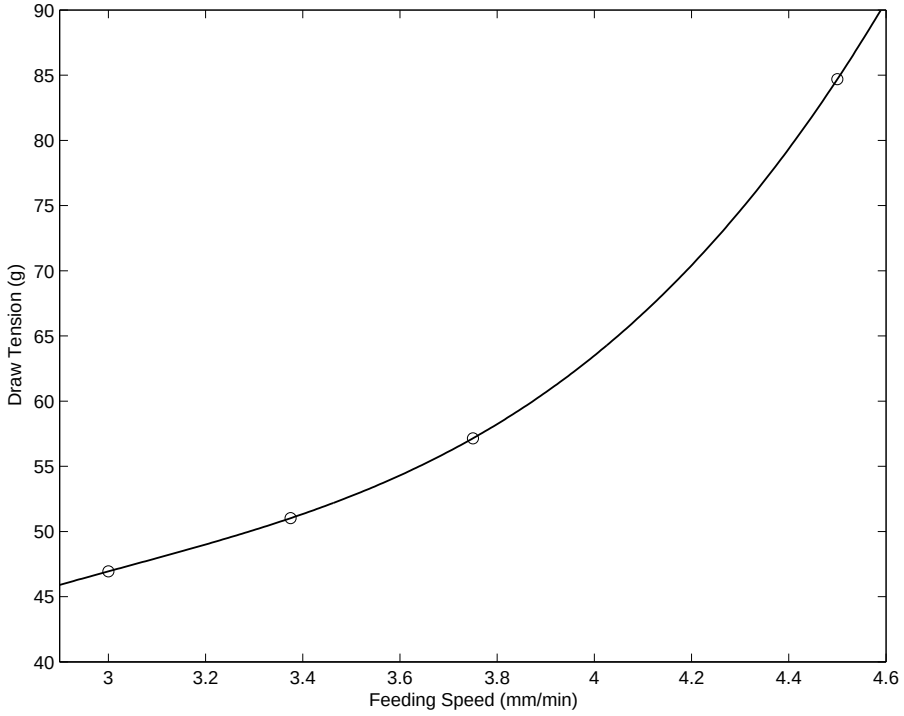

Figure 3.30: Variation of the draw tension with the preform feeding speed

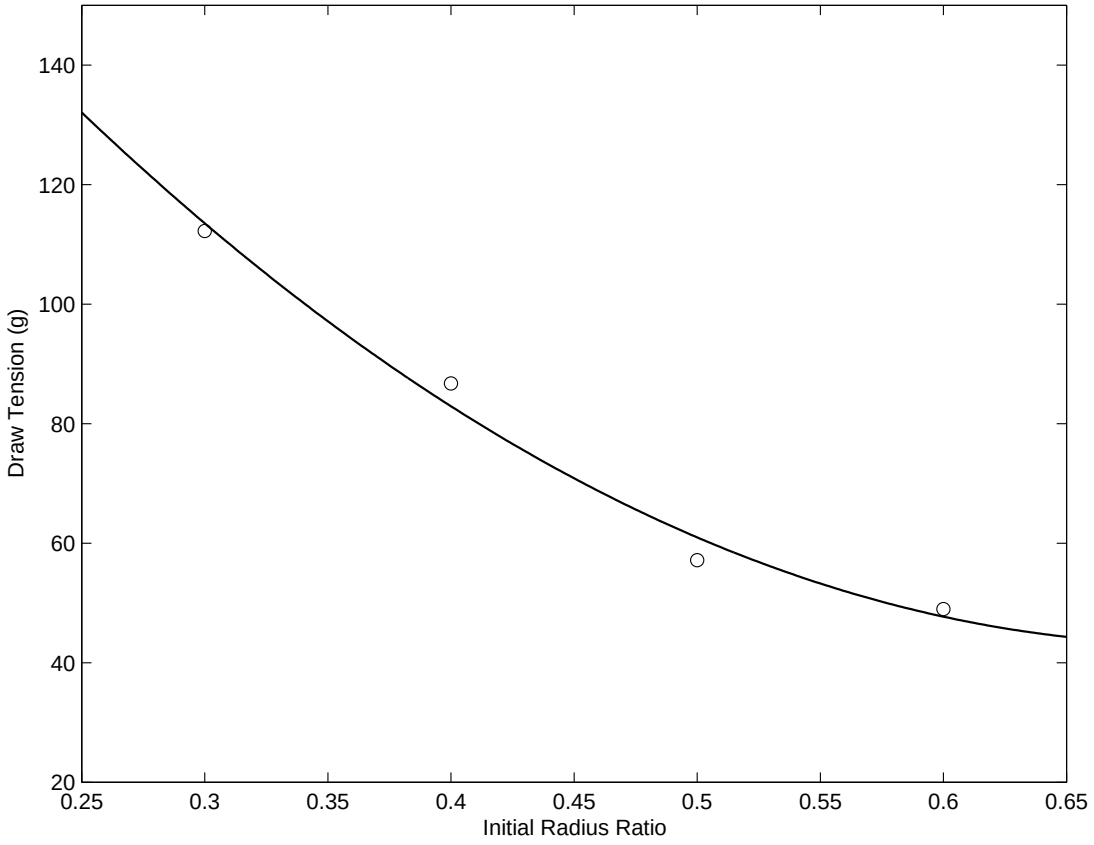

Figure 3.31: Variation of the draw tension with the preform radius ratio

Chapter 4

Optimization in Hollow Optical Fiber Drawing Process

4.1 Introduction

Hollow optical fibers have a wide range of application, from sensor technology to medical applications. A high quality hollow optical fiber is desirable to get lower signal loss. Hollow optical fibers are fabricated by drawing a hollow preform to the fiber diameter in a conventional fiber-drawing tower. The quality of the final hollow fiber can be characterized by many factors such as draw tension, radial non-uniformity in temperature and velocity, and concentration of drawing-induced defects. Small values of these factors are desirable from fiber quality considerations. All these factors strongly depend on the drawing conditions such as the furnace temperature, the drawing speed and the preform feeding speed. Therefore, optimizing the hollow fiber drawing system can significantly improve the quality of hollow optical fiber.

There are a number of studies on solid-core fiber drawing process. Among them only few are applied to the optimal design of the fiber drawing system. For instance, Cheng and Jaluria [12] developed an optimization algorithm. Compared with solid-core fiber drawing, very few researchers have presented the simulation of the hollow optical fiber drawing process [4, 18, 19, 59]. And no efforts on optimization of hollow optical fiber drawing process are available in the literature. However, optimization in hollow optical fiber drawing is strongly needed due to the interest in high quality fibers at high draw speeds. Compared to experimental work, numerical techniques are obviously more convenient and practical approach to optimization.

This chapter presents the optimal design of hollow optical fiber drawing process, considering the feasible domain. The numerical model of the hollow optical fiber drawing process, presented in the previous chapter, is used for optimal design. As shown

in the previous study, on the one hand hollow fiber may collapse completely in high furnace temperature or at low drawing speed. On the other hand, lower furnace temperature or high drawing speed may cause failure in the drawing process due to viscous rupture. Hence, the feasible domain for hollow fiber drawing, in which a successful fiber drawing is obtained, must be identified before the drawing system is optimized to get high quality hollow fibers. Among the drawing parameters, the furnace temperature and the preform feeding speed significantly affect the drawing process and can be easily and practicably controlled. So the drawing temperature and the preform feeding speed are chosen for investigation and optimized for hollow optical fiber drawing process. The effects on draw tension, maximum temperature and velocity lag and drawing-induced defect centers are investigated. Based on these results, an appropriate objective function for optimization is formulated and a multi-variable and non-constrained optimal design problem is presented. Finally, a simple optimization procedure is carried out to solve the problem.

4.2 Feasible domain for hollow optical fiber drawing

A typical drawing furnace with fixed dimensions is used here. The furnace diameter is 7 cm and its length is taken as 30 cm. The inner and outer diameters of the preform are taken as 2.5 cm and 5 cm, respectively. Unless otherwise mentioned, the velocity of the purge gas at the inlet is taken as 0.1 m/s. Pressurization of the gas in the core is neglected. The furnace temperature is assumed to be a parabolic profile, with the maximum in the middle and minimum at the two ends. The maximum temperature is referred to as the drawing temperature. The difference between maximum and minimum temperatures is fixed at 500 K. The temperature of the preform (T_0) is taken as 300 K. The fiber drawing speed and the preform feeding speed are taken as 10 m/s and 3.75mm/min, respectively.

The hollow fiber cannot be drawn at any arbitrary combination of critical drawing parameters, as shown in previous studies [67]. Figure 4.1 illustrates the feasible domain in terms of the drawing temperature and the drawing speed. The drawing speed is in the range of 1m/s to 20m/s. It shows that drawing process is possible only in the region

between two dashed lines. The left boundary exists because the continuous drawing process may fail due to the lack of material flow at low furnace temperature or high drawing speeds, which is initially indicated by the divergence of the numerical correction scheme for the profiles. Figure 4.2 shows the numerical procedure of an infeasible case due to the lack of material flow. It is shown that the neck-down profiles become more flat after 12 iterations. This phenomenon is the same as seen in the solid-core fiber drawing process [11]. The right boundary exists only for hollow optical fiber because high furnace temperature or low drawing speeds may cause the central air core collapse completely. At the right side of this boundary line, the central air core is closed during the drawing process. Therefore, there are two thresholds for the drawing temperature at the same drawing speed. These two boundary lines are nearly vertical since the effect of the drawing speed is relatively weak, which has been indicated by the earlier parameter study.

4.3 Formulation of the objective function

4.3.1 Temperature and velocity lags

It is known that radial non-uniformity in temperature and velocity in the preform are crucial to fiber quality because they can cause a redistribution of the material dopants and impurities [25, 56, 71]. The relative radial temperature difference between the outer surface and the inner surface, namely the temperature lag, is defined as:

$$T_{lag}(z) = \frac{T(r = R_2, z) - T(r = R_1, z)}{T(r = R_2, z)} \tag{4.1}$$

The temperature lag describes the thermal response in the glass. Similarly, the velocity lag in hollow fiber drawing is expressed as:

$$V_{lag}(z) = \frac{V(r = R_2, z) - V(r = R_1, z)}{V(r = R_2, z)} \tag{4.2}$$

Lower temperature and velocity lags in the hollow optical fiber drawing process indicate more uniformity in the radial direction. Therefore, small values of the maximum temperature and velocity lags are desired to obtain high quality of the fiber.

4.3.2 Drawing-induced defect centers

The drawing-induced defect centers, such as E' and non-bridging oxygen hole centers (NBOHCs), are crucial factors in determining the optical properties of fibers since they can cause optical absorption. It was observed that the 630nm absorption is related to the NBOHCs concentration in high-OH-content silica glass. In low-OH-content silica glass, the 630nm absorption is related to the sum of the concentrations of NBOHCs, E' defect centers and peroxy radicals [26]. Therefore, investigations of the drawing-induced defect centers have been of interest in the drawing process. Generally, a low value of the defect concentration is desired for a higher quality of the fiber. The formation mechanism of these drawing-induced defect centers depend strongly on the drawing conditions and the type of silica glass.

E' defects in silica glass are generated from the breaking of the Si-O bond of a potential precursor. The generation of E' defect depends on the temperature history of the fiber. The model given by Hanafusa et al [25] can be used to describe the generation of E' defects in the drawing process.

$$V\frac{dn_{E'}}{dz} = n_{p0}\bar{v}exp\left(-\frac{E_p}{kT}\right) - n_{E'}\bar{v}\left[exp\left(-\frac{E_p}{kT}\right) + exp\left(-\frac{E_d}{kT}\right)\right] \tag{4.3}$$

where $n_{E'}$ is the concentration of E' defects, and n_{p0} is the concentration of the initial precursors, E_p and E_d are corresponding activation energy, $\bar{v}$ is the frequency factor, k is the Boltzmann constant. The values of the constants are given by Hanafusa et al [25]. In the later results, the concentrations of E' defects are normalized by the E' defect concentration at T_{melt} in the equilibrium state, i.e. $5.8285 \times 10^{12} g^{-1}$.

The NBOHC defect is another important kind of defect centers in optical fiber. The generation of NBOHCs is affected by the shear stress besides the temperature history of the fiber. The equation to determine NBOHCs can be expressed as [26]:

$$\frac{dN}{dt} = N_0\left(\frac{\sigma}{\sigma_0}\right)^b exp\left(-\frac{E_c}{kT}\right) \tag{4.4}$$

where N_0, σ_0, b, E_c are constants, and the shear stress σ is defined by

$$\sigma(z) = \frac{F_T}{A(z)} \tag{4.5}$$

where F_T is the drawing Force and A is cross area of hollow fiber.

$$\sigma_0 = \frac{F_T}{A(z=0)} \tag{4.6}$$

Along the streamline, equation (4.4) can be written as:

$$V\frac{dN}{dz} = N_0\left(\frac{\sigma}{\sigma_0}\right)^b exp\left(-\frac{E_c}{kT}\right) \tag{4.7}$$

Integrating equation along the streamline:

$$\frac{N(z)-N(0)}{N_0} = \int_0^z \frac{\left(\frac{\sigma}{\sigma_0}\right)^b exp\left(-\frac{E_c}{kT}\right)}{V(z)}dz \tag{4.8}$$

where the values of the constants are given by $E_c = 3.8eV = 6.114 \times 10^{-19}J, b = 0.75$. The initial concentration of NBOHCs is taken as zero. Due to the lack of constant N_0, the normalized concentration of NBOHCs is defined as:

$$n_{NBOHCs} = \frac{N(z)}{N_0} \tag{4.9}$$

Then the equation for the normalized concentration of NBOHCs is expressed as below:

$$n_{NBOHCs} = \int_0^z \frac{\left(\frac{\sigma}{\sigma_0}\right)^b exp\left(-\frac{E_c}{kT}\right)}{V(z)}dz \tag{4.10}$$

Based on Equations (4.3) and (4.10), E' and NBOHCs defect concentrations in the fiber can be obtained during the drawing process.

The generation of the two kinds of drawing-induced defect centers (E' and NBOHCs') in hollow optical fiber drawing process is investigated. Figure 4.3(a) and (b) show the variations of normalized E' defect and NBOHCs defect concentrations along the axis at different drawing temperatures. The E' and NBOHCs defect concentrations increase along the axis. This trend indicates that E' and NBOHCs defects are generated during the drawing process. It is reasonable because E' and NBOHCs defects are drawing-process-induced defect centers. By comparing Figure 4.3(a) and (b), it is seen that the concentration of E' defect increases mainly in the upper neck-down region where the temperature of the fiber increases. But the generation of NBOHCs defects occurs in the whole neck-down region. This is because the generation of E' defect is only dependent on the temperature history of the fiber. In the lower neck-down region

the temperature of the fiber reaches the equilibrium temperature. So the concentration of E' defects is also in the equilibrium state. For NBOHCs defects, the shear stress in the fiber is another important factor besides the temperature history of the fiber. In the lower neck-down region the shear stress increases dramatically due to the decrease of the cross area of the fiber. This explains why the concentration of NBOHCs defects increases in the whole neck-down region.

The concentrations of E' and NBOHCs defects in the final fibers increase with an increase in the drawing temperature. The reason is that higher drawing temperature leads to higher temperature of the fiber during the drawing process. The generations of E' and NBOHCs defects are dependent on the temperature of the fiber. Equations (4.3) and (4.10) indicate the defects generation terms increase with an increase in the temperature. Therefore, the higher the temperature of the fiber, the higher the concentrations of E' and NBOHCs defects.

4.3.3 Effect of the drawing temperature on the quality of the fiber

The effect of the drawing temperature on the quality of the fiber is investigated. Figures 4.4 (a) and (b) show the variation of the maximum velocity and temperature lag at different drawing temperatures. It is seen that the maximum velocity lag is very sensitive to the drawing temperature. But the maximum temperature lag increases only slightly when the drawing temperature increases. These phenomena are similar to those seen in the results for solid-core fiber drawing [12]. The maximum velocity lag has a minimum at around 2550 K drawing temperature. And the levels are more than 0.6 at 2450 K and 2750 K drawing temperature. It is high at lower drawing temperature because the weak heat input at the glass surface results in a slow thermal response in hollow fiber drawing. At higher drawing temperature, the temperature difference between inner and outer surfaces increases due to the thermal inertia. Therefore the maximum velocity lag is high at extreme high drawing temperature. The maximum temperature lag is not sensitive to the drawing temperature because it strongly depends on the inlet thermal boundary conditions which are not changed here.

Figures 4.4 (c) and (d) show the concentrations of E' and NBOHCs defect in the final

fiber. The concentration of E' and NBOHCs defect increases by more than 6 times and 10 times in magnitude, respectively, when the drawing temperature goes up from 2450 K to 2750 K. The drawing temperature is a very important factor in generating defects. Higher drawing temperatures enhance the formation of E' and NBOHCs defects due to easier bond-breaking of Si-O-Si at high temperatures. These results suggest that minimizing the drawing temperature can dramatically decrease the E' and NBOHCs defects.

The draw tension is another important factor in the strength and quality of the fiber since it strongly affects optical and mechanical properties of the fiber in terms of index of refraction, residual stresses and transmission losses. A low value of the draw tension is desirable from fiber quality considerations and a large value could result in viscous rupture of the fiber [12]. Equation (2.29) is used to calculate the draw tension. The variation of draw tension with the drawing temperature is shown in Figure 4.4(e). The draw tension dramatically increases with a decrease in the drawing temperature. The reason is that the viscous stress increases at lower drawing temperature due to the exponential variation of the glass viscosity with the temperature. Therefore, high drawing temperature is desired for considering the effect of draw tension on the quality of the hollow fiber.

4.3.4 Effect of the preform feeding speed on the quality of the fiber

The effect of the preform feeding speed is shown in Figure 4.5. The preform feeding speed varies from 3mm/min to 4.5mm/min. The drawing temperature is 2600 K. It is seen that the preform feeding speed plays an important role in the E' defect concentration and the draw tension, while the maximum velocity lag, the maximum temperature lag and NBOHCs defect concentration are slightly changed with the preform feeding speed. The draw tension increases with an increase in the preform feeding speed. This phenomenon has been explained in the previous chapter. The E' defect concentration decreases with an increase in the preform feeding speed. It is because a shorter residence time of fiber inside the heating furnace will cause less frequent bond breaking of Si-O.

4.3.5 Optimization

Univariate search method is used to solve the multivariable optimal design problem considered here. In univariate search method, the multivariable problem is reduced to a series of single-variable optimization problems and then the objective function is optimized with respect to one variable at a time [31]. Optimization with respect to the drawing temperature is carried out first. The results discussed before indicates that draw tension, maximum temperature, velocity lag and drawing-induced defect centers, which characterize the quality of the fibers, depend strongly on the drawing temperature of the furnace. Lower drawing temperature decreases the drawing defects concentration but increases the draw tension. The velocity lag is large either at higher drawing temperature or lower drawing temperature. Therefore, an optimum drawing furnace temperature for high quality fiber exists.

The optimization strongly depends on the formulation of the objective function. However, the drawing conditions for hollow optical fiber drawing can be optimized based on the proper formulation of the application. An objective function in terms of fiber quality is proposed as given below:

$$U = \sqrt{\frac{1}{4}\left[\left(\frac{v_{lag}}{\overline{v}_{lag}}\right)^2 + \left(\frac{n_{E'}}{\overline{n}_{E'}}\right)^2 + \left(\frac{n_{NBOHCs}}{\overline{n}_{NBOHCs}}\right)^2 + \left(\frac{F_T}{\overline{F}_T}\right)^2\right]} \tag{4.11}$$

Where four physical quantities, namely the maximum velocity lag, E' and NBOHCs defect concentrations and draw tension, contribute to the quality of the hollow optical fiber. Each variable is normalized by the values at the drawing temperature of 2600 K, which means the objective function equals 1 at 2600 K drawing temperature. The reference values for the maximum velocity lag, E' and NBOHCs defect concentration and draw tension are 0.35, 36.55, 0.01 and 17.3 g respectively. The maximum temperature lag is screened off from the objective function due to the sensitive analysis. At the optimum drawing temperature the objective function reaches a minimum. The feasible domain for hollow fiber drawing at the drawing speed of 10m/s gives the following range for the drawing temperature:

$$2450 \leq T \leq 2750 \tag{4.12}$$

All the other drawing parameters except the drawing temperature are fixed at the values mentioned before.

Curve fitting is chosen to solve this single variable and non-constrained optimum problem. A small number of cases are needed for the curve fitting method because the range of the drawing temperature is narrow for hollow optical fiber drawing. Figure 4.6 shows the objective function and the fitting curve. Here a polynomial function is applied for the curve fitting. It is seen that the objective function decreases sharply and then gradually increases when the drawing temperature increases from 2450 K to 2750 K. The minimum of objective function occurs at 2599.1K where first derivative of the curve fitting function is equal to zero. So the optimum drawing temperature in the first step is obtained as 2599.1K. The objective function behavior shows that the draw tension dominates in hollow fiber quality at lower drawing temperature compared to the effects of defects generation. But at higher drawing temperatures, defect generation contributes more to the objective function than draw tension. These phenomena are also observed in the solid-core fiber drawing process [12]. These can be explained by the exponential variation of the draw tension with the drawing temperature.

The results discussed before also indicate that the optimum preform feeding speed for high quality fiber exists. Lower preform feeding speed can decrease the draw tension. But higher preform feeding speed is desired to achieve low defect concentration and low velocity lag. Figure 4.7 shows the objective function and the fitting curve for optimizing the preform feeding speed at a fixed drawing temperature 2599.1K. The variation of the objective function is a nearly parabolic function with the preform feeding speed. At lower preform feeding speed, the velocity lag and defect concentration dominate in hollow fiber quality over the draw tension. At higher preform feeding speed, the draw tension contributes more to the objective function. The optimum preform feeding speed, calculated from the polynomial fitting curve, is 3.48mm/min. By comparing Figure 4.6 and Figure 4.7, it is seen that the value of the objective function is more sensitive to the drawing temperature than the preform feeding speed. The objective function varies in the range of [1, 3.5] for the drawing temperature and in the range of [1, 1.06] for the preform feeding speed. Therefore, the drawing temperature plays an

important role in the optimal design in hollow optical fiber drawing process.

Besides the drawing temperature and the preform feeding speed, the same optimization procedure with the same objective function can be carried out with respect to the other drawing parameters, such as the temperature profile on the furnace wall, the heat zone length and the diameter of the furnace.

4.4 Summary

The numerical model with the two neck-down profiles correction scheme is used for the optimal design of the hollow optical fiber drawing process in this chapter. The feasible domain for hollow optical fiber drawing process is presented in terms of the drawing temperature and the drawing speed first. The complete collapse of the central cavity and viscous rupture give the limits for the drawing temperature. The possibility of optimum design, based on the drawing temperature and the preform feeding speed, is investigated. The results show that the quality of the fiber, namely maximum velocity lag, drawing-induced defect centers (E' and NBOHCs) and draw tension, strongly depend on the drawing temperature and the preform feeding speed. Either too high or too low value of the drawing temperature or the preform feeding speed will cause low quality of the fiber.

Then an optimal design of the drawing temperature and the preform feeding speed for a typical drawing furnace is carried out. The objective function, comprised of the maximum velocity lag, E' and NBOHCs defect concentrations and draw tension, is defined to characterize the fiber quality. The univariate search method is used to solve the multivariable optimal design problem. The optimum drawing temperature and preform feeding speed are obtained by using curve fitting.

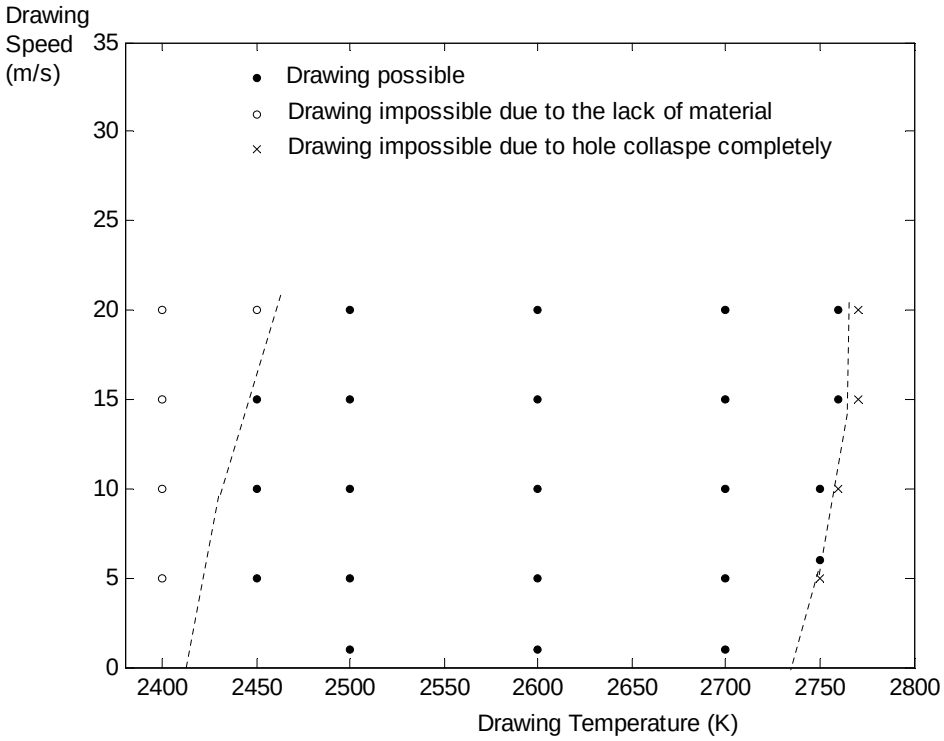

Figure 4.1: Feasible domain for hollow fiber drawing in terms of the drawing speed and the drawing temperature

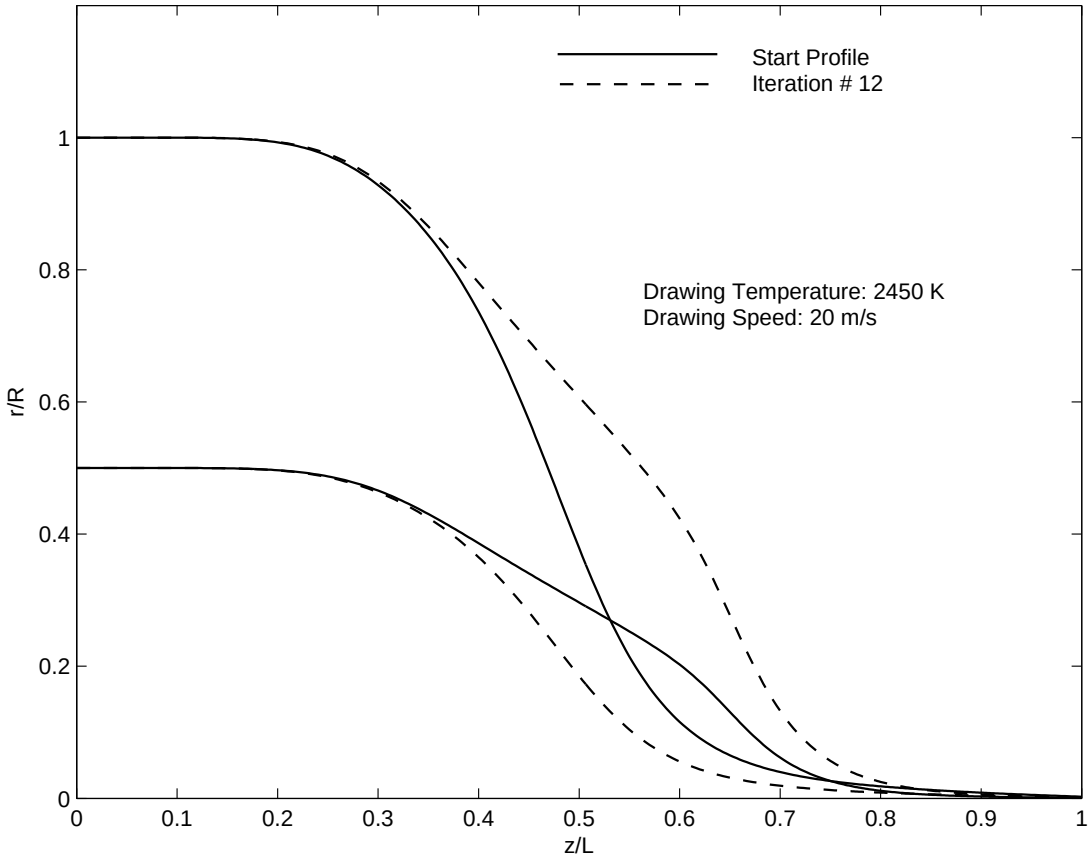

Figure 4.2: Neck-down profile corrections for an infeasible drawing case

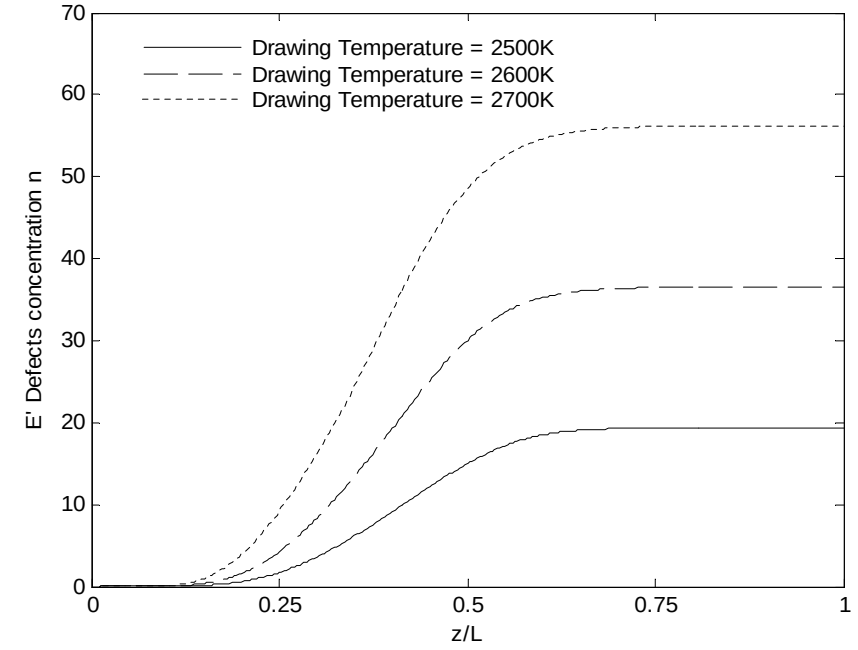

(a)

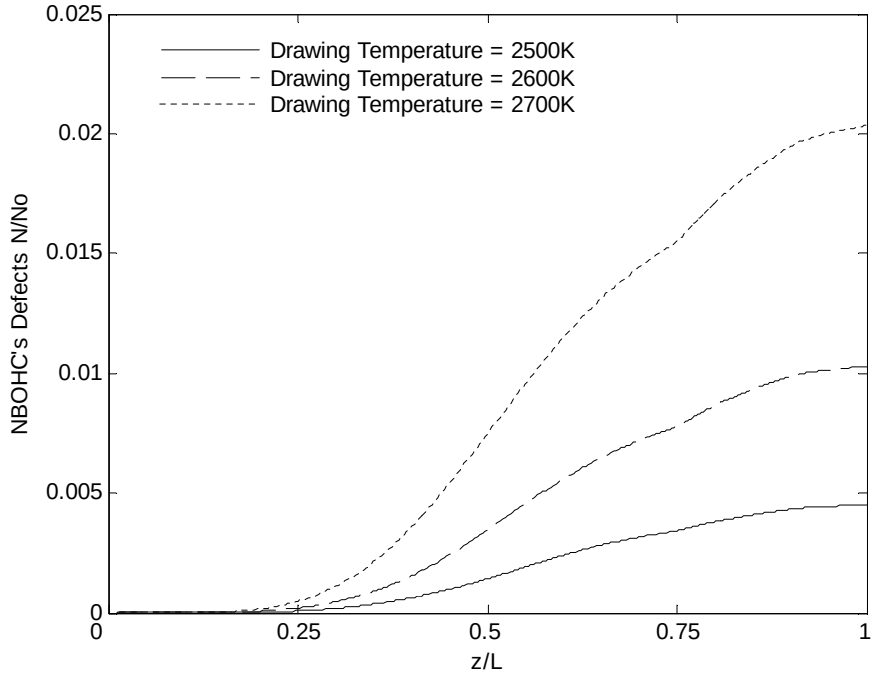

(b)

Figure 4.3: Variation of (a) normalized E' defects concentration (b) normalized NBOHCs defects concentration along the axis at different drawing temperatures

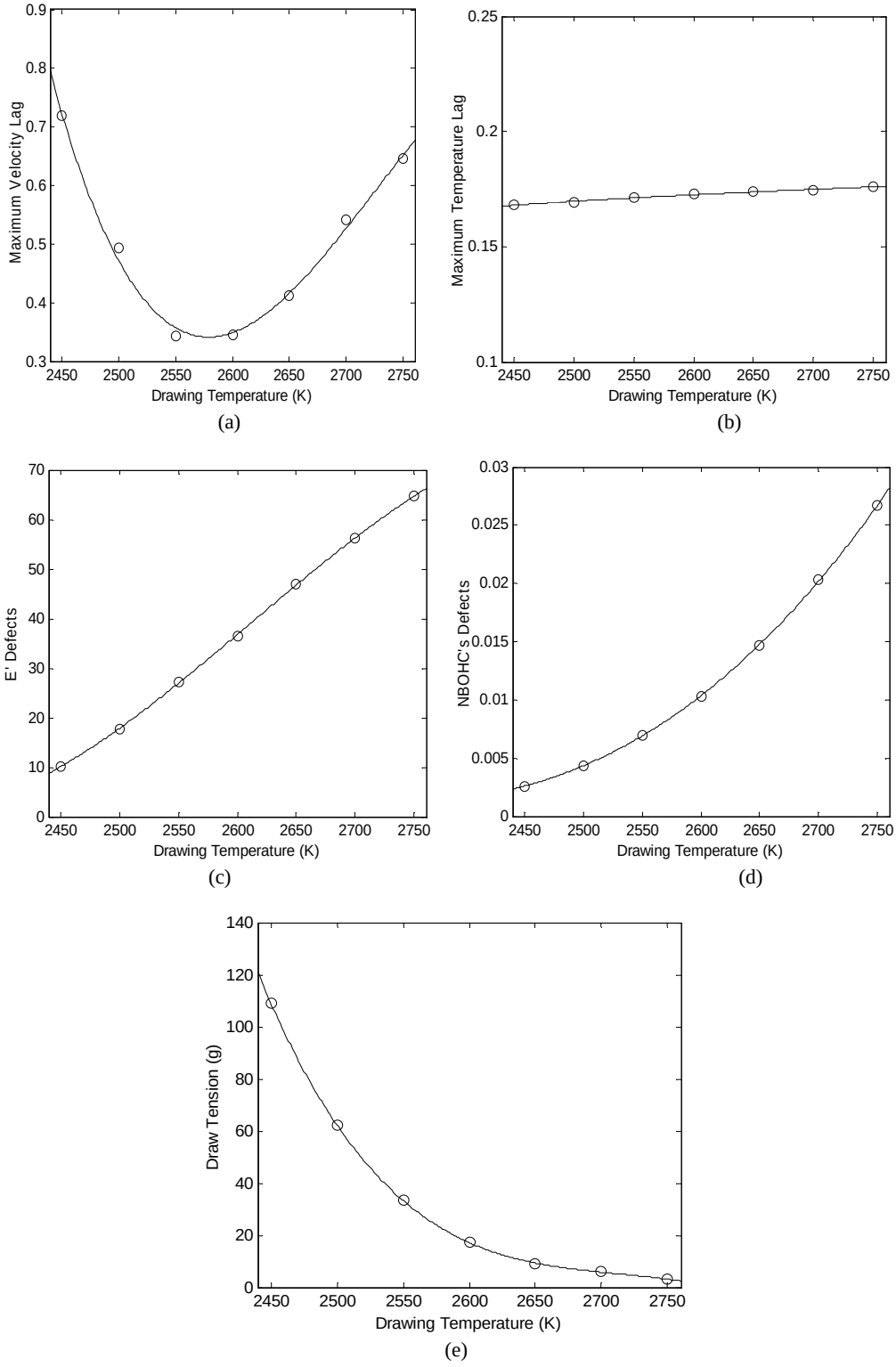

Figure 4.4: Variation of (a) maximum temperature lag, (b) maximum velocity lag (c) E' Defects (d) NBOHCs Defects and (e) Draw Tension with the drawing temperature

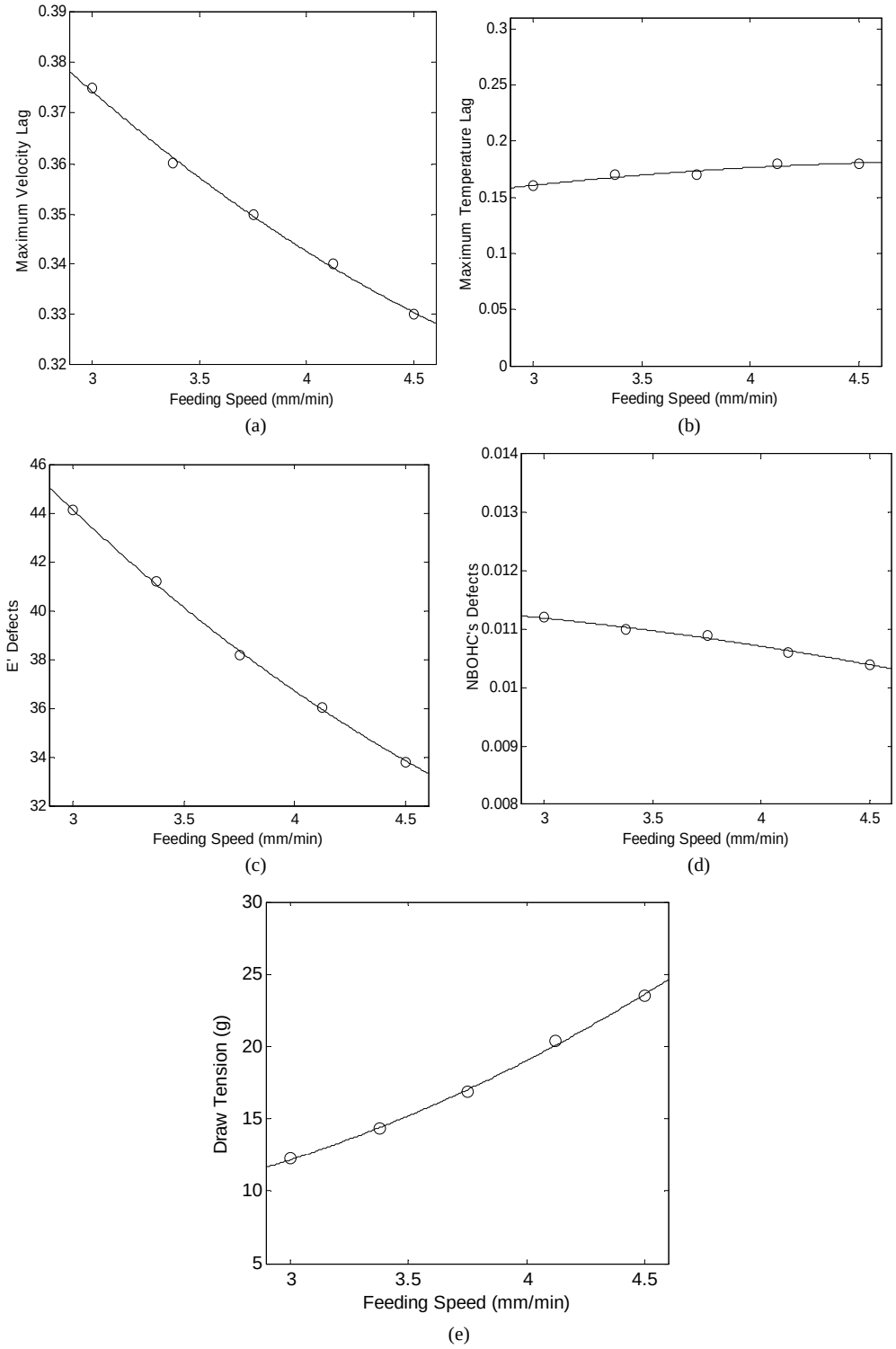

Figure 4.5: Variation of (a) maximum temperature lag, (b) maximum velocity lag (c) E' Defects (d) NBOHCs Defects and (e) Draw Tension with the preform feeding speed

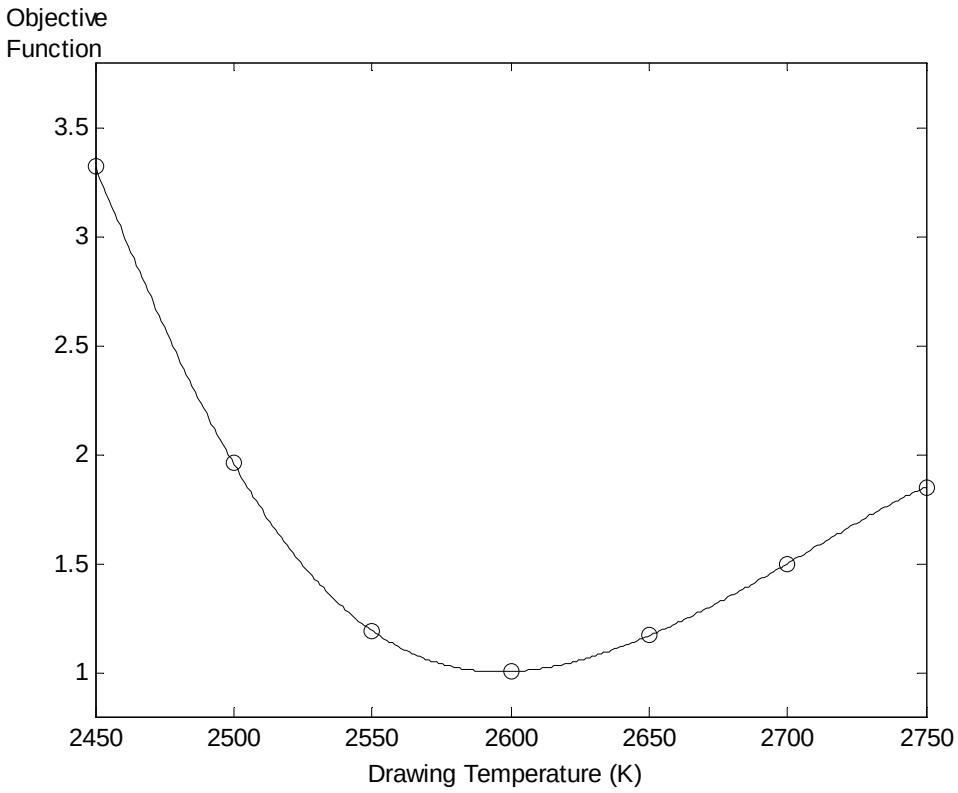

Figure 4.6: Variation of the objective function with the drawing temperature, along with the polynomial fitting curve

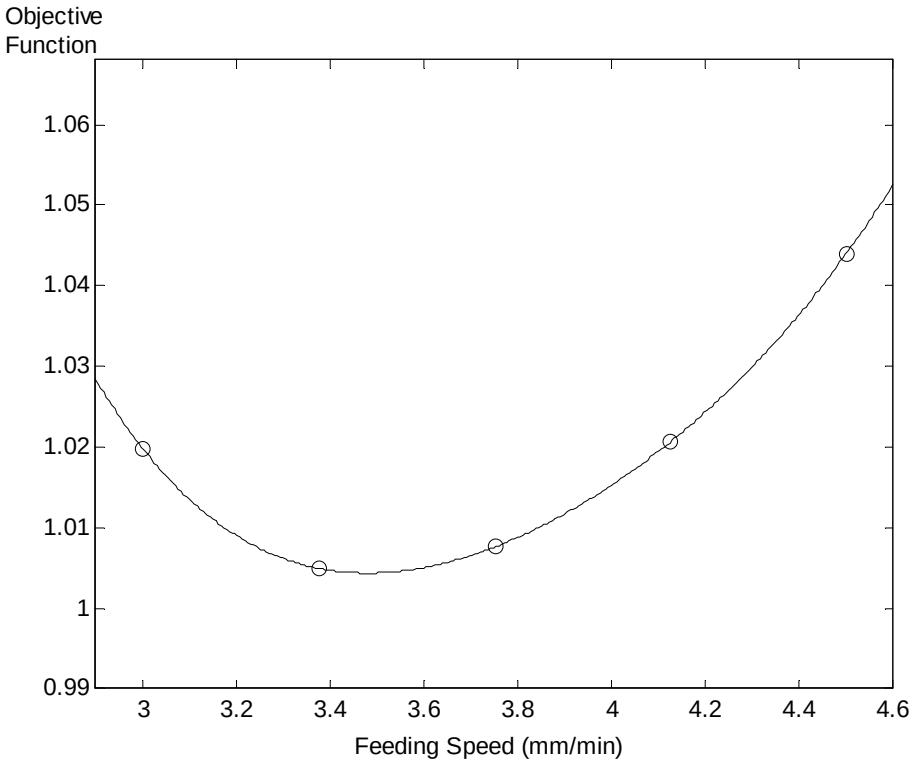

Figure 4.7: Variation of the objective function with the preform feeding speed at fixed drawing temperature 2599.1K, along with the polynomial fitting curve

Chapter 5

Simulation of Microstructured Optical Fiber Drawing Process

5.1 Introduction

Polymer optical fibers (POFs) have been of interest in recent years. POFs have many advantages, like offering a high-bandwidth, being mechanically flexible and easy to install in contrast to a glass optical fiber. However POFs have not yet been widely used due to disadvantages of conventional POFs. For example, the fabrication of the large mode-area graded-index POF is difficult due to the complex polymerization process. The absorption losses in the material limit the choice of polymers to fabricate POFs [16].

The invention of microstructured optical fiber (MOF) is an exciting and important development in optical fibers [13, 16, 17]. Typically, MOFs contain a number of circular air holes running parallel along the fiber. Due to these air holes, MOFs can employ a pattern of microscopic air channels to achieve low signal loss, rather than from variations in the refractive index of the fiber material. MOFs were fabricated from silica first. Then, recently, polymers have been introduced to fabricate microstructured optical fibres. Microstructured polymer optical fibers (MPOFs) have a number of advantages. Most of the disadvantages of conventional POF do not exist in MPOFs. Polymethyl methacrylate (PMMA) is commonly used to fabricate MPOFs. The surface tension of PMMA is an order of magnitude lower than that of silica, while the viscosity of PMMA and silica are of similar magnitudes at their respective draw temperatures. So distortion and collapse of holes due to surface tension effects can be minimized. MPOFs have a range of applications, including telecommunications, optical sensing and automotive industry [17].

However, few studies on the drawing process of MPOFs have been made. Fitt et al [18, 19] investigated the drawing process of an annular hollow fiber which has only one central hole. Deflandre [15] investigated the effect of thermal field on the periodicity and hole shape in the steady-state drawing process. Lyytikainen et al [40] numerically and experimentally investigated the effect of air-structure on the heat transfer within an MPOF preform. Xue et al [65] carried out a scaling analysis on the silica and polymer MOFs drawing process and simulated the isothermal drawing process of an illustrative five-hole structure MPOF. They also presented the experimental results for MPOFs drawing process. Then the contributions of surface tension and viscous effects on the collapse and shape changes of the holes in MPOFs were discussed by Xue et al in a second paper [66]. Reeve et al [52] solved the full axisymmetric conjugate problem, including natural convection, thermal radiation, and prediction of the free surface, to investigate the drawing process of solid-core polymer (PMMA) optical fibers and predict the draw force.

In this chapter, the model proposed in the previous work is modified to simulate the drawing process of MPOFs. The properties of fiber are characterized by the porosity of the cross-sectional area in MPOFs. Results from this model for zero porosity and for one hole are compared with the results for solid-core and annular hollow fibers, respectively, for validation. Results show that they are in good agreement. Then the effects of various parameters, i.e. the geometry of the preform (such as the number of holes and the initial porosity), material properties (such as surface tension) and drawing parameters (such as the drawing speed, the preform feeding speed and the temperature distribution on the furnace wall), on the porosity of the final MPOFs are investigated.

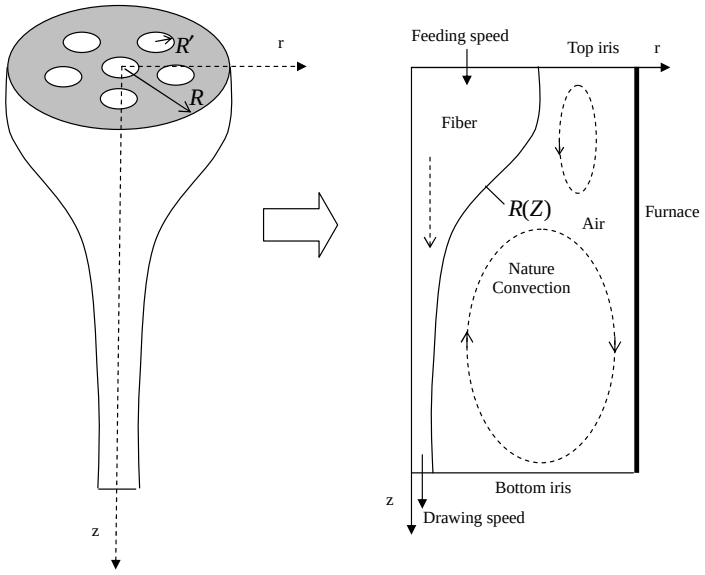

Figure 5.1: Schematic diagram of the drawing process of an MPOF

5.2 Mathematical model

A mathematical model is presented to simulate the drawing process of MPOFs. Figure 5.1 illustrates the drawing process. In the drawing furnace, the air-structured perform/fiber is considered to be a porous media described by porosity. A conjugate problem involves the flow of air-structured fiber and the nature convection flow of air in the furnace. The flows in the furnace are assumed to be laminar, axisymmetric and incompressible. The full governing equations are given by Equation (2.1)-(2.4).

The properties of the porous media are characterized by porosity, which describes the fraction of void in the cross-sectional area. The neck-down profile of MPOF is denoted by $R(z)$. The number and radius of circular air holes in MPOF are denoted

by N and $R'(z)$. Then, the porosity is defined as:

$$\phi = \frac{A_{air}}{A_{total}} = \frac{N \cdot R'(z)^2}{R(z)^2} \tag{5.1}$$

Therefore MPOF with $\phi = 0$ represents Polymer Optical Fiber (POF). The effective properties of the air-structured fiber are defined as:

$$\mu = \phi\mu_{air} + (1-\phi)\mu_{PMMA} \tag{5.2}$$

$$K = \phi K_{air} + (1-\phi)K_{PMMA} \tag{5.3}$$

$$\rho = \phi\rho_{air} + (1-\phi)\rho_{PMMA} \tag{5.4}$$

$$C = \phi C_{air} + (1-\phi)C_{PMMA} \tag{5.5}$$

The boundary conditions are specified as given below: At the top of the preform $(0 \leq r \leq R(0), z = 0)$:

$$u = 0, v = V_0, T = T_0$$

At the fiber exit $(0 \leq r \leq R(L), z = L)$:

$$u = 0, v = V_f, \frac{\partial^2 T}{\partial z^2} = 0$$

Along the furnace wall $(r = R_F, 0 \leq z \leq L)$:

$$u = v = 0, T = T_w(z)$$

Along the symmetric axis $(r = 0, 0 \leq z \leq L)$:

$$u = 0, \frac{\partial v}{\partial r} = 0, \frac{\partial T}{\partial r} = 0$$

At the top of external purge gas $(R(0) < r < R_F, z = 0)$:

$$u = v = 0, T = T_t$$

At the exit of external purge gas $(RL < r < R_F, z = L)$:

$$u = v = 0, \frac{\partial^2 T}{\partial z^2} = 0$$

Along the interface $(r = R(z))$, the stream-function value is set equal to constant and the normal velocity is taken as zero. Force and energy balance equations are applied.

$$\mu \left.\frac{\partial v}{\partial n}\right|_{fiber} = \mu_a \left.\frac{\partial v}{\partial n}\right|_{air}$$

$$u = v \cdot tan(\theta) = v\frac{dR}{dz}$$

$$-K \left.\frac{\partial T}{\partial n}\right|_{fiber} = -K_a \left.\frac{\partial T}{\partial n}\right|_{air} + q_{flux}$$

The heat flux (q_{flux}) is the surface heat flux due to radiation heat transfer, which can be obtained by considering the enclosure consisted of the furnace, the fiber and top and bottom irises. The furnace wall is assumed to be a gray and diffuse surface, with a typical value of 0.75 for the emissivity [23]. The emissivity of the irises and PMMA fiber is taken as 0.96 [50]. Only the radiation heat transfer on the surface of the fiber is taken into account due to the lack of radiative properties of PMMA. The radiation heat transfer within the fiber is neglected here [52]. The radiosity equation in the enclosure is written as:

$$q_i = \epsilon_i \sigma T_i^4 + (1 - \epsilon_i) \sum_{j=1}^{N} F_{i-j} q_j \tag{5.6}$$

where F_{i-j} is the view factor for surface j as seen from surface i on the enclosure.

$$F_{i-j} = \frac{1}{A_j} \left(\int \frac{cos\theta_i cos\theta_j}{\pi S_{i-j}^2} dA_j \right) A_i \tag{5.7}$$

Equation (5.6) is solved by using Gauss-Seidel iterative method with 10^{-5} convergence criterion. The properties for air are considered as functions of temperature. The state equation for an ideal gas and power law correlations are used to compute heat capacity, viscosity and thermal conductivity, which are expressed in equations (3.11)-(3.14). The reference temperature T_{ref} is taken as 300 K. The thermal expansion coefficient of air β is assumed to be constant 0.0023 [52]. The properties of PMMA used in our model are shown in Table 5.1 [52, 64]. In order to prevent instabilities due to very large values of the polymer viscosity, the maximum viscosity is held constant $2.3 \times 10^9 N \cdot s/m^2$ for temperatures below $109°C$ [38, 52].

In order to develop a numerical scheme to determine the neck-down profile of MPOF, $R(z)$, the assumptions that all the holes in the MPOFs have the same behavior and the collapse ratio of every air hole in MPOFs is the same as that of the single annular hole during the drawing process are made. Based on the definition of porosity, Equation (5.1) can be expressed as:

$$R'(z) = \sqrt{\frac{\phi(z)}{N}} \cdot R(z) \tag{5.8}$$

Table 5.1: Properties of PMMA

Properties	PMMA	Units
Density (ρ)	1195	kg/m^3
Viscosity (μ)	$1.506 \times 10^5 exp\left[2935\left(\frac{1}{T} - \frac{1}{170°C}\right)\right]$	$N \cdot s/m^2$
Surface tension coefficient (ξ)	0.03	N/m
Heat capacity (C)	1465	$J/kg \cdot K$
Thermal conductivity (K)	0.193	W/m^2K
Melting temperature (T_{melt})	423	K

The mass conservation equation can be expressed as:

$$R(z) = \sqrt{\frac{v_z(0)}{v_z(z)} \cdot \frac{1-\phi(0)}{1-\phi(z)}} \cdot R(0) \tag{5.9}$$

where the lumped axial velocity v_z can be obtained from Equation (2.16). The collapse ratio for the single annular air hole is applied for every air hole. Therefore,

$$\phi(z) = \phi(0) \times \left(exp\left(-\int_0^z \frac{\xi H' + \xi H}{\mu v} dz\right)\right)^2 \tag{5.10}$$

where H is defined in Equation (2.17). Thus the neck-down profile and porosity can be determined by Equations (5.9) and (5.10).

Typically, MPOF is drawn at a rate of 10 cm/s in a polymer fibre drawing tower. The temperature on the furnace is approximately $175°C$. The outer diameter of MPOFs is about 400 μm. A 369×21 grid is used in the fiber layer and a 369×61 grid is used in the outer gas. The governing transport equations are solved by the same numerical scheme as that described in the Chapter 3.

5.3 Results and discussion

5.3.1 Validation

Solid-core fiber

First, the results obtained from this porous media model with zero porosity are compared with the numerical results for solid-core polymer optical fiber drawing process, as done by Reeve et al [52], for validation. The furnace temperature profiles for cases E1 and E2 are shown in Figure 5.2. Other drawing conditions for cases E1 and E2 are the same as described by Reeve et al [52]. The surface tension is set equal to zero.

Figures 5.3 and 5.4 show the streamlines and contour plots of temperature for cases E1 and E2, respectively. It is clear that two circulations of nature convection flow of air exist in the furnace. In the upper region of the furnace, the circulation is in the counter clockwise direction because the temperature at the furnace wall is higher than the temperature of the fiber. In the lower region of the furnace, the temperature of the fiber is higher than the temperature at the furnace, which leads to a clockwise circulation of nature convection. This bi-cellular flow pattern has been observed and demonstrated by the experimental and analytical results shown by Reeve et al [51, 52]. The temperature contours are also similar to the numerical results.

Figures 5.5 and 5.6 show the temperature distributions along the center line calculated by this model as well as by Reeve et al [52]. It is clear from Figures 5.5 and 5.6 that the results from the present model are very close to the results calculated by Reeve et al [52].

Hollow fiber

The porous media model is also applied to simulate the drawing process of the optical fiber with only one central air hole. The results are validated by comparing with the results for hollow optical fiber drawing process, as presented in the previous chapters. All the drawing conditions are chosen to be the same for these two models. Drawing conditions for case E2 are used. The radius ratio of the preform is set as 0.5, which means the porosity of the preform equals 0.25. The surface tension is magnified to be 0.1 N/m so that it is easy to compare the results of collapse. Figure 5.7 shows the temperature distribution along the outer neck-down profile. The variations of porosity along the axis are shown in Figure 5.8. The porosity decreases along the axis because collapse of the central cavity occurs during the drawing process. It is seen in Figures 5.7 and 5.8 that the results from porous media model are very close to the results from the model for the hollow optical fiber drawing process. The final porosities in the fiber calculated from these two models are 0.215 and 0.217, respectively. Thus, the difference is less than 1%.

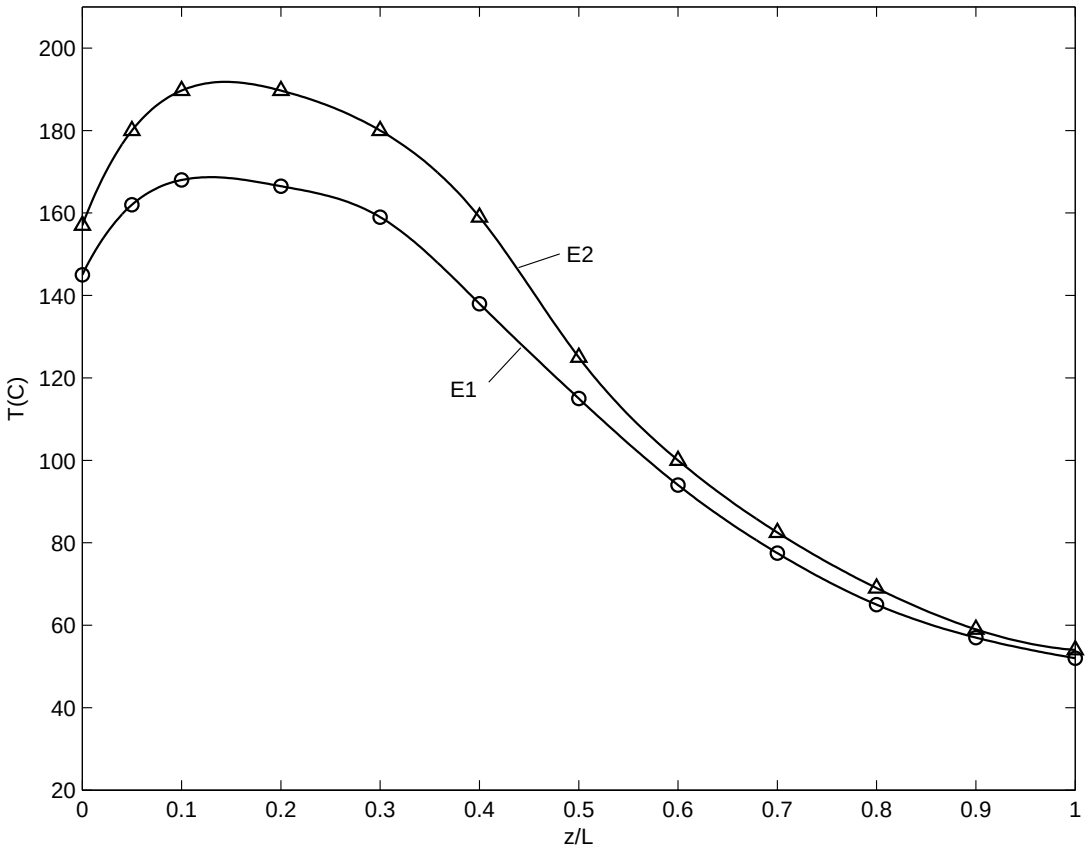

Figure 5.2: Temperature profiles at the furnace wall for cases E1 and E2

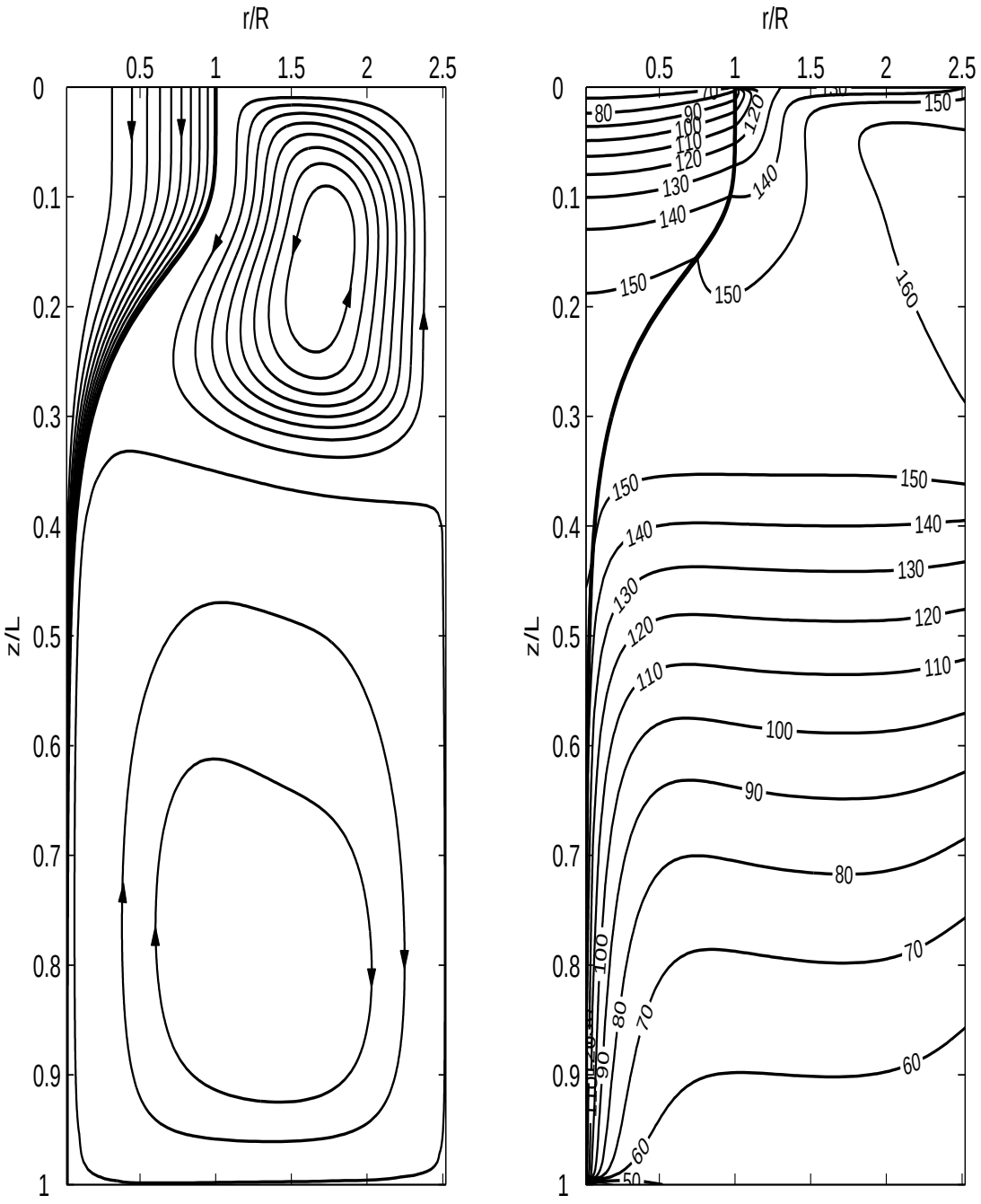

Figure 5.3: Streamlines and temperature contour plots for case E1

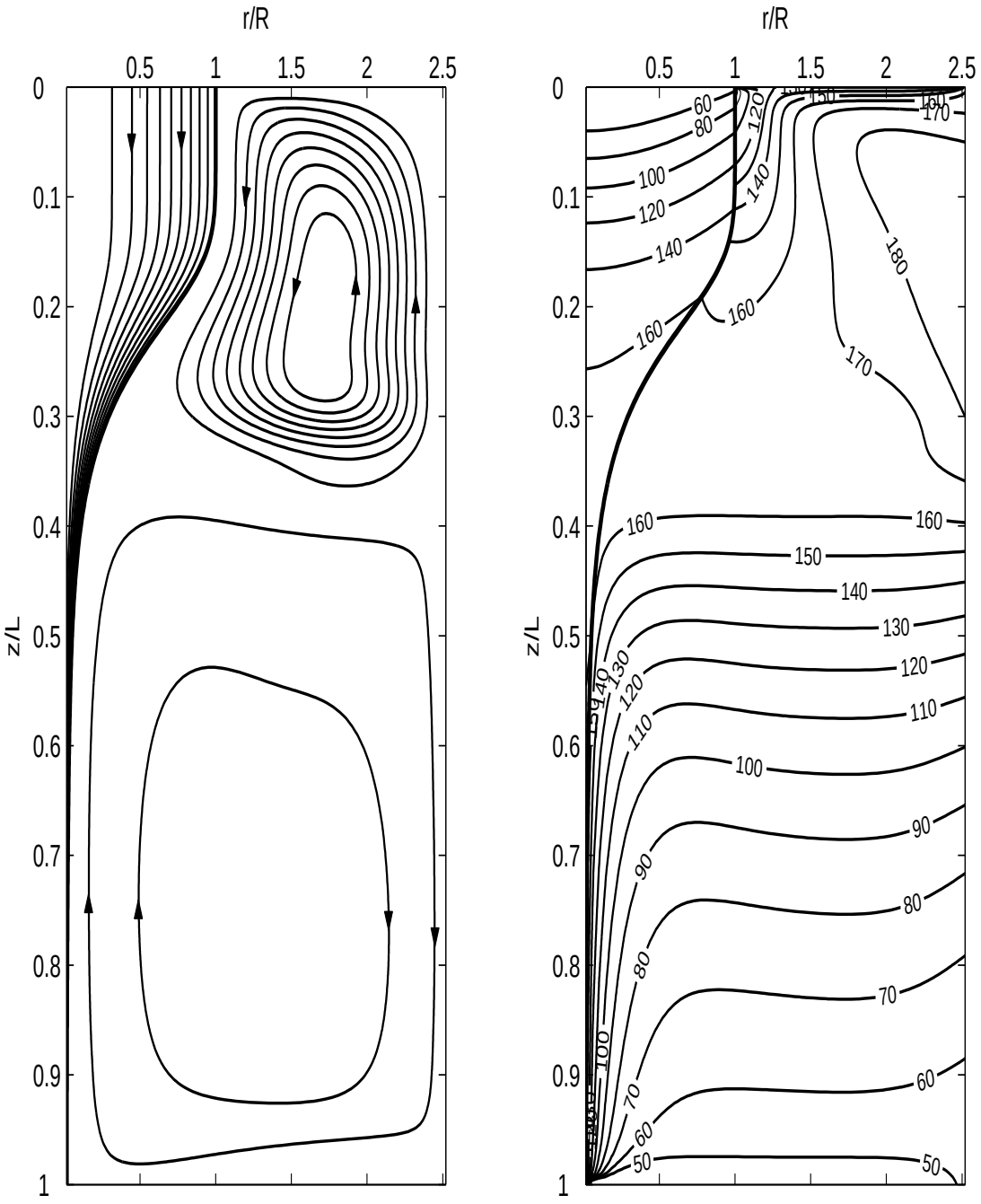

Figure 5.4: Streamlines and temperature contour plots for case E2

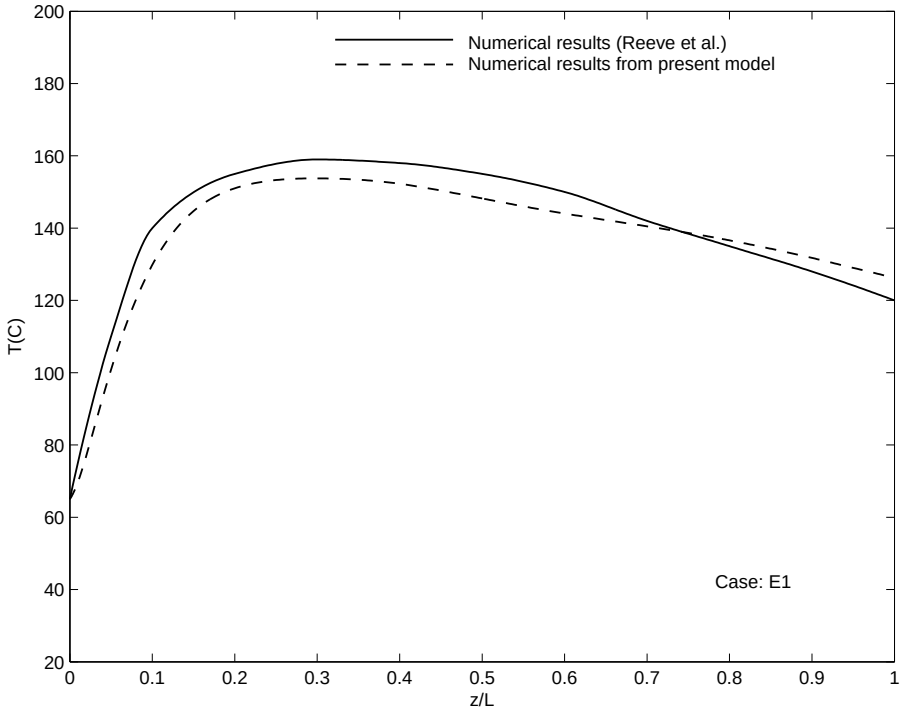

Figure 5.5: Temperature distributions along the center line for case E1 calculated from the present model and the results from Reeve et al (2004)

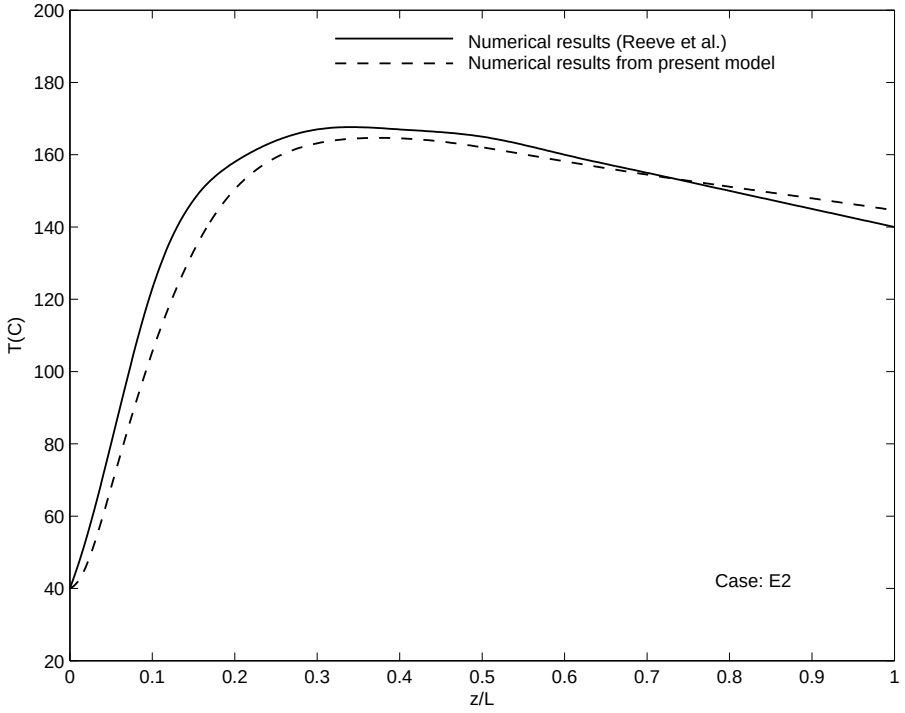

Figure 5.6: Temperature distributions along the center line for case E2 calculated from the present model and the results from Reeve et al (2004)

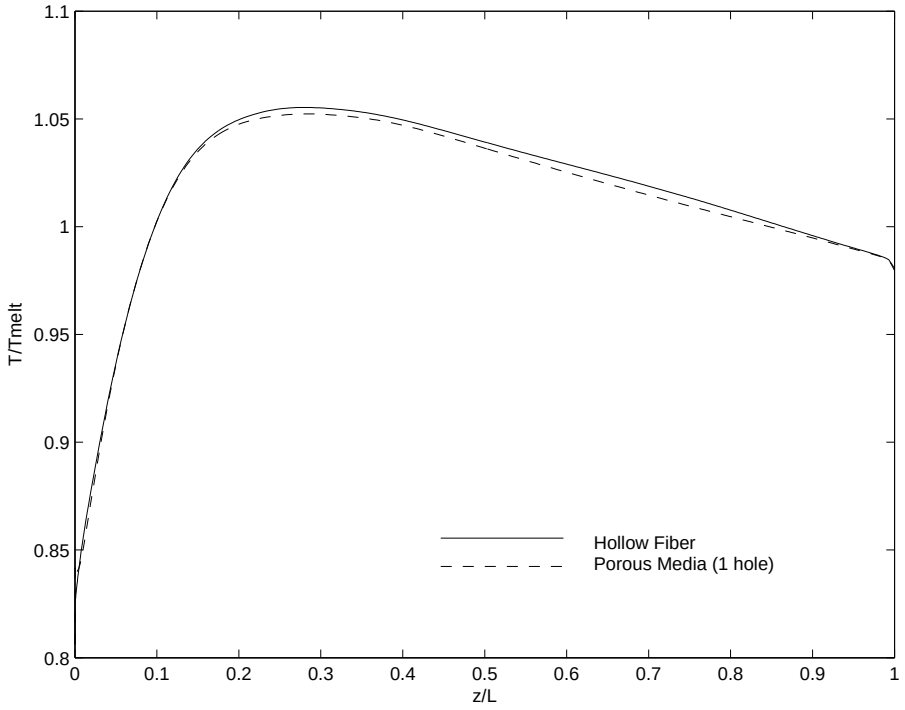

Figure 5.7: Temperature distributions along the outer neck-down profile for the drawing process of the fiber with one central hole

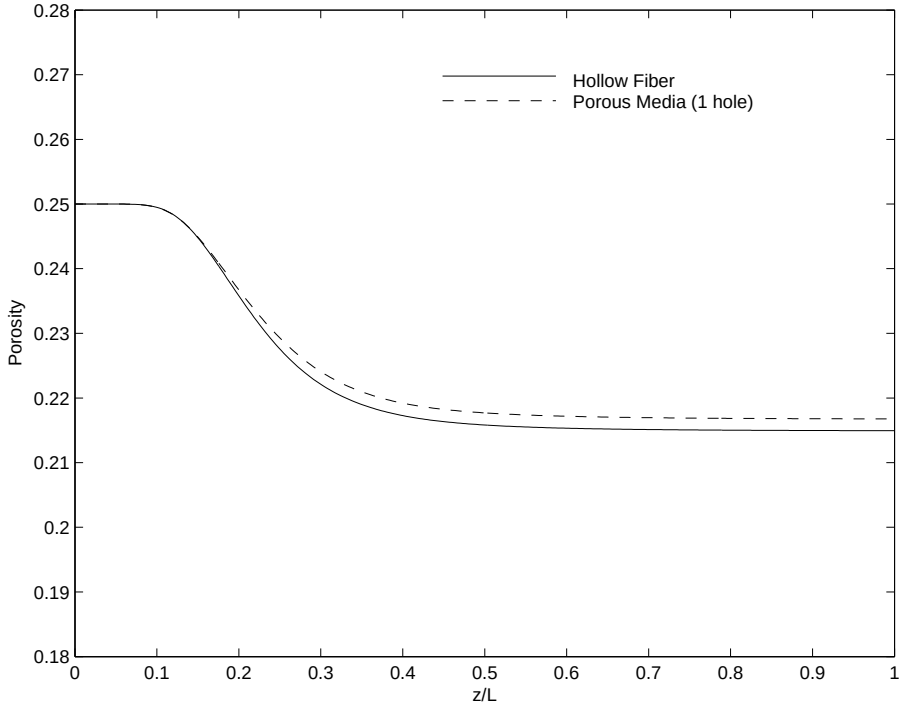

Figure 5.8: Variation of porosity along the axis calculated from the present model and the results for hollow fiber drawing process

5.3.2 Porosity

The drawing furnace used by Reeve [52] is employed here. The furnace diameter is 6.4 cm and its length is 39 cm. The drawing conditions in case E2 is set as the default conditions. The diameter of the preform is 2.54 cm. The preform feeding speed and the drawing speed are 25 $\mu m/s$ and 10 cm/s, respectively. Unless otherwise mentioned, the surface tension of PMMA is 0.03 N/m. The porosity of the preform is 0.25. The number of the air holes is 10.

The effects of porosity on the thermal transport during the drawing process are investigated. The temperature distributions along the center line for different porosity are compared in Figure 5.9. It is seen that the preform with higher porosity is heated up faster and cooled down faster during the drawing process. These phenomena are in agreement with the numerical results presented by Lyytikainen et al [40]. The MPOF with higher porosity has a faster dynamic response than that with lower porosity due to the less mass in the former case.

It has been known that the optical characteristics of MPOFs are strongly dependent on the micro-structure. MPOFs are fabricated by drawing a macroscopical preform down into a microscopical fiber in the drawing furnace. The microstructure patterns in MPOFs come from the structure patterns in preforms. The suitable structure patterns in the MPOFs are designed on a macroscopic scale. Maintaining the structure patterns in the preform during the drawing process is desirable for the manufacture of MPOFs. But it has been experimentally and numerically shown that collapse or deformation may occur during the drawing process of MPOFs. Therefore, collapse and deformation are needed to be minimized. The variation of the porosity of cross section area represents the collapse and deformation of the air holes in this numerical model.

The porosity of the final fiber depends on the geometry of the preform, drawing conditions and material properties. The effects of the geometry of the preform are investigated first. Figure 5.10 shows the variation of the normalized porosity along the axis for different initial porosity. The initial porosity is the porosity of the preform and the normalized porosity is the ratio of porosity to the initial porosity. It is seen that the

normalized porosity starts to decrease further upstream for higher initial porosity. The reason is the preform with higher porosity is heated up faster in the upper neck-down region. The normalized porosity of the final fiber increases with an increase in the initial porosity. This is due to the preform/fiber with higher porosity is cooled down faster in the lower neck-down region.

Three cases, with 2, 10, 50 and 100 holes, are compared to investigate the effect of the number of holes on collapse of air holes. The initial porosities in these three cases are equal to 0.25. All the other drawing conditions are the same as the default values. Figure 5.11 shows the variation of the porosity along the axis for these three cases. It is seen that the porosity of the MPOF with 100 holes decreases more from the initial porosity. The relationship between the final porosity and the number of holes is also shown in Figure 5.12. It is seen that the more holes MPOF has, the greater the collapse. These results are dependent on the assumption of the collapse behavior of centric and eccentric holes. Thus the results from this model can give insight to the collapse during the drawing process of MPOFs.

The surface tension coefficient is another dominating factor in the collapse of air holes, as shown in hollow annular optical fiber drawing process. Figure 5.12 shows the results in terms of porosity ϕ of the final fiber as a function of the number N of air holes for different surface tension coefficient ξ. The variation of the final porosity with the surface tension for different drawing speeds is shown in Figure 5.13. It is found that the collapse of MPOF increases with an increase in surface tension coefficient ξ. There is no collapse if surface tension equals zero. So decreasing the surface tension can minimize collapse or deformation of MPOFs during the drawing process.

The collapse of MPOFs is also dependent on the drawing conditions. Results for different preform feeding speeds and different drawing speeds are compared in Figure 5.13 and Figure 5.14, respectively. It is seen that higher preform feeding speed or drawing speed can decrease the collapse of MPOF. The collapse of MPOF is more sensitive to the preform feeding speed than the drawing speed. The drawing temperature profiles for cases E1 and E2, shown in Figure 5.2, are compared to study the effect of the drawing temperature. Figure 5.15 shows the variations of porosity along the axis for

different drawing temperature. It is seen that the porosity decreases more dramatically at higher drawing temperature. All these phenomena are the same as those observed in hollow annular fiber drawing process, as discussed in chapter 3. The collapse time can be used to explain these as well.

5.4 Summary

In this chapter, the drawing process of MPOFs is investigated. The effective properties of porous media are applied to study the effects of micro-structure in MPOFs. In order to simplify the problem in the model, the collapse ratio of every air hole is assumed to be the same as that of the single annular hole during the drawing process. Based on this assumption a numerical scheme to calculate the porosity and the neck-down profile in the model is proposed. A validation of the model is carried out. The numerical results for solid-core fiber and hollow annular fiber are used for comparison. The model gives excellent agreement with the existing numerical results. Then the effects of the initial porosity on the temperature distribution along the neck-down profile are obtained in the model. These phenomena are in agreement with the numerical results presented by Lyytikainen et al [40]. Finally, parameters, such as initial porosity, the number of holes, the surface tension, the preform feeding speed, the drawing speed and furnace temperature, are changed to study their effects on the collapse of MPOFs during the drawing process. It is shown that the normalized porosity of the final fiber increases with an increase in the initial porosity. For the same initial porosity, the collapse increases with an increase in the number of holes. Lower surface tension, lower furnace temperature, higher preform feeding speed, or higher drawing speed can decrease the collapse of MPOFs. The collapse of MPOF is sensitive to the surface tension, the furnace temperature distribution and the preform feeding speed.

In addition, it is needed to point out that this porous media model is basically an axisymmetric model. The deformation and interaction of holes can not be predicted and simulated in this model.

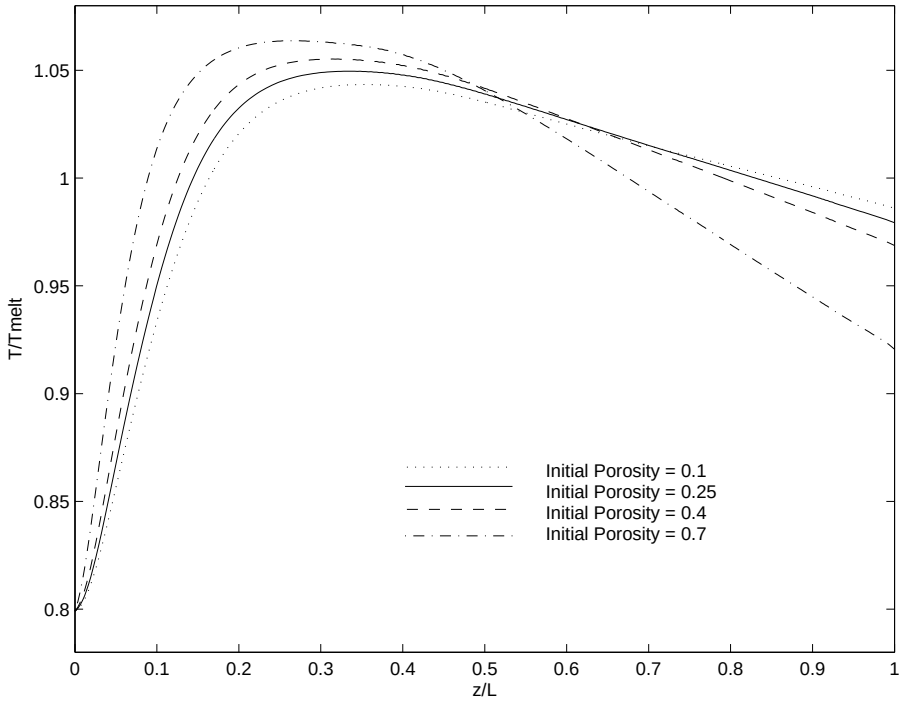

Figure 5.9: Temperature distribution along the surface of MPOF for different initial porosity

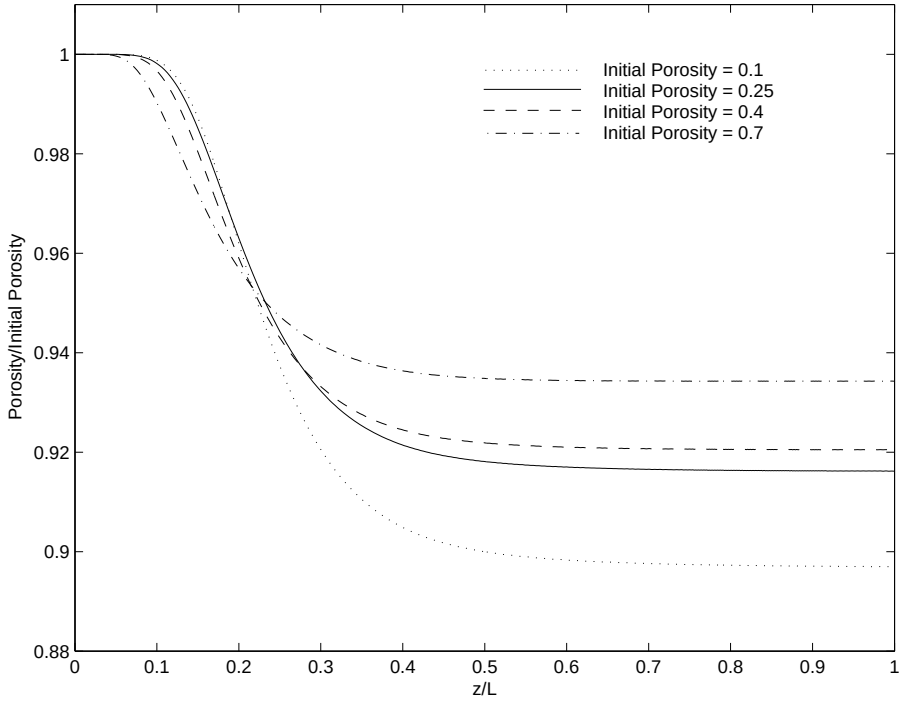

Figure 5.10: Variation of the normalized porosity along the axis for different initial porosity

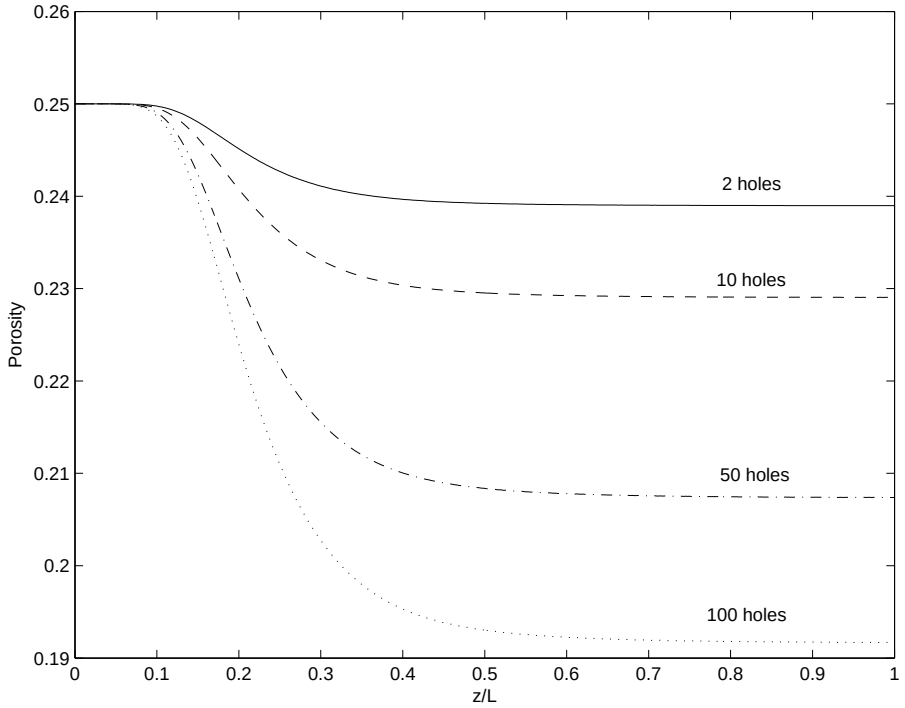

Figure 5.11: Variation of porosity along the axis for different holes

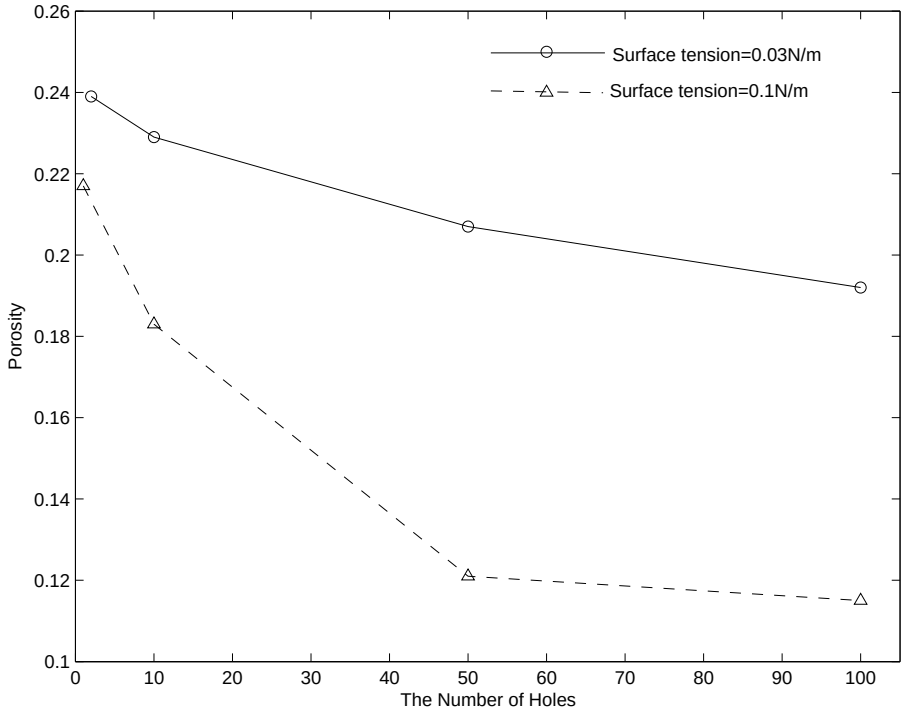

Figure 5.12: Variation of the final porosity with the number of holes for different surface tension

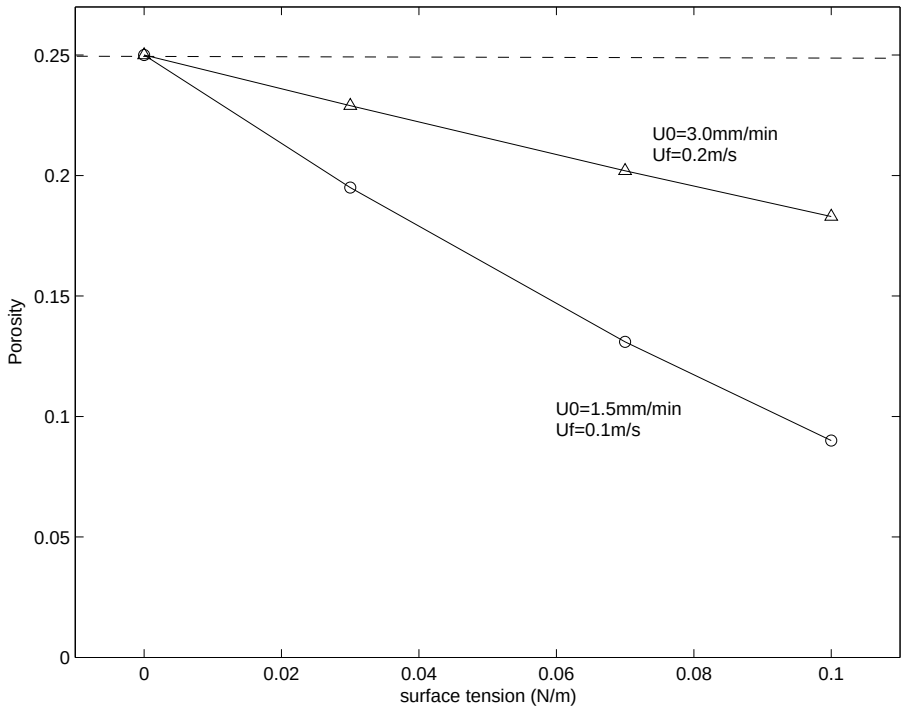

Figure 5.13: Variation of the final porosity with the surface tension for different drawing speeds

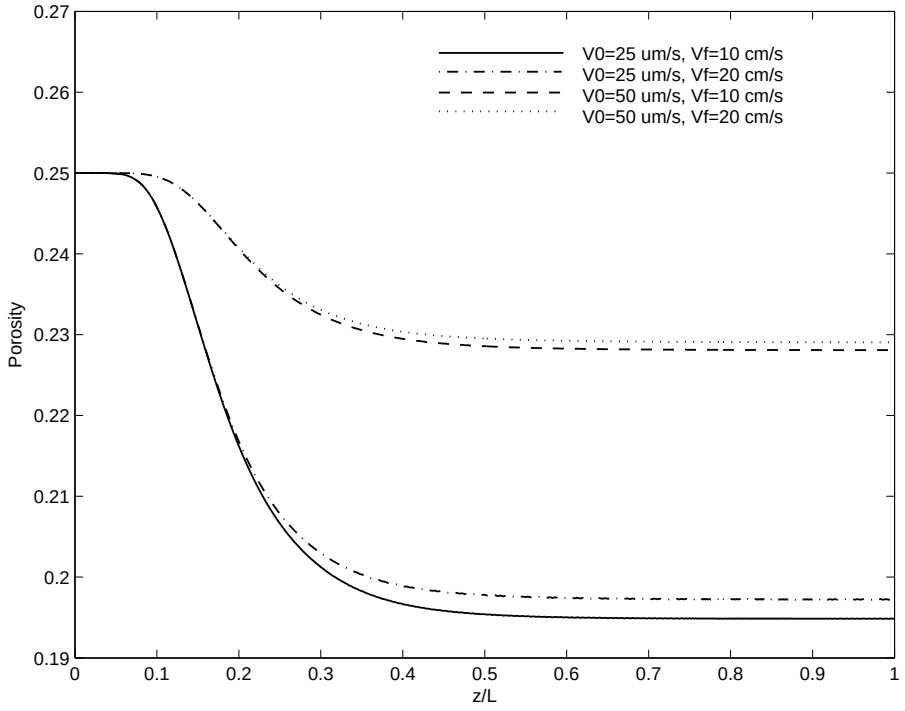

Figure 5.14: Variation of the final porosity with the surface tension for different drawing speeds

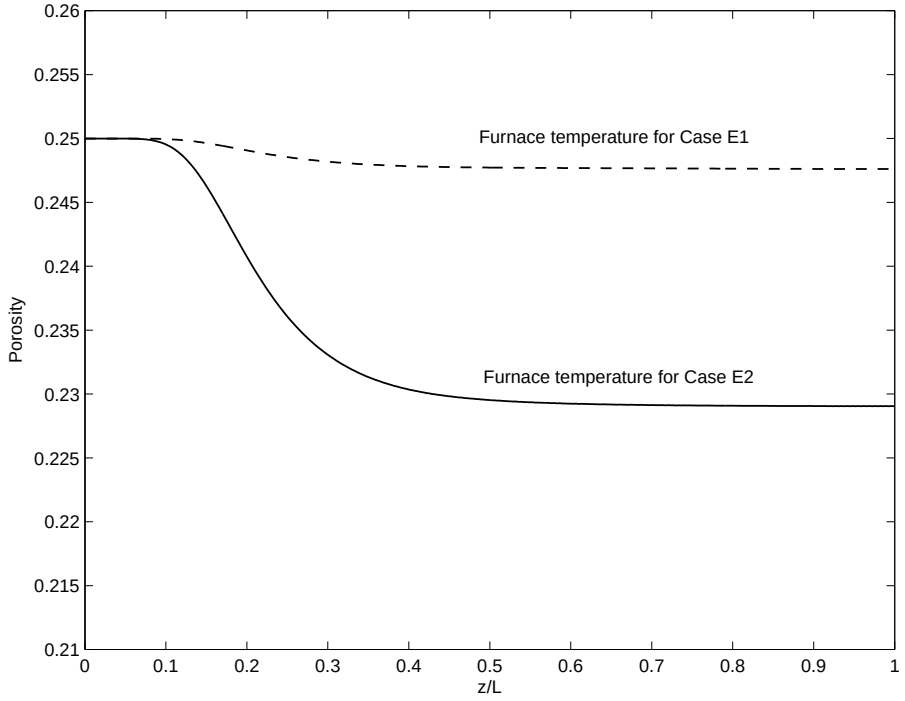

Figure 5.15: Variation of porosity along the axis for different drawing temperature

Chapter 6

Conclusions and Future Work

6.1 Conclusions

The drawing process of hollow optical fiber drawing is investigated in this thesis. The first part of the thesis presents the mathematical model and the numerical scheme with the correction of the two neck-down profiles in hollow optical fiber drawing process. The complex transport process of hollow optical fiber drawing involves conduction, natural and forced convection and radiation transport. Optically thick model as well as the zonal method is applied to simulate the radiation heat transfer within glass. The results from the model are validated by comparing with existing experimental and numerical results for hollow and solid fibers. It is found that the results are in agreement with those in the literature. A comparison between the zonal method and the optically thick method is carried out. The numerical results obtained from these two methods are similar, but there are significant differences. Since the zonal method allows radiation to transmit and be absorbed directly through the medium, the zonal method is more accurate than the optically thick method in hollow optical fiber drawing. The effects of variable properties of air and buoyancy are also investigated by the model. It is found that these effects can be neglected in the hollow optical fiber drawing process.

The parameters, such as the temperature distribution on the furnace wall, the preform feeding speed, the drawing speed and radius ratio of perform, are then varied to study their effect on the thermal transport. The results indicate that the temperature of preform/fiber in the furnace is strongly dependent on the temperature distribution at the furnace wall. The effect of the drawing speed is minor compared to other parameters.

The geometry of the final hollow fiber, which depends on the neck-down profiles,

plays an important role in the optical characteristics and performance of the fiber. The effects of parameters, like drawing conditions, geometry of perform and material properties, on the neck-down profiles are studied. The results show that the neck-down profiles are strongly dependent on the temperature distribution of preform/fiber in the furnace.

Following this study, the collapse ratio is defined to characterize the deformation that occurs in the drawing process. A parametric study on collapse ratio is carried out. The results indicate that collapse ratio can be controlled by changing the pressure difference between the central cavity and the purge gas. Negative pressure difference can prevent collapse of the central cavity. However, a high negative pressure difference may cause the central cavity to enlarge during the drawing process, i.e., "explosion" in the drawing process. The collapse ratio of the final hollow fiber also depends on drawing conditions. It is found that collapse ratio increases with a decrease in the drawing speed, decrease in the preform feeding speed, or with an increase in furnace temperature. So a higher drawing speed, higher preform feeding speed, or lower furnace temperature can avoid the collapse of the central cavity. The surface tension coefficient is another important parameter to collapse of the central cavity. It is shown that there is no collapse if the surface tension equals zero. The collapse ratio of the final hollow fiber increases with an increase in surface tension coefficient. This is why PMMA, whose surface tension coefficient is 0.032 N/m [64], has an advantaged over silica, whose surface tension coefficient is 0.3 N/m, in shape-preservation during the drawing process. The effect of the initial radius ratio of the preform on collapse ratio is also investigated. The results show that the initial radius ratio is not an important factor in the final collapse ratio.

Finally, the effects of the drawing parameters, such as the drawing temperature, the preform feeding speed and the drawing speed, on the draw tension are studied. The draw tension is a crucial factor in the fiber quality. The numerical results show that a higher drawing speed, higher preform feeding speed, or lower furnace temperature can increase the draw tension. And it is also found that the draw tension is very sensitive to the drawing temperature and the preform feeding speed. The drawing speed is a minor

parameter in determining the draw tension in hollow optical fiber drawing process. In addition, the radius ratio of the preform, which indicates the geometry of the preform, is changed to study its effect on the draw tension. The results show that the radius ratio of the preform plays an important role in the draw tension. A smaller the preform radius ratio leads to a higher draw tension.

The second part of the thesis provides an optimal design process in hollow optical fiber drawing process. First, the feasible domain for hollow optical fiber drawing process is presented in terms of the drawing temperature and the drawing speed. On the one hand, hollow optical fiber may be closed in very high furnace temperature. On the other hand, lower furnace temperature may cause failure in drawing process due to viscous rupture. Therefore, the complete collapse of the central cavity and viscous rupture give the limits for the drawing temperature at a given drawing speed.

Then, the possibility of optimum design, based on the drawing temperature and the preform feeding speed, are demonstrated by studying the effects of the drawing temperature and the preform feeding speed on the quality of the fiber, namely the maximum velocity and temperature lags, drawing-induced defect centers (E' and NBOHCs) and draw tension. The results show that the quality of the final hollow fiber is strongly dependent on the drawing temperature and the preform feeding speed. Either too high or too low values in the drawing temperature or the preform feeding speed result in low quality of the fiber.

Finally, an optimal design of the drawing temperature and the preform feeding speed, for a typical drawing furnace, is carried out. The objective function, which is comprised of four equally weighted design qualities, i.e. the maximum velocity lag, E' and NBOHCs defect concentrations and draw tension, is defined to characterize the fiber quality. The maximum temperature lag is screened off from the objective function due to the sensitive analysis. The univariate search method is used to solve multivariable optimal design problem. The optimum drawing temperature and preform feeding speed are obtained by using curve fitting. The optimum conditions are strongly dependent on the formulation of the objective function. However, the present study provides a general optimal design procedure for hollow optical fiber drawing process.

The third part of the thesis studies the drawing process of MPOFs. A porous media model is proposed to simulate the drawing process of MPOFs. The results obtained from this numerical model are compared with the numerical results for the solid-core POF done by Reeve et al [52] and numerical results for hollow POF calculated by the previous model for validation. The predictions are in good agreement with these results.

In this porous media model, the porosity is used to denote the collapse of MPOFs during the drawing process. The effects of parameters, like the initial porosity, the number of the air holes along MPOF, the surface tension, the drawing speed and temperature distribution on the furnace wall, on the final porosity are studied. MPOFs with different initial porosity are compared. It is found that the preform with higher porosity can be heated up and cooled down faster. This phenomenon is demonstrated by the numerical results obtained by Lyytikainen et al [40]. Results from the present study also show that an MPOF with more air holes is easy to collapse. Lower drawing speed, high drawing temperature and high surface tension can cause greater collapse of MPOFs.

6.2 Future work

The results obtained in the present study provide considerable insight into and practical guidance to the drawing process of hollow optical fiber and MPOF. However, there are still several aspects that need to be further investigated.

Hollow optical fibers made of silica and MPOFs made of PMMA are studied in the present study. Further study can focus on fibers made of other material, like softer glass and different polymers.

The optically thick model and the zonal method are applied to model the radiation transport within the glass in the present study. Other models, such as P-1 and discrete ordinates method, can be applied in the future work. The radiation transport within PMMA is neglected in the present study. Provided accurate optical properties of PMMA are obtained, further study can focus on the zonal method to simulate the radiation transport within PMMA.

The stability of hollow fiber drawing process is another important and attractive topic, which is not studied in the present work. Further research on the stability would be needed.

The porous media model presented in the present study can simulate the drawing process of MPOFs. However, the porous media model is an axisymmetric model. The deformation of the air holes and interaction between the air holes during the MPOFs drawing process can not be investigated in this model. Further study can focus on setting up a three dimensional numerical model to simulate the drawing process of MPOFs.

Appendix A

Governing Equations

The non-dimensional variables are defined as:

$$\Psi = \frac{\psi}{V_0 R_{20}^2}; \Omega = \frac{\omega R_{20}}{V_0}; \theta = \frac{T}{T_{melt}}; V = \frac{v}{V_0}; U = \frac{u}{V_0}; t^* = \frac{t}{R_{20}} \tag{A.1}$$

Then the transformed governing equations in terms of non-dimensional variables are expressed as:

In the central cavity:

$$\begin{aligned} &\left(\frac{R_{20}}{R_1}\right)^3 \frac{\partial}{\partial \eta}\left(\frac{1}{\eta}\frac{\partial \Psi}{\partial \eta}\right) + R_1'^2 \eta \left(\frac{R_{20}}{R_1}\right)^3 \frac{\partial^2 \Psi}{\partial \eta^2} \\ &+ \left(\frac{R_{20}}{R_1}\right)^3 \left(2R_1'^2 - R_1'' R_{20}\right) \frac{\partial \Psi}{\partial \eta} - 2R_1' \left(\frac{R_{20}}{R_1}\right)^2 \left(\frac{R_{20}}{L}\right) \frac{\partial^2 \Psi}{\partial \eta \partial \beta} \\ &+ \frac{1}{\eta}\left(\frac{R_{20}}{R_1}\right)\left(\frac{R_{20}}{L}\right)^2 \frac{\partial^2 \Psi}{\partial \beta^2} + \Omega = 0 \end{aligned} \tag{A.2}$$

$$\begin{aligned} &\frac{\partial \Omega}{\partial t^*} + \frac{V_0 R_{20}}{R_1}\frac{\partial (U\Omega)}{\partial \eta} - \frac{\eta V_0 R_{20} R_1'}{R_1}\frac{\partial (V\Omega)}{\partial \eta} + \frac{V_0 R_{20}}{L}\frac{\partial (V\Omega)}{\partial \beta} = \\ &\frac{\mu_a}{\rho_a}\left[\frac{R_{20}}{R_1^2}\frac{\partial}{\partial \eta}\left(\frac{1}{\eta}\frac{\partial (\eta \Omega)}{\partial \eta}\right) + \frac{\eta^2 R_1'^2 R_{20}}{R_1^2}\frac{\partial^2 \Omega}{\partial \eta^2} - \frac{2\eta R_1' R_{20}}{R_1 L}\frac{\partial^2 \Omega}{\partial \eta \partial \beta}\right. \\ &\left. + \frac{R_{20}}{L^2}\frac{\partial^2 \Omega}{\partial \beta^2} - \eta\left(\frac{R_1'' R_{20}}{R_1} - 2R_{20}\left(\frac{R_1'}{R_1}\right)^2\right)\frac{\partial \Omega}{\partial \eta}\right] + \frac{R_{20}^2}{V_0} S_\mu \end{aligned} \tag{A.3}$$

$$\begin{aligned} &\frac{\partial \theta}{\partial t^*} + \frac{V_0 R_{20}}{R_1 \eta}\frac{\partial (\eta U \theta)}{\partial \eta} - \frac{\eta V_0 R_{20} R_1'}{R_1}\frac{\partial (V\theta)}{\partial \eta} + \frac{V_0 R_{20}}{L}\frac{\partial (V\theta)}{\partial \beta} = \\ &\frac{1}{\rho_a C_a}\left[\frac{R_{20}}{R_1^2 \eta}\frac{\partial}{\partial \eta}\left(\frac{\partial (K_a \eta \theta)}{\partial \eta}\right) + \frac{R_{20}}{L^2}\frac{\partial}{\partial \beta}\left(K_a \frac{\partial \theta}{\partial \beta}\right)\right. \\ &- \frac{\eta R_{20}}{L}\frac{\partial}{\partial \beta}\left(\frac{K_a R_1'}{R_1}\frac{\partial \theta}{\partial \eta}\right) - \frac{\eta R_1' R_{20}}{R_1 L}\frac{\partial}{\partial \eta}\left(K_a \frac{\partial \theta}{\partial \beta}\right) \\ &\left. + \frac{\eta R_1'^2 R_{20}}{R_1^2}\frac{\partial}{\partial \eta}\left(K_a \eta \frac{\partial \theta}{\partial \eta}\right)\right] \end{aligned} \tag{A.4}$$

$$U = \frac{R_{20}^2 R_1'}{R_1^2}\frac{\partial \Psi}{\partial \eta} - \frac{R_{20}^2}{R_1 L \eta}\frac{\partial \Psi}{\partial \beta} \tag{A.5}$$

$$V = \frac{R_{20}^2}{R_1^2 \eta} \frac{\partial \Psi}{\partial \eta} \tag{A.6}$$

In the glass layer:

$$\begin{aligned}
\left(\frac{R_{20}^3}{(k_8+\eta)\,R_r}\right) \Bigg[& \left(\frac{\eta^2 R_r'^2}{R_r^2} + \left(\frac{R_1'}{R_r}\right)^2 + \frac{2\eta R_1' R_r'}{R_r^2} \right) \frac{\partial^2 \Psi}{\partial \eta^2} \\
& + \left(\frac{2\eta R_r'^2}{R_r^2} + \frac{2R_1' R_r'}{R_r^2} - \frac{\eta R_r''}{R_r} - \frac{R_1''}{R_r} \right) \frac{\partial \Psi}{\partial \eta} \\
& - \frac{2}{L} \left(\frac{\eta R_r'}{R_r} + \frac{R_1'}{R_r} \right) \frac{\partial}{\partial \beta} \left(\frac{\partial \Psi}{\partial \eta} \right) + \frac{1}{L^2} \frac{\partial^2 \Psi}{\partial \beta^2} \Bigg] \\
& + \left(\frac{R_{20}}{R_r}\right)^3 \frac{\partial}{\partial \eta} \left(\frac{1}{(k_8+\eta)} \frac{\partial \Psi}{\partial \eta} \right) + \Omega = 0
\end{aligned} \tag{A.7}$$

$$\begin{aligned}
& \frac{\partial \Omega}{\partial t^*} + \frac{V_0 R_{20}}{R_r} \frac{\partial (U\Omega)}{\partial \eta} \\
& - V_0 R_{20} \left(\frac{\eta R_r' + R_1'}{R_r} \right) \frac{\partial (V\Omega)}{\partial \eta} + \frac{V_0 R_{20}}{L} \frac{\partial (V\Omega)}{\partial \beta} = \\
& \frac{\mu}{\rho} R_{20} \Bigg[\frac{1}{R_r^2} \frac{\partial}{\partial \eta} \left(\frac{1}{(k_8+\eta)} \frac{\partial \left((k_8+\eta)\,\Omega \right)}{\partial \eta} \right) \\
& + \left(\frac{2\eta R_r'^2}{R_r^2} + \frac{2R_1' R_r'}{R_r^2} - \frac{\eta R_r''}{R_r} - \frac{R_1''}{R_r} \right) \frac{\partial \Omega}{\partial \eta} \\
& + \left(\frac{\eta^2 R_r'^2}{R_r^2} + \left(\frac{R_1'}{R_r}\right)^2 + \frac{2\eta R_1' R_r'}{R_r^2} \right) \frac{\partial^2 \Omega}{\partial \eta^2} \\
& - \frac{2}{L} \left(\frac{\eta R_r' + R_1'}{R_r} \right) \frac{\partial^2 \Omega}{\partial \eta \partial \beta} + \frac{1}{L^2} \frac{\partial^2 \Omega}{\partial \beta^2} \Bigg] + \frac{R_{20}^2}{V_0} S_\mu
\end{aligned} \tag{A.8}$$

$$\begin{aligned}
& \frac{\partial \theta}{\partial t^*} + \frac{V_0 R_{20}}{R_r\,(k_8+\eta)} \frac{\partial \left((k_8+\eta)\,U\theta \right)}{\partial \eta} \\
& - V_0 R_{20} \left(\frac{\eta R_r' + R_1'}{R_r} \right) \frac{\partial (V\theta)}{\partial \eta} + \frac{V_0 R_{20}}{L} \frac{\partial (V\theta)}{\partial \beta} = \\
& \frac{1}{\rho C} R_{20} \Bigg[\frac{1}{R_r^2\,(k_8+\eta)} \frac{\partial}{\partial \eta} \left(K\,(k_8+\eta) \frac{\partial \theta}{\partial \eta} \right) + \frac{1}{L^2} \frac{\partial}{\partial \beta} \left(K \frac{\partial \theta}{\partial \beta} \right) \\
& - \frac{1}{L} \frac{\partial}{\partial \beta} \left(\frac{K\,(\eta R_r' + R_1')}{R_r} \frac{\partial \theta}{\partial \eta} \right) - \frac{\eta R_r' + R_1'}{R_r L} \frac{\partial}{\partial \eta} \left(K \frac{\partial \theta}{\partial \beta} \right) \\
& + \frac{\eta R_r' + R_1'}{R_r^2} \frac{\partial}{\partial \eta} \left(K\,(\eta R_r' + R_1') \frac{\partial \theta}{\partial \eta} \right) \Bigg] \\
& + \frac{R_{20}}{\rho C T_{melt}} \Phi + \frac{R_{20}}{\rho C T_{melt}} S_r
\end{aligned} \tag{A.9}$$

$$U = \frac{R_{20}^2\,(R_r' \eta + R_1')}{(k_8+\eta)\,R_r^2} \frac{\partial \Psi}{\partial \eta} - \frac{R_{20}^2}{(k_8+\eta)\,R_r L} \frac{\partial \Psi}{\partial \beta} \tag{A.10}$$

$$V = \frac{R_{20}^2}{(k_8+\eta)\,R_r^2} \frac{\partial \Psi}{\partial \eta} \tag{A.11}$$

where $R_r = R_2 - R_1; k_8 = \frac{R_1}{R_r}$. In the purge gas region:

$$\left(\frac{R_{20}}{(k_8-\eta)\,R_a}\right)\left[\left(\frac{R_{20}}{L}\right)^2\frac{\partial^2\Psi}{\partial\beta^2}+\eta^2R_a'^2\left(\frac{R_{20}}{R_a}\right)^2\frac{\partial^2\Psi}{\partial\eta^2}\right.$$
$$\left.-\frac{2\eta R_a'R_{20}^2}{R_aL}\frac{\partial}{\partial\beta}\left(\frac{\partial\Psi}{\partial\eta}\right)\right]+\left(\frac{R_{20}}{R_a}\right)^3\frac{\partial}{\partial\eta}\left(\frac{1}{(k_8-\eta)}\frac{\partial\Psi}{\partial\eta}\right)$$
$$+\frac{\eta}{(k_8-\eta)}\left(\frac{R_{20}}{R_a}\right)^2\left(\frac{2R_a'^2R_{20}}{R_a}-R_a''R_{20}\right)\frac{\partial\Psi}{\partial\eta}+\Omega=0 \tag{A.12}$$

$$\frac{\partial\Omega}{\partial t^*}-\frac{V_0R_{20}}{R_a}\frac{\partial\left(U\Omega\right)}{\partial\eta}-\frac{V_0R_{20}\eta R_a'}{R_a}\frac{\partial\left(V\Omega\right)}{\partial\eta}+\frac{V_0R_{20}}{L}\frac{\partial\left(V\Omega\right)}{\partial\beta}=$$
$$\frac{\mu_a}{\rho_a}R_{20}\left[\frac{\eta^2R_a'^2}{R_a^2}\frac{\partial^2\Omega}{\partial\eta^2}-\frac{2\eta R_a'}{R_aL}\frac{\partial^2\Omega}{\partial\eta\partial\beta}-\eta\left(\frac{R_a''}{R_a}-2\left(\frac{R_a'}{R_a}\right)^2\right)\frac{\partial\Omega}{\partial\eta}\right.$$
$$\left.+\frac{1}{R_a^2}\frac{\partial}{\partial\eta}\left(\frac{1}{(k_8-\eta)}\frac{\partial\left(\left(k_8-\eta\right)\Omega\right)}{\partial\eta}\right)+\frac{1}{L^2}\frac{\partial^2\Omega}{\partial\beta^2}\right]+\frac{R_{20}^2}{V_0}S_\mu \tag{A.13}$$

$$\frac{\partial\theta}{\partial t^*}-\frac{V_0R_{20}}{R_a\left(k_8-\eta\right)}\frac{\partial\left(\left(k_8-\eta\right)U\theta\right)}{\partial\eta}$$
$$-\frac{V_0R_{20}\eta R_a'}{R_a}\frac{\partial\left(V\theta\right)}{\partial\eta}+\frac{V_0R_{20}}{L}\frac{\partial\left(V\theta\right)}{\partial\beta}=$$
$$\frac{1}{\rho_aC_a}R_{20}\left[\frac{1}{R_a^2\left(k_8-\eta\right)}\frac{\partial}{\partial\eta}\left(K_a\left(k_8-\eta\right)\frac{\partial\theta}{\partial\eta}\right)+\frac{1}{L^2}\frac{\partial}{\partial\beta}\left(K_a\frac{\partial\theta}{\partial\beta}\right)\right.$$
$$\left.-\frac{\eta}{L}\frac{\partial}{\partial\beta}\left(\frac{K_aR_a'}{R_a}\frac{\partial\theta}{\partial\eta}\right)-\frac{\eta R_a'}{R_aL}\frac{\partial}{\partial\eta}\left(K_a\frac{\partial\theta}{\partial\beta}\right)+\frac{\eta R_a'^2}{R_a^2}\frac{\partial}{\partial\eta}\left(K_a\eta\frac{\partial\theta}{\partial\eta}\right)\right] \tag{A.14}$$

$$U=\frac{R_{20}^2R_a'\eta}{\left(k_8-\eta\right)R_a^2}\frac{\partial\Psi}{\partial\eta}-\frac{R_{20}^2}{\left(k_8-\eta\right)R_aL}\frac{\partial\Psi}{\partial\beta} \tag{A.15}$$

$$V=-\frac{R_{20}^2}{\left(k_8-\eta\right)R_a^2}\frac{\partial\Psi}{\partial\eta} \tag{A.16}$$

where $R_a = R_F - R_2; k_8 = \frac{R_F}{R_a}$.

Appendix B

Glass Properties

In this study, variable properties of glass are taken from Fleming [20]. The thermal conductivity is expressed as [35]:

For $310.78 \leq T \leq 1921.89K$:

$$\begin{aligned} K(T) = \quad & -1.6874325 \times 10^{-11} \left(\tfrac{9T}{5} - 459.4\right)^3 \\ & +4.7386566 \times 10^{-9} \left(\tfrac{9T}{5} - 459.4\right)^2 \\ & +4.3111737 \times 10^{-4} \left(\tfrac{9T}{5} - 459.4\right) + 1.3424434 \end{aligned} \tag{B.1}$$

For $T < 310.78$:

$$K = K(310.78) \tag{B.2}$$

For $T > 1921.89$:

$$K = K(1921.89) \tag{B.3}$$

The surface tension is given as For $T < T_{melt}$:

$$\zeta = 0.17315 \tag{B.4}$$

For $T \geq T_{melt}$:

$$\zeta = 3.375 \times 10^{-5} T + 0.1.902625 \tag{B.5}$$

The specific heat of glass is formulated as For $310.78 \leq T \leq 1699.67K$:

$$\begin{aligned} C_p(T) = \quad & -1.9202379 \times 10^{-11} \left(\tfrac{9T}{5} - 459.4\right)^4 \\ & +8.9608033 \times 10^{-8} \left(\tfrac{9T}{5} - 459.4\right)^3 \\ & -2.00008399 \times 10^{-4} \left(\tfrac{9T}{5} - 459.4\right)^2 \end{aligned} \tag{B.6}$$

$$+0.59235423 \left(\tfrac{9T}{5} - 459.4\right) + 621.75046 \tag{B.7}$$

For $T \leq 310.78$:

$$C_p = C_p\,(310.78) \tag{B.8}$$

For $T \geq 1699.67$:

$$C_p = C_p\,(1699.67) \tag{B.9}$$

The kinematic viscosity of glass is given by an exponential relation [20, 45] as:

$$\nu = 4545.45exp\left(32\left(\frac{T_{melt}}{T} - 1\right)\right) \tag{B.10}$$

The refractive index of glass is constant as 1.42.

Appendix C

Direct Exchange Area

In the zonal method, the computation of the direct exchange areas is an important part. The surface and the volume of the preform/fiber are divided into finite zones. The formulations of direct exchange areas (surface-surface, surface-volume and volume-volume), presented by Chen [7] and Yin [69], are described in this appendix.

C.1 Surface-Surface Direct Exchange Areas

The surface-surface direct exchange area is defined as

$$\overline{S_iS_j} = \int_{A_i}\int_{A_j} exp\left(-a_\lambda S_{ij}\right)\frac{cos\theta_i cos\theta_j}{\pi S_{ij}^2} dA_i dA_j \tag{C.1}$$

where

$$S_{ij} = \sqrt{R_i^2 + R_j^2 - 2R_iR_jcos\phi_j + \left(z_i - z_j\right)^2} \tag{C.2}$$

$$cos\theta_i = \frac{R_i - R_jcos\phi_j + \left(z_j - z_i\right)R_i'}{S_{ij}\sqrt{1+R_i'^2}} \tag{C.3}$$

$$cos\theta_j = \frac{R_j - R_icos\phi_j + \left(z_i - z_j\right)R_j'}{S_{ij}\sqrt{1+R_j'^2}} \tag{C.4}$$

$$dA_i = 2\pi R_i\sqrt{1+R_i'^2}dz_i \tag{C.5}$$

$$dA_j = R_j\sqrt{1+R_j'^2}dz_jd\phi_j \tag{C.6}$$

By substituting these equations into equation (C.1), $\overline{S_iS_j}$ can be written in a general form, as:

$$\overline{S_iS_j} = 2\int_{z_i\min}^{z_i\max}\int_{z_j\min}^{z_j\max}\int_{\phi_j\min}^{\phi_j\max} F\left(z_i, z_j, \phi_j\right)dz_idz_jd\phi_j \tag{C.7}$$

where $F\left(z_i, z_j, \phi_j\right)$ is obtained after the substitution.

In order to save the computational cost, two surface elements i and j assume to be invisible each other when the optical thickness between them is larger than 10. $z_{\min}$

Table C.1: Limiting values for $cos\phi_{j\min}$ and $cos\phi_{j\max}$

	$cos\theta_i \geq 0$	$cos\theta_i \leq 0$
$cos\theta_j \geq 0$	$cos\phi_{j\min} = \min(\Gamma_1, 1)$ $cos\phi_{j\max} = \max(\chi_i, \chi_j, \Gamma_2, -1)$	$cos\phi_{j\min} = \min(\chi_i, \Gamma_1, 1)$ $cos\phi_{j\max} = \max(\chi_j, \Gamma_2, -1)$
$cos\theta_j \leq 0$	$cos\phi_{j\min} = \min(\chi_j, \Gamma_1, 1)$ $cos\phi_{j\max} = \max(\chi_i, \Gamma_2, -1)$	$cos\phi_{j\min} = \min(\chi_i, \chi_j, \Gamma_1, 1)$ $cos\phi_{j\max} = \max(\Gamma_2, -1)$

and $z_{\max}$ represent the limits in axial direction, between which the optical thickness is less than 10. Due to the blocking effect, only the part of the surface j can be viewed from one point on the surface i. This yields the limits $\phi_{j\min}$ and $\phi_{j\max}$for azimuthal angle. The method given by Modest [42] is applied here to determine the limits for azimuthal angle. Table C.1 gives the values for $cos\phi_{j\min}$ and $cos\phi_{j\max}$. The equations for $\chi_i, \chi_j, \Gamma_1, \Gamma_2$ are expressed as:

$$\chi_i = \frac{r_i}{r_j} + \frac{z_j - z_i}{r_j} tan\theta_i \tag{C.8}$$

$$\chi_j = \frac{r_j}{r_i} + \frac{z_i - z_j}{r_i} tan\theta_j \tag{C.9}$$

$$\Gamma_1 = \max\left[\frac{R_1^2(z)(z_j - z_i)^2 - r_i^2(z_j - z)^2 - r_j^2(z - z_i)^2}{2r_i r_j (z - z_i)(z_j - z)}\right]_{z\in(z_i,z_j)} \tag{C.10}$$

$$\Gamma_2 = \min\left[\frac{R_2^2(z)(z_j - z_i)^2 - r_i^2(z_j - z)^2 - r_j^2(z - z_i)^2}{2r_i r_j (z - z_i)(z_j - z)}\right]_{z\in(z_i,z_j)} \tag{C.11}$$

where $R_1(z)$ and $R_2(z)$ are the inner and outer neck-down profiles of the holloe optical fiber.

In order to use the Gaussian Quadrature, following transformations are introduced,

$$\xi_i = \frac{2z_i - z_{i\min} - z_{i\max}}{z_{i\max} - z_{i\min}} \tag{C.12}$$

$$\xi_j = \frac{2z_j - z_{j\min} - z_{j\max}}{z_{j\max} - z_{j\min}} \tag{C.13}$$

$$\varphi_i = \frac{2\phi_i - \phi_{i\min} - \phi_{i\max}}{\phi_{i\max} - \phi_{i\min}} \tag{C.14}$$

Then equation (C.7) is expressed as:

$$\overline{S_i S_j} = 2\int_{-1}^{1}\int_{-1}^{1}\int_{-1}^{1} H(\xi_i, \xi_j, \varphi_j)\, d\xi_i d\xi_j d\varphi_j \tag{C.15}$$

C.2 Surface-Volume Direct Exchange Areas

The surface-volume direct exchange area is defined as:

$$\overline{S_iG_j} = \int_{A_i}\int_{V_j} a_\lambda exp\left(-a_\lambda S_{ij}\right)\frac{cos\theta_i}{\pi S_{ij}^2}dA_i dV_j \tag{C.16}$$

where

$$S_{ij} = \sqrt{R_i^2 + r_j^2 - 2R_i r_j cos\phi_j + \left(z_i - z_j\right)^2} \tag{C.17}$$

$$cos\theta_i = \frac{R_i - r_j cos\phi_j + \left(z_j - z_i\right)R_i'}{S_{ij}\sqrt{1+R_i'^2}} \tag{C.18}$$

$$dA_i = 2\pi R_i\sqrt{1+R_i'^2}dz_i \tag{C.19}$$

$$dV_j = r_j dz_j dr_j d\phi_j \tag{C.20}$$

A general form for equation (C.16) is:

$$\overline{S_iG_j} = 2\int_{z_i\min}^{z_i\max}\int_{z_j\min}^{z_j\max}\int_{r_j\min}^{r_j\max}\int_{\phi_j\min}^{\phi_j\max} F\left(z_i, z_j, r_j, \phi_j\right)dz_i dz_j dr_j d\phi_j \tag{C.21}$$

where $F\left(z_i, z_j, r_j, \phi_j\right)$ is obtained after the substitution.

$r_{\min}$ and $r_{\max}$ representing the limits in radial direction are taken from the geometric limits for V_j. Other limits are determined by the same method as surface-surface direct exchange areas. For r_j, following transformation is introduced:

$$\eta_j = \frac{2r_j - r_{j\min} - r_{j\max}}{r_{j\max} - r_{j\min}} \tag{C.22}$$

Then equation (C.21) is expressed as:

$$\overline{S_iG_j} = 2\int_{-1}^{1}\int_{-1}^{1}\int_{-1}^{1}\int_{-1}^{1} H\left(\xi_i, \xi_j, \eta_j, \varphi_j\right)d\xi_i d\xi_j d\eta_j d\varphi_j \tag{C.23}$$

C.3 Volume-Volume Direct Exchange Areas

The volume-volume direct exchange area is defined as:

$$\overline{G_iG_j} = \int_{V_i}\int_{V_j} a_\lambda^2\frac{exp\left(-a_\lambda S_{ij}\right)}{\pi S_{ij}^2}dV_i dV_j \tag{C.24}$$

where

$$S_{ij} = \sqrt{r_i^2 + r_j^2 - 2r_i r_j cos\phi_j + \left(z_i - z_j\right)^2} \tag{C.25}$$

$$dV_i = 2\pi r_i dz_i dr_i \tag{C.26}$$

$$dV_j = r_j dz_j dr_j d\phi_j \tag{C.27}$$

A general form for equation (C.24) is:

$$\overline{G_i G_j} = 2 \int_{z_i\min}^{z_i\max} \int_{r_i\min}^{r_i\max} \int_{z_j\min}^{z_j\max} \int_{r_j\min}^{r_j\max} \int_{\phi_j\min}^{\phi_j\max} F\left(z_i, r_i, z_j, r_j, \phi_j\right) dz_i dz_j dr_j d\phi_j \tag{C.28}$$

where $F\left(z_i, r_i, z_j, r_j, \phi_j\right)$ is obtained after the substitution.

For r_i, following transformation is introduced:

$$\eta_i = \frac{2r_i - r_{i\min} - r_{i\max}}{r_{i\max} - r_{i\min}} \tag{C.29}$$

Then equation (C.28) is expressed as:

$$\overline{G_i G_j} = 2 \int_{-1}^{1} \int_{-1}^{1} \int_{-1}^{1} \int_{-1}^{1} \int_{-1}^{1} H\left(\xi_i, \eta_i, \xi_j, \eta_j, \varphi_j\right) d\xi_i d\xi_j d\eta_j d\varphi_j \tag{C.30}$$

References

[1] Abel, T., Hirsch, J., and Harrington, J. A., Hollow glass waveguides for broadband infrared transmission, *Opt. Lett.*, 1994, vol. 19, 1034-1036.

[2] Artjushenko, V. G., Butvina, L. N., Vojtsekhovsky, V. V., et al, Mechanisms of optical losses in polycrystalline KRS-5 fibers, *J. Lightwave Tech.*, 1986, vol. LT-4, 461-465.

[3] Burmeister, L. C., Convective Heat Transfer, 1983, John Wiley & Sons, New York.

[4] Chakravarthy, S. S. and Chiu, W. K. S., Collapse Prediction During Hollow Optical Fiber Fabrication, 2005 ASME Summer Heat Transfer Conference, 2005, San Francisco, California, USA.

[5] Chen, C., Transport processes in Drawing of Optical Fibers with Core-cladding Structure, Ph. D. dissertation, 2007, New Brunswick, New Jersey.

[6] Chen, C. and Jaluria, Y., Numerical Simulation of Transport in Optical Fiber Drawing with Core-cladding Structure, ASME Heat Transfer/Fluids Engineering Summer Conference, 2004, Charlotte, North Carolina, USA.

[7] Chen, C. and Jaluria, Y., "Modeling of radiation heat transfer in the drawing of an optical fiber with multi-layer structure," *ASME J. Heat Transfer*, 2007, Vol. 129(3), 342-352.

[8] Chen, C. and Jaluria, Y., Numerical Simulation of Transport in Optical Fiber Drawing with Core-Cladding Structure, *J. of Heat Transfer*, 2007, Vol. 129, 559-567.

[9] Cheng, X., Design and Optimization of the Draw Furnace for High Speed Optical Fiber Drawing, Ph. D. dissertation, 2002, New Brunswick, New Jersey.

[10] Cheng, X. and Jaluria, Y., Effect of Draw Furnace Geometry on High-speed Optical Fiber Manufactureing, *Numerical Heat Transfer*, 2002, Part A, Vol. 41, 757-781.

[11] Cheng, X. and Jaluria, Y., Feasibility of High Speed Furnace Drawing of Optical Fibers, *J. of Heat Transfer*, 2004, Vol. 126, 852-857.

[12] Cheng, X. and Jaluria, Y., Optimization of a thermal manufacturing process: Drawing of optical fibers, *International Journal of Heat and Mass Transfer*, 2005, Vol. 48, 3560-3573.

[13] Choi, J., Kim, D. Y., and Peak, U. C., Fabrication of properties of polymer photonic crystal fibre, *Proc. Plastic Optical Fibre Conf.*, 2001, Amsterdam, Netherlands, 355-360.

[14] Cregan, R.F., Mangan, B.J., Knight, J.C., et al, Single mode photonic band gap guidance of light in air, *Science*, 1999, Vol. 285, 1537-1539

[15] Deflandre, G., Modeling the manufacturing of complex optical fibres: The case of the holey fibres, *Proc. 2nd Int. Colloquium*, 2002, Valenciennes, France, 150-156

[16] Eijkelenborg, M. A., Large, M. C. J., Argyros, A. et al, Microstructured polymer optical fibre, *Opt. Express*, 2001, Vol. 9(7), 319-327

[17] Eijkelenborg, M. A., Argyros, A., Barton, G. et al, Recent progress in microstructured polymer optical fibre fabrication and characterisation, *Optical Fiber Technology*, 2003, Vol. 9, 199-209

[18] Fitt, A. D. and Furusawa, K., Monro, T. M. and Please, C. P., Modeling the Fabrication of Hollow Fibers: Capillary Drawing, *J. Lightwave Tech.*, 2001, Vol. 19(12), 1924-1931.

[19] Fitt, A. D., Furusawa, K., Monro, T. M., Please, C. P. and Richardson D. J., The Mathematical Modelling of Capillary Drawing for Holey Fibre Manufacture, *J. Eng. Math.*, 2002, Vol. 43, 201-227.

[20] Fleming, J. D., Fused Silica Manual. Final Report for the U. S. Atomic Energy Commission, 1964, Oak Ridge, Tennessee, Project No. B-153.

[21] Fotiadis, D.I., Boekholt, M. and Jensen, K.F., Flow and heat transfer in CVD reactors: comparison of Raman temperature measurements and finite element model predictions, *J. Crystal Growth*, 1990, Vol. 100, 577-599.

[22] Gebhart, B., Jaluria, Y., Mahajan, R. L. and Sammakia, B., Buoyancy-induced Flows and Transport, Hemisphere Publishing Co., 1988, Washington.

[23] Gubareff, G. G., and Janssen, J.E., Thermal Radiation Properties Survey, 1960, Honeywell.

[24] Harrington, J. A., Selected Papers on Infrared Fiber Optics, Milestone Series, 1990, Vol. MS-9, SPIE Press, Bellingham, WA, SPIE Press, Bellingham, WA.

[25] Hanafusa, H., Hibino, Y. and Yamamoto, F., Formation mechanism of drawing-iduced E' centers in silica optical fibers, *J. Appl. Phys.*, 1985, Vol. 58(3), 1356-1361.

[26] Hibino, Y. and Hanafusa, H., Defect structure and formation mechanism of drawing-induced absorption at 630 nm in silica optical fibers, *J. Appl. Phys.*, 1986, Vol. 60(5), 1797-1801.

[27] Hecht, J., Understanding fiber optics, 2002, Prentice Hall.

[28] Homsy, G. M. and Walker, K., Heat transfer in laser drawing of optical fibers, *Glass Tech.*, 1979, Vol. 20(1), 20-26.

[29] Izawa, T., Sudo, S., Optical fibers: Material and Fabrication, KTK Scientific Publishers, 1987, Tokyo.

[30] Jaluria, Y., Torrance, K., Computational Heat Transfer, Taylor and Francis, 2003, NY.

[31] Jaluria, Y., Design and Optimization of Thermal Systems, McGraw-Hill, 1998.

[32] Kaminski, D. A., Thermal transport in optical fiber manufacturing, *Proceedings of the first international symposium on radiative heat transfer*, 1995, M. Pinar Menguc ed., Begell House, New York, 667-681.

[33] Kao, C. K. and Hockham, G. A., Dielectric-fiber surface wave-guide for optical frequencies, *Proc. IEE (Lond.)*, 1966, Vol. 133, 1151-1158 (Errata: *Opt. Lett.*, 1997, Vol. 22, 484-485)

[34] Knight, J. C., Birks, T. A., Russell, P. St. J. et al, All-silica single-mode fibre with photonic crystal cladding, *Opt. Lett.*, 1996, Vol. 21, 1547-1549 (Errata: *Opt. Lett.*, 1997, Vol. 22, 484-485)

[35] Lee, S. H. -K., Numerical Investigation on the Neck-down Region of a Furnace drawn Optical Fiber, Ph. D. dissertation, 1993, Rutgers University, New Brunswick, New Jersey.

[36] Lee, S. H. -K. and Jaluria, Y., The Effects of Geometry and Temperature Variations on the Radiative Transport during Optical Fiber Drawing, *J. Material Processing and Manufacturing Sci.*, 1995, Vol. 3, 317-331.

[37] Lee, S. H. -K. and Jaluria, Y., Effects of Streamwise Convergence in Radius on the Laminar Forced Convection in Axisymmetric Ducts, *Numerical Heat Transfer*, 1995, Vol. 28, 19-38.

[38] Lee, S. H. -K. and Jaluria, Y., Effects of Variable Properties and Viscous Dissipation During Optical Fiber Drawing, *ASME Journal Heat Transfer*, 1996, Vol. 118, 350-358.

[39] Levich, V. G. and Krylov, V. S., Surface-tension Driven Phenomena, *Annual Review of Fluid Mechanics*, 1969, Vol. 1, 293-316

[40] Lyytikainen, K., Zagari, J., Barton, G. et al, Heat transfer within a microstructured polymer optical fibre preform, *Modelling Simul. Mater. Sci. Eng.*, 2004, Vol. 12, 255-265.

[41] Manfre, G., Forces Acting In the Continuous Drawing of Glass Fibers, *Glass Technology*, 1969, Vol. 10, 99-106.

[42] Modest, M. F., Radiative shape factors between differential ring elements on concentric axisymmetric bodies, *J. of Thermophysics*, 1998, Vol. 2, 86-88.

[43] Monro, T. M., Belardi, W., Furusawa, K., et al, Sensing with microstructured optical fibres, *Meas. Sci. Technol.*, 2001, Vol. 12, 854-858.

[44] Murata, H., Handbook of optical fibers and cables, 1988, Marcel Dekker Inc.

[45] Myers, M. R., A Model for Unsteady Analysis of Perform Drawing, *AIChE J.*, 1989, Vol. 35, 592-602.

[46] Nubling, R. and Harrington, J. A., Optical properties of single-crystal sapphire fibers, *Appl. Opt.*, 1997, vol. 36, 5934-5940.

[47] Okoshi, T., Optical Fibers, Academic Press, 1982, London.

[48] Paek, U. C. and Runk, R. B., Physical Behavior of the Neck-down Region During Furnace Drawing of Silica Fibers, *J. Appl. Phys.*, 1978, Vol. 49(8), 4417-4422.

[49] Poulain, M., Chanthanasinh, M., and Lucas, New fluoride glasses, *J. Mat. Res. Bull.*, 1977, vol. 12, 151-156.

[50] Reeve, H. M., Mescher, A. M., Emery, A. F., Experimental and numerical investigation of polymer preform heating, *J. Mater. Process. Manuf. Sci.*, 2001, vol. 9(4), 285-301.

[51] Reeve, H. M., Mescher, A. M., Effect of unsteady natural convection on the diameter of drawn polymer optical fiber, *Opt. Express*, 2003, vol. 11, 1770-1779.

[52] Reeve, H. M., Mescher, A. M., Emery, A. F., Investigation of steady-state drawing force and heat transfer in polymer optical fiber manufacturing, *J. Heat Tran.*, 2004, vol. 126, 236-243.

[53] Roy Choudhury, S., Thermal Transport in the Optical Fiber Drawing Process, Ph. D. dissertation, 1995, Rutgers University, New Brunswick, New Jersey.

[54] Roy Choudhury, S., Jaluria, Y., Lee, S. H. -K., Generation of neck-down profile for furnace drawing of optical fiber, *Proceedings of the 30th National Heat Transfer Conference*, 1995, Vol. 4, 23-32.

[55] Roy Choudhury, S. and Jaluria, Y., Thermal Transport due to Material and Gas Flow in a Furnace for Drawing an Optical Fiber, *J. Materials Research*, 1998, Vol. 13(2), 494-503.

[56] Roy Choudhury, S. and Jaluria, Y., Practical Aspects in the Drawing of an Optical Fiber, *J. Materials Research*, 1998, Vol. 13(2), 483-493.

[57] Roy Choudhury, S., Jaluria, Y. and Lee, S. H. -K., Generation of the Neck-down Profile for Furnace Drawing of optical fiber, *Numerical Heat Transfer*, 1999, Vol. 35, 1-24.

[58] Sa'ar, A., Moser, F., Akselrod, S., et al, Infrared optical properties of polycrystalline silver halide fibers, *Appl. Phys. Lett.*, 1986, vol. 49, 305-307.

[59] Sarboh, S. D., Milinkovic, S. A., Debeljkovic, D. L. J., Mathematical Model of the Glass Capillary Tube Drawing *Process, Glass Technol.*, 1998, Vol. 39(2), 53-67.

[60] Scholze, H., Glass, Nature, Structure, and Properties, translated by M.J. Lakin, 1990, Springer-Verlag, New York.

[61] Siegel, R. and Howell, J. R., Thermal Radiation Heat Transfer, 2001, Taylor and Francis, London.

[62] Siegel, R. and Spuckler, C. M., Effect of index of refraction on radiation characteristics in a heated absorbing, emitting and scattering layer, *J. of Heat Transfer*, 1992, Vol. 114, 781-784

[63] Wei, Z., Lee, K., Tchikanda, S. W., et al, Free surface flow in high speed fiber drawing with large-diameter glass preforms, *ASME J. Heat Transfer*, 2004, Vol. 26, 713-722.

[64] Wu, S., Surface and interfacial tensions of polymer melts. II. Poly(methyl methacrylate), poly(n-butyl methacrylate), and polystyrene, *J. Phys. Chem.*, 1970, Vol. 74(3, 5), 632-638.

[65] Xue, S. C., Tanner, R. I., Barton, G. W., et al, Fabrication of microstructured optical fibers- Part I: Problem formulation and numerical modeling of transient draw process, *J. Lightwave Tech.*, 2005, Vol. 23(7), 2245-2254.

[66] Xue, S. C., Tanner, R. I., Barton, G. W., et al, Fabrication of microstructured optical fibers- Part II: Numerical modeling of steady-state draw process, *J. Lightwave Tech.*, 2005, Vol. 23(7), 2255-2266.

[67] Yang, J. and Jaluria, Y., Numerical Modelling of Hollow Fiber Drawing, *Proc. 13th Int. Heat Transfer Conf.*, 2006, Sydney, Australia.

[68] Yin, Z. L., Numerical Investigation of Thermal Transport in Optical Fiber Drawing Processes, Ph. D. dissertation, 1997, Rutgers University, New Brunswick, New Jersey.

[69] Yin, Z. L. and Jaluria, Y., Zonal Method to Model Radiative Transport in an Optical Fiber Drawing Furnace, *ASME Journal of Heat Transfer*, 1997, Vol. 119(3), 597-603.

[70] Yin, Z. L. and Jaluria, Y., Thermal Transport and Flow in High-speed Optical Fiber Drawing, *J. Heat Transfer Trans. ASME*, 1998, Vol. 120, 916-930.

[71] Yin, Z. and Jaluria, Y., Neckdown and thermally induced defects in high speed optical fiber drawing, *ASME J. Heat Transfer*, 2000, Vol. 122, 351-362.

Vita

Jing Yang

2008 Ph.D. in Thermal Science, Department of Mechanical and Aerospace Engineering Rutgers, The State University of New Jersey, New Brunswick NJ

2003 M. S. in Fluid Mechanics, Department of Applied Mechanical Engineering Fudan University, Shang Hai, China

2000 B. S. in Applied Mechanics, Department of Applied Mechanical Engineering Fudan University, Shang Hai, China

2006-2007 Research Assistant, Department of Mechanical and Aerospace Engineering Rutgers, The State University of New Jersey, New Brunswick NJ

2005-2006 Teaching Assistant, Department of Mechanical and Aerospace Engineering Rutgers, The State University of New Jersey, New Brunswick NJ

2004-2005 Research Assistant, Department of Mechanical and Aerospace Engineering Rutgers, The State University of New Jersey, New Brunswick NJ

2003-2004 Rutgers Graduate Fellowship, Department of Mechanical and Aerospace Engineering Rutgers, The State University of New Jersey, New Brunswick NJ

2007 **Yang, J.** and Jaluria, Y., Hole collapse during the drawing process for a hollow optical fiber, , 2007, Present at American Physical Society Division of Fluid Dynamics 60th Annual Meeting, Salt Lake City, UT.

2006 **Yang, J.** and Jaluria, Y., Numerical Modelling of Hollow Fiber Drawing, 2006, Proc. 13th Int. Heat Transfer Conf., Sydney, Australia.

2001 Ding, G. H., **Yang, J.**, el al, Directional Flow of Interstitial Fluid In Human Body, 2001, Progress in Nature Science, 11(8): 811-818.